Kenate Nemera Nigussa

Density Functional Theory Investigations of Surface Structure and Reactivity

Thesis for the degree of Philosophiae Doctor

Trondheim, February 2011

Norwegian University of Science and Technology
Faculty of Natural Sciences and Technology
Department of Physics

NTNU – Trondheim
Norwegian University of
Science and Technology

NTNU
Norwegian University of Science and Technology

Thesis for the degree of Philosophiae Doctor

Faculty of Natural Sciences and Technology
Department of Physics

ISBN 978-82-471-2717-9 (printed ver.)
ISBN 978-82-471-2718-6 (electronic ver.)
ISSN 1503-8181

Doctoral theses at NTNU, 2011:93

Printed by NTNU-trykk

ABSTRACT

The $Cr_2O_3(0001)$ surface is assumed to terminate by chromium atoms, chromyl groups, and oxygen atoms. This essentially models the industrial surface when subjected to different oxygen chemical potentials. The issue of high temperature surface states is also of particular importance concerning various effects such as corrosion. The investigation of the interaction of selected atomic adsorbates, paper I, has not only been important from a fundamental physics point of view, but also offered useful insight on applied subjects such as corrosion.

Various diatomic molecules, paper II, are found to show different reactivities to the $Cr_2O_3(0001)$ surface. The different terminations provide insight on the reactivity of the surface to the molecules under varying oxygen chemical potential as background environment. Various chemical complexes have been investigated, each having applications in chemical catalysis, including the growth of an H_2O layer in a hexagonal 2D lattice and an array of Cl atoms in a honeycomb lattice.

Poisoning of materials by sulfuric acid is among the daily problems worldwide, with significant loss of resources. A mechanistic design on how to avert the problem is at the heart of scientific activities. This study, paper III, investigates the interaction of molecular, intermediately decomposed, and fully decomposed states of H_2S with the $Cr_2O_3(0001)$ surface, allowing for the possibility of a varying oxygen chemical potential as background environment. Based on the difference in reactivity of the adsorbate species with the differently terminated surfaces, we have suggested that a higher oxygen chemical potential as background environment has a potential to be unreactive to the adsorbate species or at least minimize the surface poisoning.

Titanium-nickelide is an important biomaterial with various applications in medical technology. However, it is still a matter of a continued research effort on how to establish the best biocompatible version of the material. Existence of nickel atoms at contact points of the biomaterial has been reported to hamper the quality of the biomaterial. As a consequence, several experimental activities have been carried out to remedy a surface treatment of the material, mostly by oxidation. This study, paper IV, characterizes the oxidation of various low indexes of the biomaterial surface. Based on this characterization, a conclusion is reached that doping the material with potassium atoms improves the performance quality of the biomaterial and a method of achieving the doping is suggested.

The use of two or more DFT packages, with different basis sets, may be motivated for consistency verification of results obtained so as to make quality conclusions, or to take advantage of a reduced computational time. In this report, paper V, we have shown that the Dacapo DFT package and the BAND DFT package with very different basis sets, i.e., plane waves and atomic orbitals, respectively, can be used together in a single study by satisfying the above motivation points. We have reported that the pseudopotentials (frozen

cores) used in the calculations play a crucial role for the outcome of calculations and computation time demand, and suggested a possible discrepancy in the magnitudes of energy differences.

The alloy between rare earths and novel transition metals Pt and Pd is of renewed research interest. This is in part motivated by the desire to tailor some of the properties of these widely applied transition metals or the rare earths. To be able to have control over the quantitative changes in the properties, a clear establishment of the alloy structures is crucial. There have been considerable experimental research efforts carried out reporting the investigated alloy structures. However, a consistent conclusion has not been obtained. This study, paper VI, is based on the various experimentally predicted structures and systematically suggests the most stable structure.

Preface

This thesis is submitted as a part of the requirements for the degree Philosophiae Doctor at the Norwegian University of Science and Technology (NTNU). The doctoral thesis is performed at the Department of Physics, NTNU, Trondheim. My supervisor has been Associate Professor Jon Andreas Støvneng and the research is financed by the Norwegian University of Science and Technology through the Department of Physics.

My contributions to the papers are as follows. I am the first author of all the papers. For papers I and II, calculations are done in collaboraton with K. L. Nielsen. For paper III, calculations are done by me. Papers I - III are written jointly with my supervisor and important feedback and assistance are obtained from the respective coauthors. For Papers IV, calculations are done by me and the reports are written jointly with my supervisor. For Papers V and VI, calculations are done by me and the reports are written by me.

Kenate Nemera Nigussa

Trondheim, February 2011

ACKNOWLEDGMENTS

I have to formally thank my supervisor Associate Professor Jon Andreas Støvneng whose support has been countless and gentle throughout this work. He did not doubt my suitability for the work, and has created good working conditions throughout. Thus, I would say that this thesis wouldn't have been possible if it were not due to his support and help. I am very grateful for the opportunity he has given me and have no words to express my deep respect but simply have to say Tusen Takk!.

Next, I would like to thank Dr. Ø. Borck for his mentorship (co-supervision) during the first two years. By the time I started the PhD work, he had just finished his own. I then had to start with software on which he had gained great expertise. So, he provided me the necessary orientations as a smooth kickstart. A number of other people deserve my thanks for being directly or indirectly helpful to the papers of this work. These include former M.Sc (now PhD) student Kjetil L. Nielsen, Professor Steinar Raaen, and Dr. Henrik Tollefsen.

Some of the papers in this thesis are initiated to simulate experimental work in S. Raaen's group in which notably the then PhD student H. Tollefen was the author of that experimental work. I appreciate the fruitful discussions we held with them immediately after Tollefsen's defence. Moreover, S. Raaen has always been available and welcoming further discussions for which he deserves my appreciation.

Special thanks to Norwegian High Performance Computing (NOTUR) for providing super computer facilities. The research has consumed about 10^6 CPU hours, which is certainly not affordable by any set of local PCs.

Finally, I would like to thank my siblings and in-laws for frequently interrupting me with electronic chats and calls. They have shown me their deep love and inspiration and are always interested in learning how things are progressing on my side.

Last but not least, I am thankful to my parents for their enduring and unconditional love. Thanks to **almighty God** for giving me life and keeping me healthy during the entire work.

Kenate Nemera Nigussa
Trondheim, February 2011

Dedicated to my parents and fiancée

LIST OF PUBLICATIONS

Paper I: K.N. Nigussa, K.L. Nielsen, Ø. Borck, and J.A. Støvneng.
Adsorption of hydrogen, chlorine, and sulfur atoms on α-Cr_2O_3(0001) surfaces: A Density Functional Theory investigation.
Submitted to Corrosion Science.

Paper II: K.N. Nigussa, Ø. Borck, J.A. Støvneng, and K.L. Nielsen.
Adsorption of H_2, Cl_2, and HCl molecules on α-Cr_2O_3(0001) surfaces: A Density Functional Theory investigation.
Submitted to Journal of Chemical Physics.

Paper III: K.N. Nigussa, Ø. Borck, and J.A. Støvneng.
Adsorption of H_2S on α-Cr_2O_3(0001) surfaces: A Density Functional Theory investigation.
Submitted to Surface Science.

Paper IV: K.N. Nigussa and J.A. Støvneng.
Oxidation of pure and potassium-doped NiTi shape memory surface: A density functional theory investigation.
Phys. Rev. B **82**, 245401 (2010).

Paper V: K.N. Nigussa and J.A. Støvneng.
Theoretical investigation of the interaction of oxygen with pure and K-doped NiTi shape memory surface alloys.
Computer Physics Communications (2010), doi:10.1016/j.cpc.2010.12.027.

Paper VI: K.N. Nigussa and J.A. Støvneng.
Alloy structure of rare earth Ce with Pt base metal, and the adsorption of CO.
Preprint.

Not included in the thesis

K.N. Nigussa and J.A. Støvneng.
Adsorption of C_2H_4 on Fe_2O_3(0001) surface.
In preparation.

K.N. Nigussa and J.A. Støvneng.
Adsorption of C_2H_4 on Pd, Rh, and Pt surfaces.
In preparation.

Contents

Chapter 1

Introduction

Solid state calculations are traditionally used to obtain total energies, as described in section 2, from which various interpretations are made [1]. As such, various energy values corresponding to cohesive energies and adsorption energies etc. can be calculated [2]. While the interest in bulk calculations is often associated with properties such as hardness [3],[4], surface calculations address various applied topics which include hardness [5], reactivities [6]-[13], etc.

Almost all chemical reactions proceed from a surface [14]. As such, the reactivities would address topics on applied subjects such as corrosion [6],[7], chemical evolutions [8],[9], catalysis [10],[11], and interfaces (thin films) [12],[13]. Studies of reactions at surfaces are modeled theoretically by adsorbing an adsorbate of interest on a surface of interest. Such an approach typically requires modeling the surfaces as slabs of four to five layers where often the bottom (or middle) two layers are constrained to the bulk geometry while the remaining layers are allowed to relax. The adsorbate species are optimized in a large unit cell, for example a cubic unit cell of 15 Å, before adsorption. As such, insight about the initial reactant states of the surfaces and adsorbates, including their total energies, are obtained. Insight on reaction properties, with applications to either of the applied subjects mentioned above, of the combined adsorbate-substrate state is obtained by putting the adsorbates of interest on reaction sites (adsorption sites) of the surfaces. See Fig. 1(A) for an example.

Based on the favored (occupied) adsorption sites, the structure of the adsorbate can be conveniently expressed in terms of the surface structure, see for example Fig. 1(B). Such adsorbate structure descriptions have, for example, been done in paper II where an H_2O layer (or complex) on the $Cr_2O_3(0001)$ surface resumed a hexagonal 2D lattice, while Cl atoms formed an array of honeycomb lattice. A structural description of alloy surfaces is also given weight, where one species of the alloy system occupies certain sites of the base elements, resuming a structure which is expressible in terms of the structure of the base element, see for example paper VI. A determination of the correct adsorption sites also plays a crucial role in the growth of a few layers (thin films) on a surface, see for example paper IV.

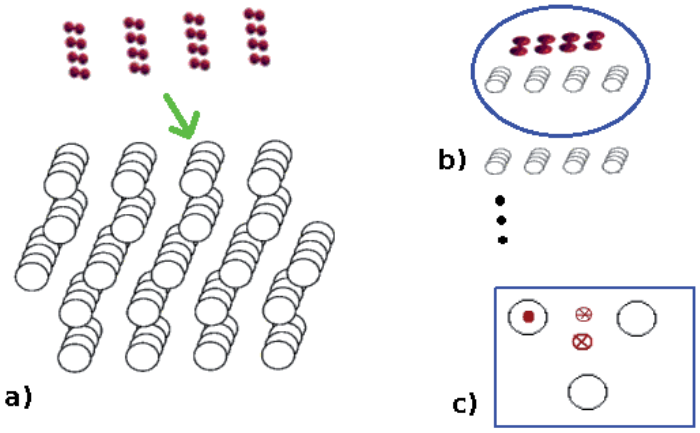

(A)

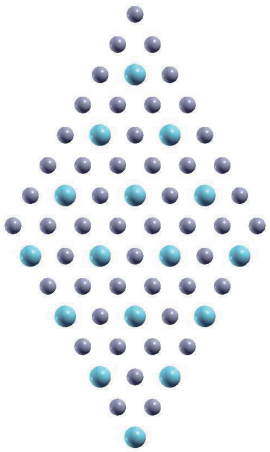

(B)

Figure 1.1: (A) (a) Surface model and adsorbate in the initial (reactant) state, (b) the adsorption process, and (c) the adsorption (reaction) sites. The dot, circled star, and circled cross show ontop, bridge, and hollow sites, respectively. (B) Typical alloy structure of a layer of $CePt_3$. Light green circles denote Ce atoms while dark circles denote Pt atoms. Different configurations of adsorption sites exist, resulting in different possible adsorbate structures.

In terms of the applied issues addressed, the studies in paper I may be categorized as corrosion, papers II and III are categorized as chemical physics, and papers IV, V, and VI are categorized as structures (growth and interfaces).

Chapter 2

Density Functional Theory

2.1 Introduction

The beginning of quantitative quantum mechanical calculations for many body systems can be seen as having its roots with the Hartree theory [15]. The theory assumes the wave function of the system to be symmetric and a product of the wave functions of individual electrons. The Coulomb interaction potential between an electron and the rest of the electrons is approximated by a mean field potential, V_H, [1§] written as

$$V_H(\mathbf{r}) = \int \frac{n(\mathbf{r'})}{\mid \mathbf{r} - \mathbf{r'} \mid} d^3r'. \tag{2.1}$$

The Hamiltonian operator corresponding to each electron is thus,

$$\hat{H} = \hat{T} + \hat{V} + \hat{V}_H \tag{2.2}$$

where $\hat{V}$ is the interaction term between an electron and the nuclei. However, the theory does not include further electron interaction terms and as a consequence failed to give good predictions of (binding) energies. The first major improvement is made following the work of Fock [16] who recognized that the wave function of an electron must be antisymmetric in space and/or spin coordinates, obeying the Pauli exclusion principle. The wave function of the system is thus written as a Slater determinant. [1‡] The incorporation of this wave function condition into the Hartree theory resulted in what is called the Hartree-Fock theory.

Applying the Hamiltonian operator in Eqn. (2.2) to the Hartree-Fock wave function of the system, we obtain the energy for the system to be

$$E_{HF} = E_{Hartree} - \sum_{i,j=1}^{N/2} \int\int \psi_i^*(\mathbf{r_1})\psi_j(\mathbf{r_1}) \frac{1}{\mid \mathbf{r_1} - \mathbf{r_2} \mid} \psi_i(\mathbf{r_2})\psi_j^*(\mathbf{r_2}) d\mathbf{r_1} d\mathbf{r_2}, \tag{2.3}$$

[1§] where

$$n(\mathbf{r'}) = \sum_{i=1}^{N} |\psi_i(\mathbf{r'})|^2.$$

[1‡] The concept of Slater determinant follows from a work by Slater (1929) [17].

where $E_{Hartree}$ is the total energy obtained by applying the Hartree wave function to the operator. The second term is the exchange integral and is a consequence of the form of the wave function. Clearly, the energy is better minimized for the electronic system with the Hartree-Fock theory than the Hartree theory. For easy practical implementation, it is interesting to further simplify and partition the exchange integral to one electron. Suppose $\psi_i^*(\mathbf{r_1})$ is a diagonalized function. Then, the Hamiltonian operator for one electron can be written as

$$\hat{H} = \hat{T} + \hat{V} + \hat{V}_H + \hat{V}_x, \tag{2.4}$$

where $\hat{V}_x$ is the operator corresponding to the exchange energy which can be given by

$$\hat{V}_x = -\sum_{j=1}^{N} \int d\mathbf{r_2} \psi_j^*(\mathbf{r_2}) \psi_i(\mathbf{r_2}) \frac{1}{\mid \mathbf{r_1} - \mathbf{r_2} \mid} \frac{\psi_j(\mathbf{r_1})}{\psi_i(\mathbf{r_1})}. \tag{2.5}$$

Each wave function $\psi_i(\mathbf{r})$ is further expressed as a sum over a set of functions $\{\phi_\mu(\mathbf{r})\}$, a basis set, by

$$\psi_i(\mathbf{r}) = \sum_{\mu=1}^{K} C_{i,\mu} \phi_\mu(\mathbf{r}). \tag{2.6}$$

The solution to the one electron wave function is thus obtained by first starting with a trial wave function as in Eqn. (2.6), then calculate the densities, then insert the densities and trial wave functions into Eqn. (2.4) thereby calculating energies. The process is repeated iteratively until the global total energy minimum is obtained. Another approach is to apply a variational principle to Eqn. (2.6). This transforms the Hartree-Fock equations into Roothaan equations [18] which are widely used in quantum chemistry.

The problem is that the computational time scales as N^4, see Fig. 2.1 (a), to calculate the full wave function in an $N \times N$ Slater determinant even with the Hartee-Fock approach where a correlation energy treatment is missing. The computational time becomes even worse, scaling as N^6, with post-Hartree-Fock methods such as configuration interaction singles (doubles) which include a contribution due to the electron correlation interactions. As a consequence, the feasible application of these wave function methods is restricted to small size systems rather than extended (large crystal) systems.
This has lead to the emergence of a comprehensive quantum many electron theory with the electron density $n(\mathbf{r})$ as the basic variable [19], which has become a starting base for the current practical implementations of density functional theory. Hohenberg and Kohn suggested the total energy of a system to be a functional of the density,

$$E[n(\mathbf{r})] = F_{HK}[n(\mathbf{r})] + \int V_{ext}(\mathbf{r}) n(\mathbf{r}) d\mathbf{r}. \tag{2.7}$$

[2‡] As such, there is a one to one correspondence between $n(\mathbf{r})$ and $V_{ext}(\mathbf{r})$, see Fig. 2.1 (b), and hence the obtained ground state density would lead to the

[2‡] where $F_{HK}[n(\mathbf{r})] = T[n(\mathbf{r})] + E_{XC}[n(\mathbf{r})] + \frac{1}{2}\int V_H[n(\mathbf{r})] n(\mathbf{r}) d\mathbf{r}$ and $V_{ext}(\mathbf{r})$ is the interaction potential between electrons and nuclei. Sometimes F_{HK} is called a universal functional in the sense that its value is independent of the external potential.

global energy minimum by Eqn. (2.7), see Theorem I and II of Ref. [19].

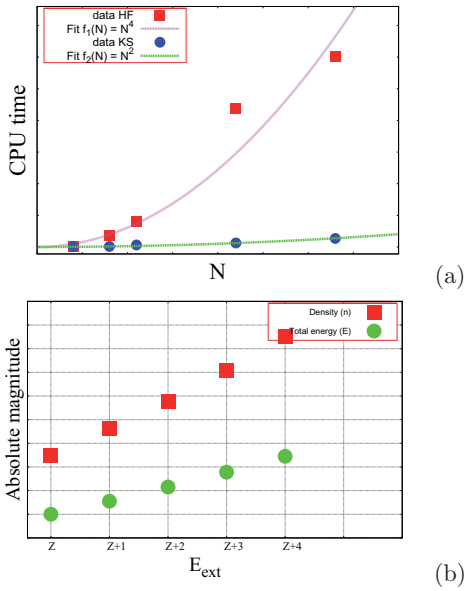

Figure 2.1: (a) Computational time vs the number of electrons N with DFT (blue circles) and Hartree-Fock theory (red squares), for selected small organic molecules. The green line is a quadratic fit to the DFT data. The pink line is an N^4 fit to the Hartree-Fock data. (b) Relation between external potential energy E_{ext} and the maximum value of the electron density n (red squares) and the total energy E (green circles). E_{ext} due to nuclei-electron interaction is in a one to one correspondence with electron density and total energy. The electron density and total energy are in turn in one to one correspondence. This illustrates the basic theorems of DFT.

The Thomas-Fermi theory, established from early works of Thomas [20] and Fermi [21], is credited for its initial ideals on expressing the total energy of a many electron system as a functional of the electron density. But their treatment of the Hamiltonian, in its original form, was on a (semi-) classical level, missing most of the quantum effects (exchange and correlation interactions) among the electrons. The theory was based on a uniform electron gas model for the kinetic energy and the Poisson equation for the potential V_H, leading to a nonlinear equation of the form,

$$\nabla^2 V_H(\mathbf{r}) = C[\mu - V_{ext}(\mathbf{r}) - V_H(\mathbf{r})]^{\frac{3}{2}}. \tag{2.8}$$

[2§] The Thomas-Fermi total energy, described for example in [22], is obtained by numerical integration using the values of V_H, V_{ext}, and $n(\mathbf{r})$ (equivalent to the right hand side of Eqn. (2.8)). The Thomas-Fermi model can thus be

[2§] Here C is some correctly chosen constant and μ is the chemical potential. See for example, Ref. (5) for details.

simply regarded as a special case of the more general (inclusive) theory, i.e., the Hohenberg-Kohn formulation.

Table 2.1: Total energies (a.u.) for He, Ne, and Ar using the Thomas-Fermi (TF), Hartree (H), Hartree-Fock (HF), and Kohn-Sham (KS) approaches. The trends are of importance when compared against each other. The Thomas-Fermi model grossly overestimates the energy values.

Atom	TF (2.8)	H (2.2)	HF (2.4)	KS (2.9)
He	−3.87	−1.84	−2.86	−2.90
Ne	−165.61	−116.61	−122.07	−128.90
Ar	−652.72	−496.88	−500.07	−527.49

Practical implementation of the Hohenberg-Kohn formulation is made possible following the ansatz by Kohn and Sham [23], where a non-interacting kinetic energy is assumed with an interacting electron density. The non-classical self-interactions of the electrons are included in and contributed by the exchange-correlation term. As such, a one electron Hamiltonian is given as

$$\hat{H} = \hat{T}_{KS} + \hat{V} + \hat{V}_H + \hat{V}_{xc}. \tag{2.9}$$

The methodology progress is shown in Table 2.1. The exact values of the kinetic and exchange-correlation energies are explicit functionals of density, $T_{KS}[n]$ and $E_{XC}[n]$, according to Hohenberg and Kohn [19] and are unknown. The Kohn-Sham kinetic energy, $T_{KS} = \langle \psi \mid \hat{T}_{KS} \mid \psi \rangle$, is only an implicit functional of the density and the residual energy (the difference between exact and Kohn-Sham kinetic energies) could be offset by choosing an appropriate form of the exchange-correlation energy. The original idea of the Kohn-Sham approach assumes a non-relativistic treatment,

$$T_{KS} = \langle \psi \mid -\frac{1}{2}\nabla^2 \mid \psi \rangle. \tag{2.10}$$

Since then, some refinements, which include a relativistic treatment, mostly to the kinetic energy, have been assumed and implemented in some software packages [24]. As such, the matrix elements of the kinetic energy with a scalar relativistic treatment are

$$T_{KS} = \langle \nabla\psi \mid -\frac{c^2}{2c^2 - U} \mid \nabla\psi \rangle, \tag{2.11}$$

where c is the speed of light and U is the total potential energy. This is to be compared with the matrix elements of Eqn. (2.10), $T_{KS} = \langle \nabla\psi \mid -\frac{1}{2} \mid \nabla\psi \rangle$. This treatment is found to yield better minimum energies in some modestly heavy elements as shown in Fig. 2.2. For very heavy elements (such as Pb, not presented here), a vectorial relativistic treatment to first order, formulated as

$$T_{KS} = \langle \mathbf{M} \mid -\mathbf{m}\frac{c^2}{2c^2 - U} \mid \mathbf{M} \rangle, \tag{2.12}$$

is expected to be necessary. Here **M** and **m** are matrices given by

$$\mathbf{M} = \vec{\sigma} \cdot \begin{pmatrix} \tilde{\nabla}\phi_1 \\ \tilde{\nabla}\phi_2 \end{pmatrix}$$

and

$$\mathbf{m} = \mathbf{1} - \frac{\vec{\sigma} \cdot \vec{p}c^2 \vec{\sigma} \cdot \vec{p}}{(2c^2 - U)^2}.$$

Here, $\vec{\sigma}$ is a 2×2 Pauli matrix and ϕ_1 and ϕ_2 are spinor components. The improved kinetic energy in turn leads to an improvement of total energies and potentials, albeit to a lesser extent, as shown in Fig. (2.2). The figure shows that the relativistic treatment is increasingly important as the nuclei become heavier and the difference between Scalar Relativistic (ZORA, Eqn. (2.11)) and Spin Orbit Relativistic (FORA, Eqn. (2.12)) energies is negligible for the considered nuclei, but quite different in computational time demand. A more detailed explanation of the formulation of the relativistic effects can be found in the relevant literature [25]. The effect of this treatment on adsorption energies is shown and summarized in a paper by Philipsen et al. [26]. They have shown that energetic improvements due to the relativistic treatment play a key role for the judgement of energetically favored adsorption sites.

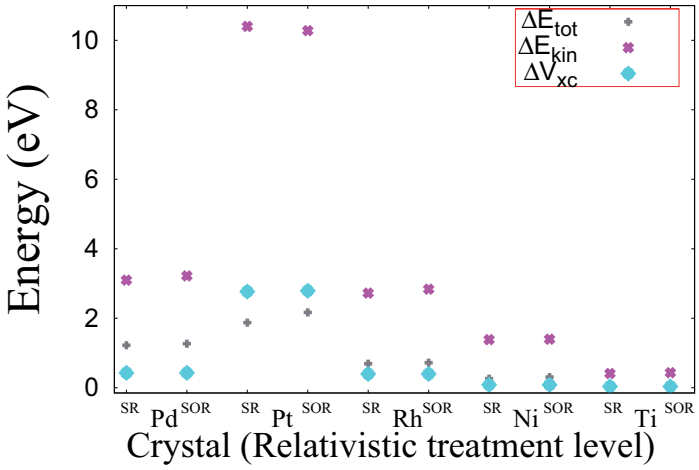

Figure 2.2: Relativistic effects are most pronounced for heavy elements such as Pt. The effects are less pronounced for lighter elements such as Ti. Here, zero energy denotes the nonrelativistic treatment.

2.2 The functionals

The exchange-correlation energy E_{xc}[n] is unknown. As a consequence, approximations have to be made and hence there are different exchange-correlation

functionals widely in use today, being implemented on the basis of different approximations [28]−[33]. The exact value of the exchange energy can be calculated from Eqn. (2.5), by applying Fock's antisymmetry principle [16] to the Kohn-Sham wave functions, and can be expressed as

$$E_x[n] = \frac{1}{2}\int d\mathbf{r} n(\mathbf{r}) \int d\mathbf{r}' \frac{n_x(\mathbf{r}, \mathbf{r}')}{\mid \mathbf{r} - \mathbf{r}' \mid}, \tag{2.13}$$

where $n_x(\mathbf{r}, \mathbf{r}')$ is the exchange hole density.[§ 3] However, this can produce results in a feasible computational time only for few-electron systems. For extended (solid) systems, approximations have to be made. The simplest approximation is the assumption of a uniform electron gas [34] where the exchange energy in the local density approximation can be expressed as,

$$E_x^{LDA}[n] = C\int n^{4/3} d\mathbf{r} \equiv \int n(\mathbf{r}) \epsilon_x^{hom}(n) d\mathbf{r}. \tag{2.14}$$

Eqn. (2.14) can be extended to spin polarized systems, which then reads

$$E_x^{LSD}[n_\uparrow, n_\downarrow] = \int n(\mathbf{r})(\epsilon_x(2n_\uparrow) + \epsilon_x(2n_\downarrow)) d\mathbf{r}. \tag{2.15}$$

This approach, exact in principle for homogeneous systems, has severe shortcomings when applied to real systems (with inhomogeneous densities) [28]. Based on the concept of the gradient expansion approximation [35], a correction is added to Eqn. (2.14) and takes the form

$$E_x^{GEA}[n] = \int n(\mathbf{r}) \epsilon_x^{hom}(n) d\mathbf{r} + \beta_x \int d\mathbf{r} \frac{(\nabla n)^2}{n^{4/3}}. \tag{2.16}$$

Similarly, the correction in the case of a spin polarized system takes the form

$$E_x^{GEA}[n_\uparrow, n_\downarrow] = E_x^{LSD}[n_\uparrow, n_\downarrow] + \int \sum\nolimits_{\alpha,\beta} \frac{C_{\alpha\beta}(n_\uparrow, n_\downarrow)}{(n_\alpha n_\beta)^{2/3}} \nabla n_\alpha \nabla n_\beta d\mathbf{r}. \tag{2.17}$$

Here, α and β each runs over spins up and down. However, this approach fails to satisfy some of the physical conditions of an exchange hole described elsewhere [27]. As a consequence, a class of generalized gradient approximations (GGAs) [28], [31]−[33] have emerged with analytic form

$$E_x^{GGA}[n] = \int d\mathbf{r} f(n, \nabla n) \tag{2.18}$$

and

$$E_x^{GGA}[n_\uparrow, n_\downarrow] = \int d\mathbf{r} f(n_\uparrow, n_\downarrow, \nabla n_\uparrow, \nabla n_\downarrow) \tag{2.19}$$

in spin unpolarized and spin polarized systems, respectively. Corrections to the gradient expansion approximation [35] are made by assuming a summation of an infinite series of powers of ∇n until all the physical conditions of the exchange hole are fairly met. The difference between the functionals is on the

[3§] The exchange hole density has negative values, and integrates to -1 [27].

details of parametrizations used in the perspective of fulfilling those conditions. The analytic form of the correlation energy is complicated and does not have a simple form of inverse proportionality with $\mathbf{r}$ [29],[30]. On the other hand, the simple inverse relation of the exchange energy to $\mathbf{r}$, for example Eqn. (2.13), was the reason for the emergence of GGA based and practically implementable approximations to the exchange energy [28].

The Kohn-Sham ansatz was first implemented with the uniform gas model for the exchange-correlation energy, where both the exchange and correlation energies are approximated in the same way [23], given as

$$E_{xc}^{LDA}[n] = \int n(\mathbf{r})\epsilon_{xc}^{hom}(n) \tag{2.20}$$

and

$$E_{xc}^{LSD}[n_\uparrow, n_\downarrow] = \int d\mathbf{r} n(\mathbf{r})(\epsilon_{xc}(2n_\uparrow) + \epsilon_{xc}(2n_\downarrow)) \tag{2.21}$$

in spin unpolarized and spin polarized systems, respectively. This model is widely used today with a revised version by Vosko et al. [36] and provides exact values in homogeneous systems, and fairly accurate values in inhomogeneous systems. The surprise success of the model has since lead to a theory of exchange and correlation together in the same way, and an analytic description of the form

$$E_{xc}[n] = \frac{1}{2}\int d\mathbf{r} n(\mathbf{r}) \int d\mathbf{r}' \frac{n_{xc}(\mathbf{r}, \mathbf{r}')}{\mid \mathbf{r} - \mathbf{r}' \mid}, \tag{2.22}$$

was suggested [37]. The gradient expansion approximation [35] version of Eqns. (2.18 and 2.19) take the form

$$E_{xc}^{GEA}[n] = \int n(\mathbf{r})\epsilon_{xc}^{hom}(n)d\mathbf{r} + \beta_{xc}\int d\mathbf{r}\frac{(\nabla n)^2}{n^{4/3}} \tag{2.23}$$

and

$$E_{xc}^{GEA}[n_\uparrow, n_\downarrow] = E_{xc}^{LSD}[n_\uparrow, n_\downarrow] + \int \sum\nolimits_{\alpha,\beta} \frac{C_{\alpha\beta}(n_\uparrow, n_\downarrow)}{(n_\alpha n_\beta)^{2/3}} \nabla n_\alpha \nabla n_\beta d\mathbf{r}. \tag{2.24}$$

However, although it is an improvement over LDA (LSD), it has shortcomings of not fulfilling physical conditions of exchange-correlation holes, as also discussed above with Eqns. (2.16 and 2.17). This continued with the replacement with a class of GGAs [31]−[33] with functional expressions

$$E_{xc}^{GGA}[n] = \int d\mathbf{r} f(n, \nabla n) \tag{2.25}$$

for spin unpolarized systems, and

$$E_{xc}^{GGA}[n_\uparrow, n_\downarrow] = \int d\mathbf{r} f(n_\uparrow, n_\downarrow, \nabla n_\uparrow, \nabla n_\downarrow) \tag{2.26}$$

for spin polarized systems. From Eqn. (2.22), the exchange-correlation energy can be seen to vary as the inverse of $\mathbf{r}$. From Eqn. (2.13), the exchange energy

can be seen to vary as the inverse of $\mathbf{r}$. However, the form of the exchange energy, as discussed above, does not show a simple variation as $\mathbf{r}^{-1}$. This indicates that the exchange energy is dominating over the correlation energy, which is some secondary correction, but significant enough to make differences in measured properties of materials [31]−[33]. This could be a reason for the better efficiency and feasibility of GGA approximations by applying the necessary enhancement factors on the exchange energy (Eqns. (2.27) and (2.28)) rather than applying gradient expansions of the combined exchange-correlation, Eqns. (2.23) and (2.24). The relative differences between the efficiencies of the GGAs [31]−[33] are due to the differences in the parametrizations adopted by each of them. For example, with the parametrization by Perdew et al. [31],

$$E_{xc}^{GGA}[n] = \int d\mathbf{r} n(\mathbf{r}) \epsilon_x(r_s) F_{xc}(r_s, s) \tag{2.27}$$

for spin unpolarized systems and

$$E_{xc}^{GGA}[n_\uparrow, n_\downarrow] = \int d\mathbf{r} n(\mathbf{r}) \epsilon_x(r_s) F_{xc}(r_s, \zeta, s) \tag{2.28}$$

for spin polarized systems. For details, see Ref. [31].

2.3 k - points

§[5] In Eqn. (2.9), we can assume a Hamiltonian periodic in the unit cell. As such, the form of the electron wave function would be of plane wave type (Bloch wave function). For energy band i and wave vector $\mathbf{k}$, we have

$$\psi_{i,k}(\mathbf{r}) = C_{i,k}(\mathbf{r}) e^{i\mathbf{k}\cdot\mathbf{r}}, \tag{2.29}$$

and

$$n_{\mathbf{k}''}(\mathbf{r}) = \sum\nolimits_{i=1}^{N} C^*_{i,\mathbf{k}'}(\mathbf{r}) C_{i,\mathbf{k}}(\mathbf{r}) e^{i\mathbf{k}''\cdot\mathbf{r}}. \tag{2.30}$$

Here $\mathbf{k}'' = \mathbf{k}$ - $\mathbf{k}'$ is also a wave vector, spanning twice the range of $\mathbf{k}$. The electron density $n(\mathbf{r})$ is a sum of densities per wave vector $\mathbf{k}$. In the limit of a large number of bands N, it takes the form

$$n(\mathbf{r}) = \frac{1}{N} \frac{V_{cell}}{8\pi^3} \int_{BZ} n_k(\mathbf{r}) d^3k, \tag{2.31}$$

or

$$n(\mathbf{r}) = \frac{V_{cell}}{8\pi^3} \int_{BZ} n(\mathbf{k}) e^{i\mathbf{k}\cdot\mathbf{r}} d^3k. \tag{2.32}$$

The wave function in Eqn. (2.29) is not periodic in real space but periodic in reciprocal space [38]. The density is periodic in real space, and can be expressed as

$$n(\mathbf{r}) = \sum\nolimits_{\mathbf{G}}^{\mathbf{K_{max}}} n_{\mathbf{G}} e^{i\mathbf{G}\cdot\mathbf{r}}, \tag{2.33}$$

[5§] One obvious advantage with plane wave methods is the use of FFT, enabling efficient transformations back and forth between real and reciprocal space as necessary.

where $\mathbf{K_{max}}$ is an appropriately chosen cutoff wave vector, often simply called a density cutoff.

Next, simplifications of the computational demand to evaluate Eqns. (2.31) or (2.32) in a feasible time, while at the same time being able to study large systems, are desirable. This has been achieved by generating a finite number of special k points which can fairly sample the original k points in the BZ. At present, a k point sampling based on the Monkhorst-Pack scheme [39] is widely used in plane wave based programs. The set of $\mathbf{k}$ values generated as such are $\mathbf{k} = u_1\mathbf{b_1} + u_2\mathbf{b_2} + u_3\mathbf{b_3}$, and $\mathbf{k} = u_1\{\mathbf{b_1} + u_2\mathbf{b_2} + 1 \cdot \mathbf{b_3}$, respectively, for bulk and surface calculations. Here, $\{\mathbf{b_1}, \mathbf{b_2}, \mathbf{b_3}\}$ denote the primitive vectors in reciprocal space, and $\{u_1, u_2, u_3\}$ are the special points generated as

$$u_j = (2m - M - 1)/2M, (m = 1, 2, ..., M) \quad ; \quad (j = 1, 2, 3). \tag{2.34}$$

For example, for a k point mesh of $M\times M\times M$ ($M\times M\times 1$), the number of sample k points generated are M^3 (M^2). As a rule of thumb, M should be even, and experience shows that a value of M = 4 - 6, generally fares well in various systems. Further simplifications follow from the symmetry properties of the crystal. Time reversal and inversion symmetries automatically reduce the computational time by a factor of two. Space group symmetries which include point groups R ($\{R\mathbf{r} = \mathbf{r}\}$), and translation group $\mathbf{T}$ ($\{\mathbf{r} + \mathbf{T} = \mathbf{r}\}$) reduce the computational time further. The set of distinct symmetry groups could constitute an irreducible Brillouin zone (IBZ) with finite group elements. As such, the integrals in Eqns. (2.31) or (2.32) would reduce to summations over finite grids as

$$n(\mathbf{r}) = \frac{1}{2N_{group}} \sum\nolimits_{\mathbf{k}}^{IBZ} w_k n_{\mathbf{k}}(R\mathbf{r} + \mathbf{T}), \tag{2.35}$$

and

$$n(\mathbf{r}) = \frac{1}{2N_{group}} \sum\nolimits_{\mathbf{k}}^{IBZ} w_k n(\mathbf{k}) e^{i\mathbf{k}\cdot(R\mathbf{r}+\mathbf{T})}, \tag{2.36}$$

respectively, where w_k is the appropriate weight factor.

2.4 Cutoff energy

Practical implementations require a complete specification of the single particle Bloch states, whose periodic part $C_{i,k}(\mathbf{r})$ can be expressed as

$$C_{i,k}(\mathbf{r}) = \frac{1}{\sqrt{V_{cell}}} \sum_{\mathbf{G}} C_{i,\mathbf{k}+\mathbf{G}}\, e^{i\mathbf{G}\cdot\mathbf{r}}, \tag{2.37}$$

where

$$\sum\nolimits_{\mathbf{G}} |C_{i,\mathbf{k}+\mathbf{G}}|^2 = 1, \tag{2.38}$$

and $\mathbf{G}$ are reciprocal lattice vectors. Evaluating the kinetic energy part of the eigenstate $(i, \mathbf{k})$ gives

$$T = \sum\nolimits_{\mathbf{G}} |C_{i,\mathbf{k}+\mathbf{G}}|^2 \frac{\hbar^2}{2m} (\mathbf{k} + \mathbf{G})^2. \tag{2.39}$$

Now, with the possibility of an infinite number of $\mathbf{G}$ vectors, such calculations for all eigenstates $(i, \mathbf{k})$ are not feasible. A common practice is thus to truncate the $\mathbf{G}$ value to some $\mathbf{G_{max}} < \mathbf{G_{cut}} - \mathbf{k}$. As such, Eqns. (2.37) and (2.39) take the form

$$C_{i,k}(\mathbf{r}) = \frac{1}{\sqrt{V_{cell}}} \sum_{\mathbf{G}}^{\mathbf{G_{max}}} C_{i,\mathbf{k}+\mathbf{G}}\, e^{i\mathbf{G}\cdot\mathbf{r}} \tag{2.40}$$

and

$$T = \sum_{\mathbf{G}}^{\mathbf{G_{max}}} |C_{i,\mathbf{k}+\mathbf{G}}|^2 \frac{\hbar^2}{2m}(\mathbf{k}+\mathbf{G})^2, \tag{2.41}$$

respectively. From (2.41), it can be seen that the kinetic energy T is less than what is called the cutoff energy E_{cut}, which is given as $E_{cut} = \frac{\hbar^2}{2m} G_{cut}^2$. To obtain reliable results, the cutoff energy values should be selected carefully, and experience shows that values of 350−450 eV are often satisfactory for most systems. In Fig. 2.3, for example, we demonstrate the selection of E_{cut} values from a total energy point of view.

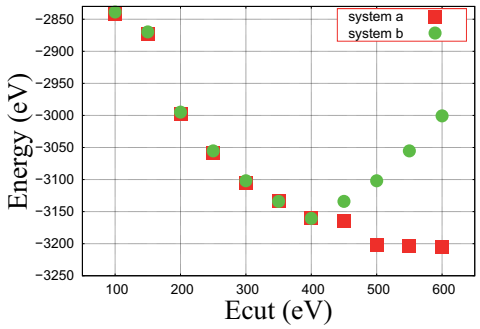

Figure 2.3: Depending on the system, the energetics continues to improve with increasing cutoff energy (system a) or attains a minimum with a cutoff energy of 400 eV (system b). However, in a system such as (a), the improvement in energetics is not rapid after a cutoff energy of 400 eV. Hence, a reasonable guess is to set up calculations with a cutoff energy of 400 eV.

2.5 Pseudopotentials

A further reduction of the basis set size in Eqn. (2.41) is essential. The motivation for this is also in part fueled by a concern over the rapidly oscillating nature of the wave functions, shown in Fig. (2.4), and the divergent nature (cusps) of the nuclei-electron interaction potential, in the vicinity of the nuclei. The remedy which has emerged has been to replace the real interaction potential within a region of some chosen cutoff radius r_c with a pseudopotential. As such, the rapid oscillations of the wave functions near the nuclei (i.e., requiring a large basis set) is replaced with a pseudo wave function, which is smooth and hence

requires a smaller basis set.

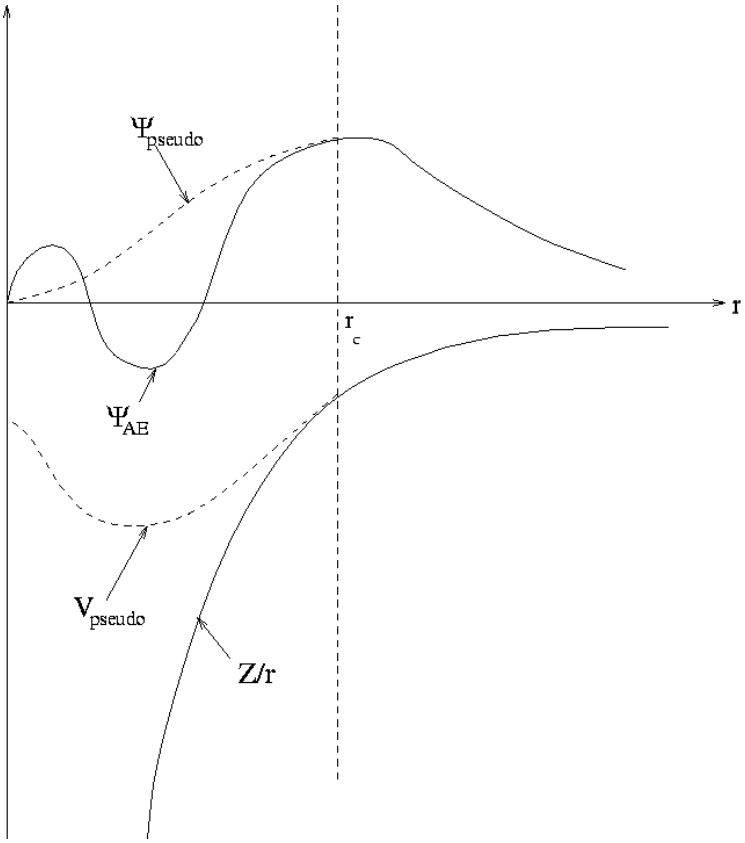

Figure 2.4: Smoothening of the wave function and potentials within a cutoff radius $\mathbf{r}_c$.

Moreover, the core electrons could be required to be frozen and/or possess wave functions orthogonal to the wave functions of the valence electrons. The development of pseudopotentials is of historical nature. Over the time, there are various pseudopotentials generated based on different assumptions. These include: hard core pseudopotentials [40], norm conserving ab-initio pseudopotentials [41], and other modified norm conserving pseudopotentials [42],[43], which include what is widely used and called ultra soft pseudopotentials [43].

While the ultra soft pseudopotentials provide smoother potentials and wave functions compared to the hard core pseudopotentials [40], they deviate more from the strict conservation of charge within r_c, as well as the energy eigenvalues [41]. The norm conservations are strictly met only outside r_c. However, the fact that ultra soft pseudopotentials are characterized by a relatively large r_c,

makes it very smooth (soft) and hence requires a smaller basis set for describing the wave functions. This makes it a frequent choice in the studies of large (extended) systems. Note, however, that the pseudo parameters must be carefully chosen so that the pseudo charges inside r_c and the pseudo eigenvalues do not deviate too much from the all electron charges, and all electron eigenvalues, respectively.
The above statements can alternatively be expressed as follows. Eqn. (2.9) can be written as

$$\hat{H} = \hat{T} + \hat{V}_{KS}, \tag{2.42}$$

where $\hat{V}_{KS}$ is the Kohn-Sham effective potential, which for convenience is denoted as $\hat{V}_{KS}^{pp}$ ($\hat{V}_{KS}^{ae}$) in the case of treatments with (without) pseudopotentials, respectively. The eigenvalue of state i is obtained as

$$(T + \hat{V}_{KS}^{ae})|\psi^{ae}\rangle = \varepsilon_i|\psi^{ae}\rangle, \tag{2.43}$$

and

$$(T + \hat{V}_{KS}^{pp})|\psi^{pp}\rangle = \varepsilon_i{}'|\psi^{pp}\rangle, \tag{2.44}$$

respectively, where ψ^{pp} (ψ^{ae}) are the corresponding wave functions with (without) the pseudopotential treatment. Conservation of charge and eigenvalues (norm conservation) means $\langle\psi^{ae}|\psi^{ae}\rangle = \langle\psi^{pp}|\psi^{pp}\rangle$, within and/or outside r_c, and $\varepsilon_i = \varepsilon_i{}'$. The idea behind the ultra soft pseudopotential is that the charges and eigenvalues do not have to be conserved within r_c, but they should be outside r_c.
One of the assumptions behind these pseudopotentials [42],[43] is to write $\hat{V}_{KS}^{pp}$ in separable form, as local (purely radial) and non-local components (which include an angular part and possibly some radial functions). I.e., $\hat{V}_{KS}^{pp} = \hat{V}_L + \hat{V}_{NL}$. Inserting this into Eqn. (2.44) gives

$$(\varepsilon_i{}' - T - \hat{V}_L)|\psi^{pp}\rangle = \hat{V}_{NL}|\psi^{pp}\rangle \equiv|\chi\rangle, \tag{2.45}$$

where

$$\hat{V}_{NL} = \frac{|\chi\rangle\langle\chi|}{\langle\chi|\psi^{pp}\rangle}. \tag{2.46}$$

As can be seen from the above equation, the form of $\hat{V}_{NL}$ depends on the eigenvalues assumed, and the different pseudopotentials that exist today differ on whether they strictly obey the norm conservation (i.e., $\varepsilon_i = \varepsilon_i{}'$ and/or $\langle\psi^{ae}|\psi^{ae}\rangle = \langle\psi^{pp}|\psi^{pp}\rangle$ within r_c) or not (i.e., $\varepsilon_i = M\varepsilon_i{}'$ and $\langle\psi^{ae}|\psi^{ae}\rangle = \langle\psi^{pp}|M|\psi^{pp}\rangle$ within r_c). In the latter case, some additional parameters must be provided to minimize the deviations. For a further discussion of this topic, see our paper [44].

2.6 Numerical and Slater type orbitals

Another frequently used class of basis set for the expansion of the electron wave function is atomic (-like) orbitals, be it numerical or analytic. As such, the

wave function of the electron is expressed as a linear combination of the basis functions (LCAO),

$$\psi_i(\mathbf{r}) = \sum_{\nu=1}^{M} c_{i,\nu}\eta_\nu(\mathbf{r}). \tag{2.47}$$

A complete basis set would require $M = \infty$. However, in practice, M is finite and it is crucial to choose appropriate (set of) functions $\eta_\nu(\mathbf{r})$ such that the linear combination (Eqn. (2.47)) provides an accurate approximation of the exact Kohn-Sham wave function. In some more complicated cases, each function $\eta_\nu(\mathbf{r})$ is in turn given as a linear combination of a second type of basis functions, say $\eta_a(\mathbf{r})$. As such, the wave function takes the form,

$$\psi_i(\mathbf{r}) = \sum_{\nu}^{M} c_{i,\nu} \sum_{a}^{A} c'_{i,a}\eta_a(\mathbf{r}). \tag{2.48}$$

However, this latter case is more than just a simple linear combination of basis functions with a single variable, as it involves an effective matrix (two variables) rather than just a simple coefficient vector. The computation time is proportional to some power of $M \times A$ compared to some power of M in the former case. The electron density may now be expressed as

$$n(\mathbf{r}) = \sum_{i}^{N} |\psi_i(\mathbf{r})|^2. \tag{2.49}$$

After certain manipulations, one could see that the application of the Kohn-Sham Hamiltonian (Eqn. (2.9)) to these wave functions could lead to a Roothaan type matrix formalism of the eigenvalue problem,

$$\mathbf{H}^{KS}\mathbf{C} = \mathbf{S}\mathbf{C}\varepsilon, \tag{2.50}$$

as described elsewhere at length [45]. This is acknowledged to be more easily coded into efficient computer programs. The form of the wave functions described above (Eqns. (2.47) and (2.48)) assumes the basis functions to be centered arbitrarily. A more common approach requires the basis functions to be centered on the atoms. As such, Eqns. (2.47) and (2.48) take the form,

$$\psi_i(\mathbf{r}) = \sum_{\nu}^{M} c_{i,\nu}\eta_\nu(\mathbf{r} - \mathbf{R}_I), \tag{2.51}$$

and,

$$\psi_i(\mathbf{r}) = \sum_{\nu}^{M} c_{i,\nu} \sum_{a}^{A} c'_{i,a}\eta_a(\mathbf{r} - \mathbf{R}_I), \tag{2.52}$$

respectively. The electron density corresponding to Eqn. (2.51) is then

$$n(\mathbf{r}) = \sum_{i}^{N} \sum_{\nu,\mu,I,I'} c_{i,\nu}c_{i,\mu}\eta_\nu(\mathbf{r} - \mathbf{R}_I)\eta_\mu(\mathbf{r} - \mathbf{R}_{I'}), \tag{2.53}$$

where I and I' describe the atoms, say in a unit cell. Eqn. (2.53) reveals the possibility of a contribution of the basis function centered on atom I' to the density on atom I. Such overlap contributions could also hold to the eigenenergies, as described elsewhere [46]. An alternative approach is to adapt the Bloch theorem to the basis functions of, say, Eqn. (2.51). In this regard, one can assume

$$\eta_\nu(\mathbf{r} - \mathbf{R}_I) = \sum_{\mathbf{T}} a_{\nu,k} e^{i\mathbf{k}\cdot\mathbf{T}} \eta_\nu(\mathbf{r} - \mathbf{R}_I - \mathbf{T}). \tag{2.54}$$

Substituting Eqn. (2.54) into Eqn. (2.51), the **k**-adapted eigenfunctions take the form

$$\psi_{i\mathbf{k}}(\mathbf{r}) = \sum\nolimits_{\mathbf{T}} e^{i\mathbf{k}\cdot\mathbf{T}} \left\{ \sum\nolimits_{\nu=1}^{M} C_{i,\nu\mathbf{k}} \eta_\nu(\mathbf{r} - \mathbf{R}_I - \mathbf{T}) \right\} \equiv \sum\nolimits_{\mathbf{T}} e^{i\mathbf{k}\cdot\mathbf{T}} \eta(\mathbf{r} - \mathbf{R}_I - \mathbf{T}). \tag{2.55}$$

Such an approach is the basis of some currently used program packages [47]. However, although this approach (Eqn. (2.55)) is interesting for solid state calculations, it is accompanied by a higher computer time demand compared to say, Eqn. (2.51). For example, if the number of **T** values is set to L, then the computation time demand can be seen to be proportional to some power of ($L\times M$) or ($L\times M\times A$) with Eqn. (2.55) compared to some power of M or $M\times A$ with Eqns. (2.54) and (2.52), respectively. The **k**-resolved eigenenergies and density can be given by

$$\hat{H}\psi_{i\mathbf{k}}(\mathbf{r}) = \varepsilon_{i\mathbf{k}}\psi_{i\mathbf{k}}(\mathbf{r}), \tag{2.56}$$

and

$$n_{i\mathbf{k}}(\mathbf{r}) = |\psi_{i\mathbf{k}}(\mathbf{r})|^2, \tag{2.57}$$

respectively. The effective eigenvalues and electron density can be given as a weighted sum of the forms in Eqns. (2.56) and (2.57) over the available **k** points, by

$$\varepsilon_i = \frac{1}{K} \sum\nolimits_{\mathbf{k}=1}^{K} w_{\mathbf{k}} \varepsilon_{i\mathbf{k}}, \tag{2.58}$$

and

$$n(\mathbf{r}) = \frac{1}{K} \sum\nolimits_{i}^{N} \sum\nolimits_{\mathbf{k}}^{K} w_{\mathbf{k}} n_{i\mathbf{k}}(\mathbf{r}), \tag{2.59}$$

respectively. At the heart of such an approach is the choice of appropriate basis functions, as mentioned already. Among the commonly used functions are Numerical Atomic Orbitals (η_ν^{NAO}), Slater Type Orbitals (η_ν^{STO}), and Gaussian Type Orbitals (η_ν^{GTO}). The Gaussian type orbitals ($\eta_\nu^{GTO} = Cr^\beta \mathrm{e}^{-\alpha r^2}$) ease the computational demand because they can be easily implemented in analytic form. As a consequence, they are the favorite choice in all electron calculations, where the use of pseudopotentials or freezing of some core electrons is not required. However, the downside of these basis functions is that they are far from exactly mimicing the hydrogen atom like orbitals, which are of exponential (slater type) nature. Due to this, they are often used in the forms described in Eqns. (2.48) or (2.52), where some desired number of η_a^{GTO} are linearly combined so as to give a single η_ν, if high accuracy is desired.

The Slater type orbitals ($\eta_\nu^{STO} = C' r^\beta \mathrm{e}^{-\alpha r} Y_{lm}(\theta,\phi)$), have an exponential nature and, as a consequence, are regarded as a natural choice of basis functions which can mimic the exact eigenfunctions well. However, the fact that η_ν^{STO} exhibits the correct cusp behavior at $r\rightarrow 0$ with a discontinuous derivative, unlike for example η_ν^{GTO}, makes it more difficult in practical calculations. Due to this, in practice, η_ν^{NAO} are used for some selected core electrons, where the $r\rightarrow 0$ effect is more pronounced, and a combination of η_ν^{NAO} and η_ν^{STO} is used for valence

electrons. There are various schemes of generating η_ν^{NAO}, ranging from some kind of spherically symmetric atom type approximation [48] to multiplication of the atomic orbital by an appropriate factor [49].
As described in Eqn. (2.48), the use of multiple η_ν^{STO} (in what is sometimes called a split valence basis) would increase the accuracy compared to single functions. This is shown in Fig. 2.5 (left), where the energetics is improved in going from single η_ν^{STO} (SZ) to double η_ν^{STO} (DZ) to triple η_ν^{STO} (TZ). Augmenting the basis sets with polarization functions (i.e., functions of higher

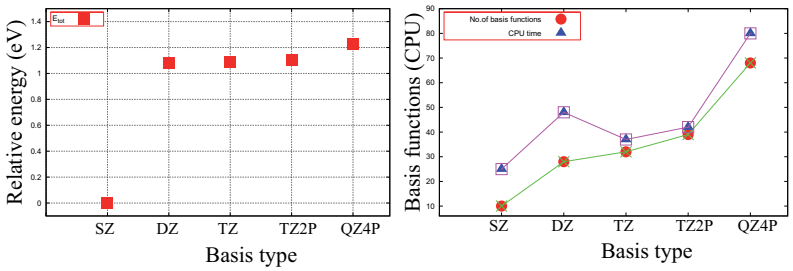

Figure 2.5: Improvement of the energetics with basis type from SZ to QZ4P (left). (Absolute values of the energy with respect to the SZ case. Hence, a higher relative energy amounts to an improvement.) However, an improved energetics is achieved at a requirement of significant computation time (right). Moreover, a comparison of the energetics with TZP and QZ4P (left) shows about the same energy value (left), but with a huge difference in computation effort (right).

angular momentum than those occupied in the atom), further improves the energetics, as shown in Fig. 2.5 (right) via TZ2P compared to TZ. This is because polarization functions have by definition more angular nodal planes than occupied atomic orbitals, and thus ensure that the orbitals can distort from their original atomic symmetry and better adapt to solid or molecular environments.

2.7 k - space

In addition to the Monkhorst-Pack scheme [39] for generating sample k-points, see section 2.3, a series of schemes based on the tetrahedron method [50]−[53] are also widely in use. The goal of both approaches (i.e. Monkhorst-Pack and tetrahedron method) is to sample the Brillouin Zone (BZ) as accurately as possible, using fewer sample k-points. With the Monkhorst-Pack scheme, the BZ is divided into an equispaced grid of k-points, while with the tetrahedron method, the BZ is divided into tetrahedral volumes, not necessarily equivalent, in three dimensions [50],[51],[53] or triangles [52] in two dimensions. As such, the k-points generated are to some degree dependent on the symmetry operations of the crystal. Less symmetric crystal systems tend to require more k-points than highly symmetric ones. This is not the case with the Monkhorst-Pack scheme,

where the k-points are generated independently, regardless of the type of crystal.

A linear tetrahedron contains the k-points at its corners and sides [51]. As such, though it yields accurate results, it is presumed to be computationally expensive. An alternative approach is to divide the linear tetrahedron into eight smaller tetrahedrons, in what is called quadratic tetrahedrons [53]. Thus, the quadratic tetrahedron contains k-points at the corners where interpolation is used for the sides. This approach has been reported to be of comparable accuracy with the linear tetrahedron, while at the same time it results in large savings of computational time.

For example, for a simple cubic 3D crystal, the smallest number of k-points generated, parametrized in the BAND program [54] as KSPACE = 3, would give 10 k-points. This can be understood from six quadratic tetrahedrons that can be constructed and where the net number of unique k-points equals 10. With a parametrization of KSPACE = 4, additional k-points at the sides would be added. This effectively sees each of the original tetrahedrons to be further split into four tetrahedrons. As such, the total number of unique k-points equals 20. With KSPACE = 5, the original tetrahedron (i.e., the tetrahedron of KSPACE = 3) is split into sixteen tetrahedrons, resulting in 35 unique k-points. This can be imagined as follows. Assume that scaled coordinates of the corners of a given tetrahedon with KSPACE = 3 are {(1,0,0), (1,0,1), (0,0,1), (1,1,1)}. With KSPACE = 4, this set expands to {(1,0,0), ($\frac{1}{2}$,0,$\frac{1}{2}$), (0,0,1), ($\frac{1}{2}$,0,1), (1,0,1), (1,0,$\frac{1}{2}$), (1,$\frac{1}{2}$,1), (1,1,1), (1,$\frac{1}{2}$,$\frac{1}{2}$)}. Now, consider a single finer tetrahedon from the latter set, say one with the coordinates {($\frac{1}{2}$,0,$\frac{1}{2}$), (0,0,1), ($\frac{1}{2}$,0,1), (1,0,$\frac{1}{2}$)}. With KSPACE = 5, this set expands to { ($\frac{1}{2}$,0,$\frac{1}{2}$), ($\frac{1}{4}$,0,$\frac{3}{4}$), ($\frac{1}{4}$,0,1), ($\frac{3}{4}$,0,$\frac{3}{4}$), ($\frac{3}{4}$,0,$\frac{1}{2}$), ($\frac{1}{2}$,0,$\frac{3}{4}$)}. Similarly, the corresponding lists can be imagined with the other three finer tetrahedrons. So, undoubtedly, KSPACE = 5 offers a superior sampling (accuracy) when compared with KSPACES values of 3 and 4, but at the expense of a higher computational time.

Such an involvement of half integer k-points with the tetrahedron approach makes it quite a superior method for providing spectral (boundary related optical) properties when compared with the special-point (Monkhorst-Pack) scheme [51]. As it is presented in section 2.3, it is not necessary that the sample k-points generated with the Monkhorst-Pack scheme involve half integers. A body centered cubic 3D crystal is treated in a similar fashion as the simple cubic (sc), discussed above. However, with a face centered cubic 3D crystal, twelve tetrahedrons can be constructed as compared to six for sc (or bcc), even with KSPACE = 3. This makes the number of unique k-points equal to 15, 34, and 65, respectively, with KSPACES values of 3, 4, and 5. In 2D cases (surfaces), a highly symmetric lattice is the square lattice, followed by rectangles, and so on. For a square lattice, the BZ is divided into 2, 8, and 32 triangles, respectively, with KSPACE values of 3, 4, and 5. The corresponding number of unique k-points are 4, 10, and 15, respectively. Alternatively, this can be described as follows. A 1×1 square lattice with KSPACE = 3 forms a 2×2 set of finer square lattices with KSPACE = 4, and a 4×4 set of square lattices with

KSPACE = 5. Of all k-points from the sets, only symmetry unique points are selected. The same approach works with rectangular lattices. But due to lower symmetry, the symmetry unique points turn out to be larger with rectangular lattices than with the square lattices.
Such a generation of k-points improves the energetics of the eigenvalues, in Eqn. (2.58), which would take the form

$$\varepsilon_i = \sum\nolimits_{k,n} w_{kn}\varepsilon_{ikn}, \tag{2.60}$$

where w_{kn} is a carefully chosen weight factor, and k and n run over k-points and energy bands, respectively.

Chapter 3

Properties

3.1 Charges

There are different schemes for estimating atomic charges from the calculated electron density depending on whether the basis functions are centered on atoms or not [55]-[62]. In this section, a brief analysis of the scope and merits of the two classes of methods will be put forth.

3.1.1 Bader analysis

The original algorithm by Bader [55] is devoted to determining critical points given by

$$\nabla n(\mathbf{r_c}) = 0, \tag{3.1}$$

and then characterize the critical points by calculating the Hessian matrix of the density, $\nabla^2 n(\mathbf{r})|_{\mathbf{r}=\mathbf{r}_c}$. Based on the obtained points, the density is partitioned into volumes Ω_j assigned to each atom j. The regions of space assigned to different atoms are separated by zero flux surfaces $S(\mathbf{r_s})$ satisfying the relation

$$\nabla n(\mathbf{r_s}) \cdot \hat{1}(\mathbf{r_s}) = 0, \tag{3.2}$$

where $\hat{1}$ is a unit vector normal to S. The corresponding charge enclosed within each region is obtained as

$$Q = \int_{\Omega_j} n(\mathbf{r}) d\mathbf{r}. \tag{3.3}$$

However, because of these explicit calculations the algorithm is restricted to small systems. There are various algorithms [56]-[58] further developed avoiding the calculations of critical points as well as explicit construction of zero flux surfaces. These later algorithms use grid points instead of critical points to partition the density to each atom and the corresponding charges are obtained as

$$Q = \sum_{i \epsilon \Omega_j} n(\mathbf{r}_i) \Delta \mathbf{r}_i, \tag{3.4}$$

where i runs over the grid points contained in the region Ω_j assigned to atom j.

3.1.2 Mulliken analysis

The Mulliken analysis is a typical choice for wave functions expressed as a linear combination of centered basis functions. The concept behind this approach [59] can be seen as follows. Consider a wave function of a molecule given as

$$\psi_{mo}(\mathbf{r}) = c_m\eta_m(\mathbf{r}) + c_o\eta_o(\mathbf{r}), \tag{3.5}$$

i.e., as a linear combination of two basis functions η_m and η_o. This would lead to an expression for the total charge,

$$\int |\psi_{mo}(\mathbf{r})|^2 d\mathbf{r} = N_{mo} = N_m + N_o + \int (c_m^* c_o \eta_m^* \eta_o + c_o^* c_m \eta_o^* \eta_m) d\mathbf{r}, \tag{3.6}$$

where $N_m = \int |c_m|^2 |\eta_m(\mathbf{r})|^2 \mathrm{d}\mathbf{r}$ and $N_o = \int |c_o|^2 |\eta_o(\mathbf{r})|^2 \mathrm{d}\mathbf{r}$ are charges localized on atoms m and o, and the term $\int (c_m^* c_o \eta_m^* \eta_o + c_o^* c_m \eta_o^* \eta_m) \mathrm{d}\mathbf{r}$, hereafter denoted as $2\int S_{mo}(\mathbf{r}) \mathrm{d}\mathbf{r}$, is an overlap contribution. When S_{mo} is positive, the nature of the overlap is called antibonding while when S_{mo} is negative, it is called bonding.
Further insight can be gained by considering the three main types of molecular states, i.e., bonding (B), antibonding (AB), and non-bonding (NB) states, as follows. Assume, in the bonding state, that the charges are expressed as

$$N_{mo}^B = N_m^B + N_o^B + 2\int S_{mo}^B(\mathbf{r}) d\mathbf{r}, \tag{3.7}$$

where S_{mo}^B is negative. In the antibonding state,

$$N_{mo}^{AB} = N_m^{AB} + N_o^{AB} + 2\int S_{mo}^{AB}(\mathbf{r}) d\mathbf{r}, \tag{3.8}$$

where S_{mo}^{AB} is positive. In the non-bonding state,

$$N_{mo}^{NB} = N_m^{NB} + N_o^{NB}, \tag{3.9}$$

i.e., there is no overlap term. The sum of Eqns. (3.7) - (3.9) gives the charges on the atoms of the molecule. The bonding state is expected to be where the overlap charge is mostly located on the electronegative atom while the antibonding state is where the overlap charge is mostly located on the electropositive atom. Further, the bonding state is a charge gain and antibonding state is a charge loss. This can be justified by considering the CO molecule, where a charge of $5.774e$ is assigned to the C atom and a charge of $8.226e$ is assigned to the O atom. Here, we have used the BAND program [54].
For an electron wave function which is expressed as a linear combination of basis functions η,

$$\psi_i(\mathbf{r}) = \sum\nolimits_{\mu=1}^{N} c_{\mu i}\eta_\mu(\mathbf{r}), \tag{3.10}$$

one has

$$\int |\psi_i(\mathbf{r})|^2 d\mathbf{r} = \sum\nolimits_{\mu=1}^{N} |c_{\mu i}|^2 \int |\eta_\mu(\mathbf{r})|^2 d\mathbf{r} + \sum\nolimits_{\mu\nu}^{\frac{N}{2}} \int S_{\mu\nu}(\mathbf{r}) d\mathbf{r}. \tag{3.11}$$

A sum over all the electrons of an atom gives the corresponding charge,

$$Z_A = \sum_i \int |\psi_i(\mathbf{r})|^2 d\mathbf{r} = \sum_i \sum_{\mu=1}^{N} |c_{\mu i}|^2 \int |\eta_\mu(\mathbf{r})|^2 d\mathbf{r} + \sum_i \sum_{\mu\nu}^{\frac{N}{2}} \int S_{\mu\nu}(\mathbf{r}) d\mathbf{r}, \tag{3.12}$$

A being m or o. As an example we consider the C and O atoms of a CO molecule, where the electron configuration, as calculated with a Mulliken analysis, is given as $1s^2 2s^{1.899} 2p^{1.875}$ and $1s^2 2s^{1.835} 2p^{4.391}$, respectively. For a summary, see Fig. 3.1 and Table 3.1.

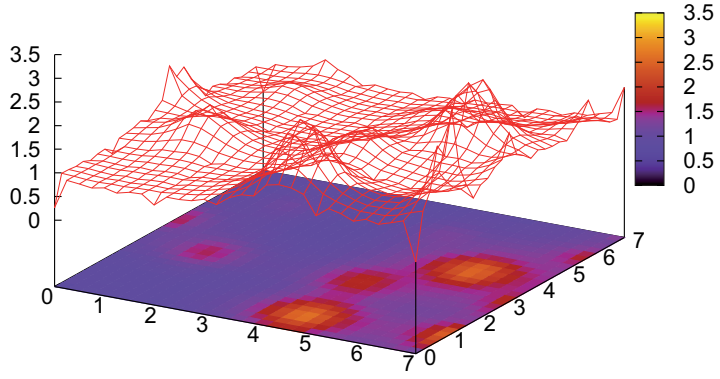

Figure 3.1: As an example, an electron density plot is presented where yellow color shows areas of density maxima, while dark color shows areas of density minima. Both regions contain critical points $\mathbf{r}_c$ which are then used as input for dividing into Bader regions.

Table 3.1: Summary of the discussion in this section.

Method	charge	
	H	Cl
Bader(3.1.1)	0.675	17.323
Mulliken(3.1.2)	0.875	17.125

3.2 Density of states

Among functions which require integration over the Brillioun Zone (BZ) is the density of states (DOS) which is obtained from the band structure [38],[52],[53].

For numerical implementation, the integration is replaced by summation over discrete energy levels as

$$D(\varepsilon) = \sum\nolimits_i \delta(\varepsilon - \varepsilon_i(\mathbf{k})). \tag{3.13}$$

3.2.1 Local DOS

Unit cells often contain atoms of different types, where the wave functions are expressed as linear combinations of basis functions, which may be plane waves of the form described in section 2.3 or atomic orbitals in section 2.6. The wave functions are required to be normalized [63],

$$\int |\psi(\mathbf{r})|^2 d\mathbf{r} = 1, \tag{3.14}$$

where $\psi(\mathbf{r}) = \sum_a \sum_i c_{ai} \phi_i^a(\mathbf{r})$. $D(\varepsilon)$, Eqn. (3.13), can now be expressed as a sum over all atoms of a unit cell, i.e., $D(\varepsilon) = \sum_a d_a(\varepsilon)$. Here a runs over the different atoms and $d_a(\varepsilon)$ can be interpreted as a local density of states.

3.2.2 Projected DOS

Furthermore, the DOS on an atom can be regarded as a sum over a state resolved density of states (PDOS), i.e., $d_a(\varepsilon) = \sum_l c_{la} \wp_l(\varepsilon)$.

Perhaps the most important point to be emphasized is the type of approximations used for the δ functions, i.e., $\delta(\varepsilon\text{-}\varepsilon_i(\mathbf{k}))$. Among the widely used approximations are Gaussian broadening [64],[65] or some weight factor of the form $w_n(\mathbf{k})$ [51],[63],[50]. Depending on the type of basis set used, usually either of the approximations mentioned above are used. For example, with a plane wave basis and the Monkhorst-Pack scheme of k-point sampling, usually Gaussian broadening is preferred. Weight factors $w_n(\mathbf{k})$ are typically chosen when an atomic orbital basis and a tetrahedron approach for k-point sampling is used. The DOS provides a valuable analysis where insight about reactive tendencies, energy gaps, etc. of a system is obtained. (See Fig. (3.2).)

3.3 Vibrations

A general discussion of molecular vibrations can be found in several textbooks, see e.g. [66]. Possible implementations of methods for the calculation of vibrational frequencies with DFT based packages is also described in the relevant literature [67],[68]. An effort by Ratajczak et al. [69] needs to be underscored here. They have presented a relation between vibrational frequencies and bond energies. A calculation based on [68] (Table 3.2) for selected small molecules reveals clear correlations between bond distances, bond energies, and vibrational frequencies. Even for larger systems, correlations have been found between the bond energy and vibrational frequencies [69]. Based on these findings, it would be of interest to study possible relations between atomic charges and vibrational frequencies. This has been one of the issues in the papers not included in this

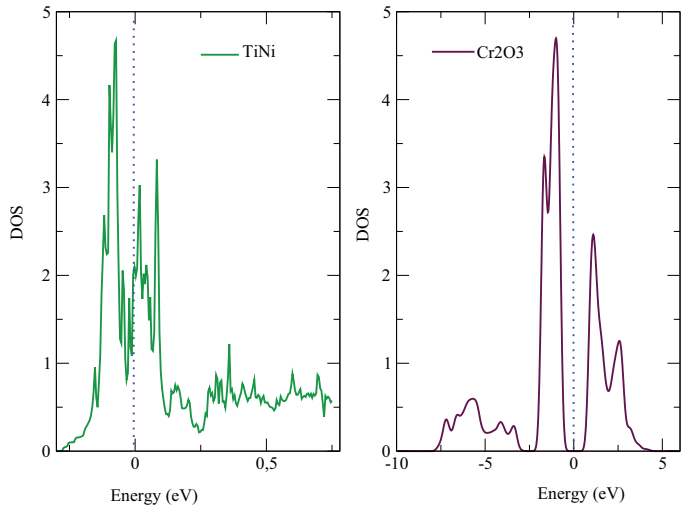

Figure 3.2: (Left) DOS of a TiNi system calculated based on the $w_n(\mathbf{k})$ approach, displaying a non-zero DOS at the Fermi level. (Right) DOS of Cr_2O_3 calculated with the gaussian broadening approach, displaying zero DOS at the Fermi level. This shows the presence of an energy gap.

thesis. Hence, vibrational frequencies coupled with atomic charges etc. could also represent a valuable tool in the analysis of reaction studies.

3.4 Reaction Paths

Reaction paths are minimum energy paths (MEP) between two states, i.e., between given initial and final states. As such the same procedure can be followed for the MEP calculations of dissociation, diffusion etc. Over the years, various schemes for calculating MEP have been proposed [70]-[78]. These include nudged elastic band (NEB) method [70] - [74], [77], adaptive nudged elastic band (ANEB) [75], doubly nudged elastic band (DNEB) [76] etc. With the NEB method, the MEP is obtained by constructing a set of images (replicas) between the initial and final states. Since the process of geometry optimization involves minimization of the forces acting on the images, a spring interaction between adjacent images is added to ensure continuity of the path and avoid the sliding-down of images to energy minima. Only the tangential component of the spring force is included in the total force. The difference between DNEB and NEB is in the degree of the spring force added to the total force [78].

Table 3.2: Correlation between bond energy (BE), bond distance (BD), and vibrational frequency (VF) for a selection of small molecules.

Molecule	BE (eV)	BD (Å)	VF (cm^{-1})
H_2	867.6	0.75	6998
OH	632.5	0.98	5102
N_2	232.7	1.10	1877
O_2	217.8	1.20	1756

3.5 Potential energy surfaces

A general goal in our studies is to localize various stationary points on the potential energy surface (PES). These could represent different adsorption sites for a given adsorbate on a given surface (energy minima), and transition states connecting these adsorption sites (saddle points), see Fig. 3.3 (b). Several factors will influence the accuracy of our description of the PES, such as convergence criteria, minimization algorithms (e.g. BFGS, conjugate gradient, quasi-newton[79]) , input geometries, choice of energy functionals, as well as other technical parameters of the program package being used. While precise error estimates cannot be made, one should typically be prepared to see errors in calculated energies of the order of a few tenths of an eV [80],[81].

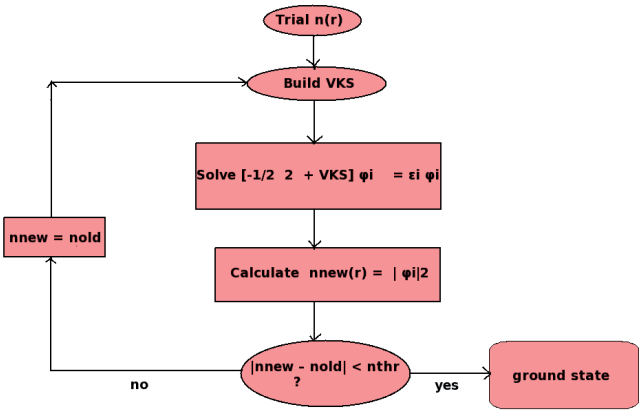

(a)

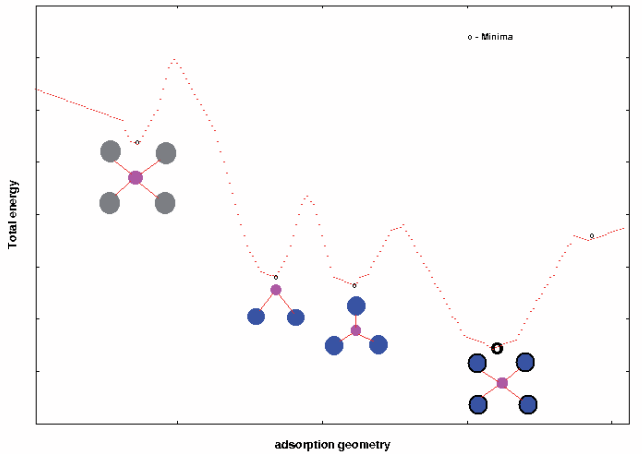

(b)

Figure 3.3: (a) Solution of the Kohn - Sham equations showing convergence criteria and process. (b) Different local minima corresponding to different adsorption sites as indicated. The differently colored circles denote the possibility of different atoms in a unit cell.

Chapter 4

Systems of interest and the challenges

4.1 Corundum type surfaces

Characterization of corundum structures has long been a topic of interest [82]. However, timely modeling must be based on advances from the latest experimental investigations. Experiments often present the structure of corundum oxides based on the growth of these oxides on a base metal, e.g., Cr_2O_3 on Cr(110) [83] etc. Nevertheless, the interesting phenomenon here is that several corundum type oxides M_2O_3 where M = Ti, V, Al, Fe, or Cr are reported to have more or less similar structures, i.e., R3$\bar{c}$ group [84]. Hence, interestingly, it can be expected that a study on a polar surface of any of these corundum surfaces can give insight about the others. The characterization of the crystal structure of these corundum systems is still subject to continuous improvement. In this study, we address the reactive properties of some selected molecules on the polar (0001) surface of Cr_2O_3.

4.2 Bimetallic surfaces

4.2.1 TiNi

Some knowledge of the properties of Ti and Ni single crystals is beneficiary for the investigation and analysis of properties of TiNi alloys. Calculation of equilibrium properties such as the lattice constant and bulk modulus is nowadays a routine but common means of checking the accuracy of methods used. Table 4.1 consists of some of these calculations, including comparison with literature values.
The bulk moduli are estimated from a Birch-Murnaghan fit [85],[86] as

$$E(V) \simeq E_0 + \frac{9}{8} B_0 V_0 [\{\frac{V_0}{V}\}^{2/3} - 1]^2, \tag{4.1}$$

or from fitting the energy curve with respect to the lattice constant a as

$$E(a) \simeq E_0 + \beta(a - a_0)^2, \tag{4.2}$$

Table 4.1: Heat of formation H_f (eV) and bulk modulus B (GPa) for bulk Ti and Ni, as well as the monoclinic and B_2 phases of TiNi. a, b, and c are lattice constants (Å).

Crystal	Phase	H_f	B	a	b	c
Ti	hcp		124.12[a],133.75[b]	2.91		4.89
			110			
	bcc		227.3[a],240[b]	3.2		
	fcc		213.7[a],212.6[b]	4.1		
Ni	fcc		241.2[a],	3.45		
			180,			
TiNi	mono	0.80	119.9	2.89	4.69	4.10
	B_2	0.57	160.67[a],163.7[b]	3.0		
			140.3[c],157.8[d]			

[a] calculated by Eqn. (4.1). [b] calculated by Eqn. (4.2).
[c] experimental result from Ref. [88]. [d] from Ref. [87].

where E_0, B_0, and V_0 are equilibrium values of energy, bulk modulus, and volume. In the latter case, the bulk modulus was estimated as $B_0 = 2C\beta/9a$ where $C = 1$, 2, and 4 for simple cubic, body centered cubic, and face centered cubic structures, respectively. For hexagonal structures, $B_0 = \beta/\sqrt{3}c$. The accuracy of such estimates depends on a number of factors. For example, we have assumed $\frac{\partial B}{\partial P} \mid_T \equiv 1$ which is a multiplicative constant in Eqn. (4.1) as stated in [85]. For best accuracy, the value of this constant could be different from one. Thus, the trend in the estimated values of the bulk moduli would be the most reliable outcome. With the method we have employed, these values are slightly overestimated (presented in Table 4.1).
The transition pressure between two structures could be estimated from the slope of a tangent line connecting two points with the same Gibbs free energy. Starting with the general form of Gibbs free energy,

$$G(P,T) = E + PV - TS(P,T), \tag{4.3}$$

it reduces to the form

$$G(P) = E + PV \tag{4.4}$$

for our study which is carried out at $T = 0$ K. Here, $E = E(V)$ for a total energy calculated at $P = 0$ or $E = E(V,P) \rightarrow E'(V)$ for a total energy calculated at finite pressure. Next, one assumes the Gibbs free energy shared by the points

on the tangent line to be zero. The transition pressure could then be estimated as

$$P = -\frac{\Delta E}{\Delta V}, \tag{4.5}$$

where $\Delta E = E_2 - E_1$ is the energy difference between the two equilibrium structures, and $\Delta V = V_2 - V_1$ is the corresponding volume difference.

4.2.2 PtCe

Rare earths are of importance not only because of properties such as variable valency, magnetic Kondo effect etc. that they introduce to the alloy system, but also from the point of view of controlling certain properties of a given base metal. Because they are not abundantly available, they are often required to be used in small amounts. As such, they typical prove to be of high importance for surface property modifications, where only a few layers can significantly alter the reactive properties of the base metals.

The challenge, though, is that different rare earth coverages could result in different alloy structures, and as a concequence could lead to different types of influence on the properties of the base metal. Moreover, the spatially extended nature of the f electrons has also been a difficulty both from an experimental and a theoretical point of view [89].

4.3 Metallic surfaces

An accurate description of crystal structures of single metal systems has already been well established. However, a study of the interaction between a metal of interest and a molecule of interest is a never ending topic. The challenge though is how to address industrially relevant reactions of large molecules with metals with model studies of reactions of small molecules with metal systems. A continued improvement on establishing methods for addressing the industrial interest more accurately gives a continuous renewed research interest.

Nevertheless, even with the present advance, some useful insight can be obtained from the interaction of small molecules with the metals, as they are building blocks of large molecules or polymers. A smart analysis (i.e., the use of different analysis tools and approaches) is the key to achieving this. An example is a study of the interaction of C_2H_4 with Pd, Rh, and Pt surfaces, which not only provides the influence of the molecule on these widely used transition metals, but also offers insight into the reaction of polyethylene on these surfaces. This has been addressed in the papers not included in this theses.

Chapter 5

Conclusions

This thesis investigates various ranges of reactivities of various molecules on various surfaces of interest. A brief summary of typical results may be described as follows. Atomic adsorbates (Paper I) degrade the corrosion inhibiting ability of the $Cr_2O_3(0001)$ surface. The interaction of various small molecules with the $Cr_2O_3(0001)$ surface (Paper II) is found to result in various catalytic chemical complexes. Notable is the growth of a single hexagonal 2D lattice of H_2O layer and honeycomb lattice of Cl atoms. Sulfuric acid generally reacts preferably with donor species (metallic systems). As a consequence, an appropriate surface treatment mechanism (Paper III) as oxidizing a surface could prevent it from the attack by these species.

Doping of a NiTi shape memory surface would lead to an improved biofunctionality performance of the alloy (Paper IV). Different surface indices of the NiTi shape memory surface are found to have different reactivities to oxygen. As such, the oxidation of the different surface indices by the oxygen leads to different initial growths of various types of TiO_2 surfaces. The impact of using different approximations in DFT calculations (Paper V) becomes small when considering differences such as energy differences (typically adsorption energies), charge transfers etc. Different coverages of Ce used to make an intermetallic alloy with Pt as base metal determines the type of structure that the alloy would resume. As a consequence, the reactive property of the alloy would be significantly influenced (Paper VI).

Bibliography

[1] K. Schwarz, P. Blaha, *Comput. Mater. Sci.* **28**, 259 (2003).

[2] J. Ihm, *Rep. Prog. Phys.* **51**, 105 (1988).

[3] G.R. Anstis, P. Chantikul, B.R. Lawn, and D.B. Marshall, *J. Am. Ceram. Soc.* **64**, 533 (1981).

[4] J.P. Buban, K. Matsunaga, J. Chen, N. Shibata, W.Y. Ching, T. Yamamoto, and Y. Ikuhara, *Science* **311**, 212 (2006).

[5] F.T. da Silva, M.A.N. Zacché, H.S. de Amorim, *Materials Research* **10**, 63 (2007).

[6] M.A. Amin, K.F. Khaled, Q. Mohsen, H.A. Arida, *Corros. Sci.* **52**, 1684 (2010).

[7] I.B. Obot, N.O. Obi-Egbedi, *Corros. Sci.* **52**, 198 (2010).

[8] H. Carsten, S. Stefan, *J. Chem. Phys.* **131**, 224303 (2009).

[9] T. G.-Lezana, P. Honvault, P.G. Jambrina, F.J. Aoiz, J.-M. Launay, *J. Chem. Phys.* **131**, 044315 (2009).

[10] P.R. Davies, M. Bowker, *Catal. Today* **154**, 31 (2010).

[11] S. Zweidinger, J.P. Hofmann, O. Balmes, E. Lundgren, H. Over, *J. Catal.* **272**, 169 (2010).

[12] S.C. Lo, S.K. Tanwar, A.M. Chaka, T.P. Trainor, *Phys. Rev. B* **75**, 075425 (2007).

[13] F. Sinapi, T. Issakova, J. Delhalle, Z. Mekhalif, *Thin Solid films* **515**, 6833 (2007).

[14] R.I. Masel, *Principles of adsorption and reaction on solid surfaces*(Wiley, New York, 1996).

[15] D.R. Hartree, *Proc. Cambridge Phil. Soc.* **24**, 89,111,426 (1928).

[16] V. Fock, *Z. Phys.* **61**, 126 (1930).

[17] J.C. Slater, *Phys. Rev.* **34**, 1293 (1929).

[18] C.C.J. Roothaan, *Rev. Mod. Phys.* **23**, 69 (1951).

[19] P. Hohenberg and W. Kohn, *Phys. Rev.* **136**, 3B (1964).

[20] L. H. Thomas, *Proc. Cambridge. Phil. Roy. Soc.* **23**, 542 (1927).

[21] E. Fermi, *Rend. Accad. Naz. Lincei* **6**, 602 (1927).

[22] R.G. Parr and W. Yang, *Density-Functional Theory of Atoms and Molecules* (Oxford University Press, 1989.)

[23] W. Kohn and L.J. Sham, *Phys. Rev.* **140**, 1133A (1965).

[24] C.F. Guerra, O. Visser, J.G. Snijders, G. te Velde, and E.J. Baerends, *Parallelisation of the Amsterdam Density Functional Program* (The Netherlands, 2000.)

[25] E. van Lenthe. http://www.scm.com/Doc/vlenthe.pdf, 1996.

[26] P.H.T. Philipsen, E. van Lenthe, J.G. Snijders, and E.J. Baerends, *Phys. rev. B* **56**, 13556 (1997).

[27] J.P. Perdew and W. Yue, *Phys. Rev. B* **33**, 8800 (1986).

[28] A.D. Becke, *Phys. Rev. A* **38**, 3098 (1988).

[29] C. Lee, W. Yang, and R.G. Parr, *Phys. Rev. B* **37**, 785 (1988).

[30] J.P. Perdew and Y. Wang, *Phys. Rev. B* **46**, 12947 (1992).

[31] J.P. Perdew, J.A. Chevary, S.H. Vosko, K.A. Jackson, M.R. Pederson, D.J. Singh, and C. Fiolhais, *Phys. Rev. B* **46**, 6671 (1992).

[32] J.P. Perdew, K. Burke, and M. Ernzerhof, *Phys. Rev. Lett.* **77**, 3865 (1996).

[33] B. Hammer, L.B. Hansen, and J.K. Nørskov, *Phys. Rev. B* **59**, 7413 (1999).

[34] P.A.M. Dirac, *Proc. Camb. Philos. Soc.* **26**, 376 (1930).

[35] M. Rasolt and D.J.W. Geldart, *Phys. Rev. B* **34**, 1325 (1986).

[36] S.H. Vosko, L. Wilk, and M. Nusair, *Canadian Journal of Physics* **58**, 1200 (1980).

[37] O. Gunnarsson and B.I. Lundqvist, *Phys. Rev. B* **13**, 4274 (1976).

[38] S.R. Elliott, *The Physics and Chemistry of Solids* (John Wiley and Sons Ltd., England, 1998).

[39] H.J. Monkhorst and J.D. Pack, *Phys. Rev. B* **13**, 5188 (1986).

[40] R.W. Shaw and W.A. Harrison, *Phys. Rev.* **163**, 604 (1967).

[41] D.R. Hamann, M. Schlüter, and C. Chiang, *Phys. Rev. Lett.* **43**, 1494 (1979).

[42] L. Kleinman and D.M. Bylander, *Phys. Rev. Lett.* **48**, 1425 (1982).

[43] D. Vanderbilt, *Phys. Rev. B.* **41**, 7892 (1990).

[44] K.N. Nigussa, J.A. Støvneng, Comp. Phys. Commun. (2010), doi:10.1016/j.cpc.2010.12.027.

[45] W. Koch, M.C. Holthausen, *A Chemist's Guide to Density Functional Theory* (2^{nd} edn., Wiley-Vch, Weinheim, 2001).

[46] R.M. Martin, *Electronic Structure: Basic Theory and Practical Methods* (Cambridge University Press, Cambridge, 2004).

[47] G. te Velde and E.J. Baerends, *Phys. Rev. B.* **44**, 7888 (1991).

[48] F. Herman and S. Skillman, *Atomic Structure Calculations* (Prentice-Hall, Englewood Cliffs, NJ, 1963).

[49] J. Junquera, Ó. Paz, D. Sánchez-Portal, and E. Artacho, *Phys. Rev. B.* **64**, 235111 (2001).

[50] O. Jepson and O.K. Anderson, *Solid State Communications* **9**, 1763 (1971).

[51] P.E. Blöchl, O. Jepsen, and O.K. Andersen, *Phys. Rev. B* **49**, 16223 (1994).

[52] G. Wiesenekker, G. te Velde, and E.J. Baerends, *J. Phys. C: Solid State Phys.* **21**, 4263 (1988).

[53] G. Wiesenekker and E.J. Baerends, *J. Phys.: Condens. Matter* **3**, 6721 (1991).

[54] http://www.scm.com.

[55] R.F.W. Bader, Atoms in Molecules : A Quantum Theory (Oxford University Press, UK, 1990).

[56] G. Henkelman, A. Arnaldsson, and H. Jonsson, *Comput. Mat. Sci.* **36**, 354 (2006).

[57] E. Sanville, S.D. Kenny, R. Smith, and G. Henkelman, *J. Comput. Chem.* **28**, 899 (2007).

[58] W. Tang, E. Sanville and G. Henkelman, *J. Phys.: Condens. Matter* **21**, 084204 (2009).

[59] R.S. Mulliken, *J. Chem. Phys.* **23**, 1833 (1955).

[60] W.J. Mortier, S.K. Ghosh, and S. Shankar, *J. Am. Chem. Soc.* **108**, 4315 (1986).

[61] M. Gussoni, M.N. Ramos, C. Castiglioni, and G. Zerbi, *Chem. Phys. Lett.* **142**, 515 (1987).

[62] M. Basma, S. Sundara, D. Çalgan, T. Vernali, and R.J. Woods, *J. Comput. Chem.* **22**, 1125 (2001).

[63] B. te Velde. http://www.scm.com/Doc/BANDthesis/BANDThesis.pdf, 1990.

[64] M. Methfessel and A.T. Paxton, *Phys. Rev. B* **40**, 3616 (1989).

[65] R.J. Needs, R.M. Martin, and O.H. Nielsen, *Phys. Rev. B* **33**, 3778 (1986).

[66] P. Atkins and R. Friedman, *Molecular Quantum Mechanics* 4^{th} *edn* (Oxford University Press, UK, 2005).

[67] D.E. Jiang and E.A. Carter, *Surf. Sci.* **583**, 60 (2005).

[68] T. Frederiksen, M. Paulsson, M. Brandbyge, and A.-P. Jauho, *Phys. Rev. B* **75**, 205413 (2007).

[69] H. Ratajczak, W.J. O.-Thomas, and C.N.R. Rao, *Chem. Phys.* **17**, 197 (1976).

[70] G. Mills and H. Jónsson, *Phys. Rev. Lett.* **72**, 1124 (1994).

[71] G. Mills, H. Jónsson, and G.K. Schenter, *Surf. Sci.* **324**, 305 (1995).

[72] H. Jonsson, G. Mills, and K. Jacobsen, *Nudged elastic band method for finding minimum energy paths of transitions*, in Classical and Quantum Dynamics in Condensed Phase Simulations, edited by B. Berne, G. Ciccoti, and D. Coker (World-Scientific, Singapore, 1998).

[73] G. Henkelman, B.P. Uberuaga, and H. Jónsson, *J. Chem. Phys.* **113**, 9901 (2000).

[74] G. Henkelman and H. Jónsson, *J. Chem. Phys.* **113**, 9978 (2000).

[75] P. Maragakis, S.A. Andreev, Y. Brumer, and D.R. Reichman, *J. Chem. Phys.* **117**, 4651 (2002).

[76] S.A. Trygubenko and D.J. Wales, *J. Chem. Phys.* **120**, 2082 (2004).

[77] N. G.-García, J. Pu, Á. G.-Lafont, J.M. Lluch, and D.G. Truhlar, *J. Chem. Theory Comput.* **2**, 895 (2006).

[78] D. Sheppard, R. Terrell, and G. Henkelman, *J. Chem. Phys.* **128**, 134106 (2008)

[79] W. Press, B. Flannery, S. Teukolsky, and W. Vetterling, *Numerical Recipes in Fortran* 2^{nd} *edn* (Cambridge University Press, Cambridge, 1992).

[80] J.A. White, D.M. Bird, M.C. Payne, and I. Stich, *Phys. Rev. Lett.* **73**, 1404 (1994).

[81] R.A. Olsen, G.J. Kroes, and E.J. Baerends, *J. Chem. Phys.* **11**, 11155 (1999).

[82] R. Wyckoff, *Crystal Structures, 2nd edn* (Interscience, New York, 1964).

[83] V. Maurice, S. Cadot and P. Marcus, *Surf. Sci.* **458**, 195 (2000).

[84] C. Ma and G.R. Rossman, *American Mineralogist* **94**, 841 (2009).

[85] F.D. Murnaghan, *Proc. Natl. Acad. Sci.* **30**, 244 (1944).

[86] F. Birch, *J. Geophys. Res.* **83 (B3)**, 1257 (1978).

[87] O. Mercier, K.N. Melton, G. Gremaud, and J.J. Hägl, *J. Appl. Phys.* **51**, 1833 (1980).

[88] G. Bihlmayer, R. Eibler, and A. Neckel, *Phys. Rev. B* **50**, 13113 (1994).

[89] D.J. Peterman, J.H. Weaver, M. Croft, and D.T. Peterson, *Phys. Rev. B* **27**, 808 (1983).

PAPER I

Adsorption of hydrogen, chlorine, and sulfur atoms on α-Cr_2O_3(0001) surfaces: A Density Functional Theory investigation

Submitted to Corrosion Science

Adsorption of hydrogen, chlorine, and sulfur atoms on α-Cr_2O_3(0001) surfaces: A Density Functional Theory investigation

K.N. Nigussa[a], K.L. Nielsen[b], Ø. Borck[a], J.A. Støvneng[a,*]

[a]*Department of Physics, NTNU, N-7491 Trondheim, Norway*
[b]*Sør–Trøndelag University College (HiST), N-7004 Trondheim, Norway*

Abstract

We have investigated the adsorption of atomic H, Cl, and S on the chromyl (Cr=O), oxygen (O), and chromium (Cr) terminated α-Cr_2O_3(0001) surfaces using density functional theory (DFT) calculations. The results show that these adsorbates chemisorb to the oxygen and chromium atoms of the surfaces. Adsorption of H is strongest on the Cr=O and O terminated surfaces. H preferably binds to the oxygen atoms of these surfaces. However, the adsorption of Cl and S atoms is strongest on the Cr terminated surface where the atoms preferably bond to the Cr atoms of the surface. These geometry preferences are explained by electronic structure analysis. Quantitative values of the adsorption energies and charge transfers are also presented. The adsorption of the adsorbates to the Cr atoms of the O terminated surface has resulted in significant outward relaxation of the Cr atoms, thereby causing significant bond breaking on the surface.

Keywords:

1. Introduction

Solid Cr_2O_3 has several and diverse applications: It is used as a coating for alloying [1], it is formed on the surface when chromium is added to yield corrosion resistant steel [2],[3], it has catalytic properties [4],[5], and it functions as a binder layer in the production of magnetic recording media [6]. In this paper, particular attention is given to cases under which the corrosion inhibiting quality of the oxide is affected. Today, there are several reports worldwide regarding the loss of resources due to the malfunctioning of the corrosion protective layers. To design solutions, it is important to have a detailed understanding of the various reactions leading to the problems.

There is consensus on the classification of various types of corrosion, as pitting [7], crevice [8], galvanic [9], and high temperature corrosion [10]. However, the underlying principle by which corrosion takes place is often one of the following: reduction of the surface oxygen, presence of acidic solution, or high concentration of anions surrounding the surface. That way, cation-anion sites are formed resulting in charge transfer between them. At a microscopic level, corrosion is manifested as cracks or voids [8],[9]. There have been experimental studies of corrosion carried out under reducing environment containing H cations [11], atmospheric environment containing Cl and S anions [12], acidic solutions containing Cl anions [13], and solid environment containing Cl anions [14]. In these studies, the analyses were carried out at the μm scale or greater. We approach the problem theoretically by analysing the interaction structures at the atomic level.

We choose atomic H, Cl, and S as the adsorbates to investigate the maximum effect of these species on the surface. Illustrations of bond breaking, substitutional bonds, and surface relaxation are atomic level equivalents of illustrating corrosion by cracks or voids at the μm level. In addition, we study the problem by calculating the corresponding charge exchanges. There is not a single conclusion regarding how the Cr_2O_3(0001) surface terminates. Wang et al. [15] have shown by thermodynamic phase calculations that the surface terminates by Cr atoms at low oxygen chemical potential and by Cr=O groups or O atoms at higher oxygen chemical potential. However, Rohrbach et al. [16] have concluded, on the basis of thermodynamic phase calculations, that the surface terminates by Cr atoms. An experimental study by Dillmann et al. [17] suggests that the surface terminates by Cr atoms or Cr=O groups at low

*Corresponding author: jon.stovneng@ntnu.no

or high oxygen concentrations, respectively. In summary, theoretical and experimental investigations agree that the surface terminates by Cr atoms at low oxygen chemical potential or high vacuum conditions. That may also be the reason that most studies carried out on this surface [18],[19] assume termination by Cr atoms.

However, the suggestions that the surface can be terminated by Cr=O groups or O atoms at high oxygen chemical potential cannot be ignored in the present study. Hence, our study considers all these terminations. A literature survey shows that most of the adsorptive studies carried out on Cr_2O_3 surfaces are either molecular or dissociative adsorptions of molecules. Only little attention has been given to atomic adsorptions. Among the few studies are H atom on O terminated $Cr_2O_3(0001)$ [20] and Cu on $Cr_2O_3(000\bar{1})$ [21]. In a study of adsorption of CO on $Cr_2O_3(11\bar{2}1)$ [22], it is established that CO has a high barrier energy of dissociation and always adsorbs in upright orientation, where only the C end of the molecule bonds with the surface atoms. By studying adsorption of H, Cl, and S atoms on the $Cr_2O_3(0001)$, we believe that in addition to gaining knowledge about the impact of these atoms on the surface, it serves to expand the literature on the details of interaction between atoms. Adsorption of atomic H on $V_2O_5(001)$ [23], Cr(110) [24], Cu(110) [25], and Pt(111) [26] has also been investigated previously.

On the basis of the existing literature, it is possible to make the following brief summary of the interaction between atomic H, Cl, and S and various surfaces. H atom prefers to react with surface oxygen atoms rather than with metals [23]. The presence of H_2O as a solvent environment catalytically blocks the interaction of the H atom with surface oxygen atoms [20]. H atom interacts with surface Cr atoms forming Cr_xH or CrH_x (x being 1 or 2) species on the surface depending on the H coverage [24]. The interaction of H atom with subsurface atoms is weak compared to its interaction with surface atoms [25]. Alloying decreases the strength of interaction of H atom with the surface [26]. Studies on the adsorption of Cl atom on Au(111) [27] and MgO(100) [28] indicate that the Cl atom possesses an electron acceptor nature and interacts preferably at a donor site. Studies on the adsorption of S on $TiO_2(110)$ [29], TiC(001) [30], Mo(110) [31], and Au(110) [32] all indicate that S atom interacts significantly with metal centers of the systems. Moreover, the adsorption of S on the oxygen rich $TiO_2(110)$ result in a substitutional bond between S and O atoms, where the S atom bonds to the surface Ti atoms by displacing some of the initial bonds between the oxygen and Ti atoms.

The paper is organized as follows. In section 2, we present our computational methods. A presentation of the results is included in section 3. In section 4, we present the discussion. We close the paper with some conclusions in section 5.

2. Computational Methods

2.1. Computational detail

The program DACAPO has been used to perform calculations based on density functional theory (DFT) (https://wiki.fysik.dtu.dk/dacapo) and ultrasoft pseudopotentials [33]. The wave function of the valence electrons is expanded in a plane wave basis with cutoff energy 400 eV. The selection of k-points in the irreducible Brillouin zone is done according to the Monkhorst-Pack scheme [34]. For bulk crystals, a $4 \times 4 \times 4$ k-point mesh is used. For (1×1), (2×1), and (2×2) surface unit cells, k-point meshes of $4 \times 4 \times 1$, $2 \times 4 \times 1$, and $2 \times 2 \times 1$ are used, respectively. The cutoff energy and k-point mesh are chosen on the basis of convergence tests for the bulk crystals and clean surface structures. Higher cutoff energies and denser k-point meshes result in negligible changes in total energies and geometries. The contributions of exchange and correlation to the total energy are calculated within the generalized gradient approximation (GGA) using the PW91 parametrization [35]. Geometries are relaxed with the BFGS algorithm [36] until the total force on all unconstrained atoms is below 0.05 eV/Å.

Artificial electrostatic effects are selfconsistently compensated by a dipole layer in the vacuum region between the slabs [37],[38]. We quantify the adsorption coverage in terms of adsorbed atoms per chromium atom at (or near) the surface. Hence, a coverage of one monolayer, $\Theta = 1$ ML, corresponds to one adsorbed atom per Cr=O, Cr, or CrO_3 unit, depending on the type of surface termination. We have used $\Theta = 1$, 0.5, and 0.25 ML for adsorption on (1×1), (2×1), and (2×2) surface unit cells, respectively. The solution of the Kohn-Sham equations provides the ground state of a given system in terms of occupied single particle states and corresponding energies. This forms the basis for a discussion of the energetics, and the electronic, magnetic, and structural features of the various combinations of the surface terminations and adsorbates that have been investigated in the present study.

Adsorption energies, per adsorbed atom, are defined as

$$E_{ads} = -(E_{SA} - E_S - E_A). \quad (1)$$

Here, E_S is the total energy per unit cell of the clean surface, E_A is the total energy per isolated atom, and E_{SA}

is the total energy per unit cell of the surface and adsorbate atom combined. With the chosen sign, an exothermic adsorption corresponds to $E_{ads} > 0$. Atomic charge and magnetic moment (i.e., spin) are calculated from the electron density $n(\mathbf{r})$, using the atoms-in-molecules approach developed by Bader [39]. To each atom j, a region of space Ω_j is assigned by starting close to the nucleus and following trajectories of steepest density descent, i.e., $-\nabla n$. The Bader atomic charge Q_j is then

$$Q_j = Z_j - \int_{\Omega_j} n(\mathbf{r}) d\mathbf{r} \tag{2}$$

where Z_j is the nuclear charge of atom j, including all electrons incorporated in the pseudopotential. Similarly, the Bader magnetic moment μ_j is given by

$$\mu_j = \int_{\Omega_j} (n_\uparrow(\mathbf{r}) - n_\downarrow(\mathbf{r})) d\mathbf{r}. \tag{3}$$

Here, $n_\uparrow$ and $n_\downarrow$ denote the density of spin-up and spin-down electrons, respectively. In all calculations, we allow spin polarization. The interaction between adsorbate atom and surface can be further conveniently described in terms of *electron density difference plots* and the *projected density of states*. The electron density difference $\Delta n(\mathbf{r})$ is defined as

$$\Delta n(\mathbf{r}) = n_{SA}(\mathbf{r}) - n_S(\mathbf{r}) - n_A(\mathbf{r}). \tag{4}$$

Here, $n_{SA}(\mathbf{r})$ is the electron density of the combined surface and adsorbate system, whereas n_S and n_A are the separate electron densities of the surface and adsorbate, respectively, evaluated with geometries corresponding to the combined system. Thus, $\Delta n > 0$ corresponds to a gain in electron density. The projected (or: state resolved) density of states (PDOS) $N_\alpha(\epsilon)$ is defined by

$$N_\alpha(\epsilon) = \sum_{i=1}^{\infty} |\langle \varphi_\alpha | \varphi_i \rangle|^2 \, \delta(\epsilon - \epsilon_i). \tag{5}$$

In this expression, $|\varphi_i\rangle$ are the Kohn-Sham eigenstates with energy ϵ_i, and $|\varphi_\alpha\rangle$ is a localized function, e.g., a 3d state on a Cr atom, a 2p state on an O atom etc. Insight into the nature of the adsorbate-substrate interaction can be obtained by a comparison of $N_\alpha(\epsilon)$ for different localized states $|\varphi_\alpha\rangle$, and for the clean surface and the combined surface-adsorbate system. In particular, the formation of socalled bonding and antibonding states upon adsorption on the various surfaces is reflected in peaks in $N_\alpha(\epsilon)$, for two or more localized orbitals $|\varphi_\alpha\rangle$ at a given energy ϵ. The orbital character of such bonding and antibonding states may be expressed in terms of the relative contributions $N_\alpha(\epsilon)$ for the different orbitals $|\varphi_\alpha\rangle$.

2.2. Surface models

The surface slab models are shown in Fig. 1 where we have denoted the Cr, Cr=O, and O terminated surfaces as surface A, B, and C, respectively. Common to all the surface models are the bottom three Cr_2O_3 layers. This assures that the models are based on the different ways of cleaving a surface from the same bulk-like underlying structure. The models differ in the atomic layers in the top part of the slabs. In model A, the slab ends with one additional Cr_2O_3 layer with atomic stacking sequence Cr-O_3-Cr. In models B and C, the slabs end with layers having atomic stacking sequences of Cr-O_3-Cr-O and Cr-O_3, respectively. In Fig. 2, the electronic structure of the surface slab models is illustrated in terms of the projected density of states (PDOS) of Cr 3d and O 2p states. For comparison, the PDOS of these states is also included for bulk Cr_2O_3. In subsequent sections, comparison will be made between the PDOS curves of these clean surfaces and the corresponding states after adsorption of atomic H, Cl, and S.

The same surface models have been considered previously [15]. In that study, it was shown theoretically that the surface terminations of models B and C are realistic under moderate to high oxygen chemical potentials, while that in model A was attributed to low oxygen chemical potentials. This validates the experimental conclusions [17].

Experimental investigations [40] showed a near hexagonal surface structure for the α-Cr_2O_3(0001) surface. Hence, we have constructed the models with hexagonal lattice parameters, where the oxygen atoms occupy the hexagonal close packed sites and the Cr atoms occupy 2/3 of the interstitial octahedral sites between the layers of the oxygen atoms. The bulk crystal structure can alternatively be described by a rhombohedral unit cell with two formula units [41] or a hexagonal unit cell with six formula units [42], where $a = 4.95$ Å and $c = 13.58$ Å [43]. The same antiferromagnetic ordering of $+ - +-$ in the bulk is applied at the surface. In Table 1, we summarize the differences between the three surface models by emphasizing the properties of the atoms in the top layers.

Table 1 highlights the main differences between the surface models. In the deeper layers of the models, not presented in Table 1, the Cr-O and Cr-Cr interlayer spacings approach the bulk values of 0.98 and 0.32 Å, respectively. The magnetic moments on the Cr atoms alternate at $\pm 2.62 \mu_B$ whereas it is zero on the O atoms. The bulk charges on the Cr and O atoms are 1.67 and $-1.12e$, respectively. These are all close to previously reported bulk values [44].

Table 1: Summary of geometric, magnetic, and electronic properties of the top layers of the three surface models. Values (in Å) for the three (A, C) or four (B) outermost neighbouring interlayer separations are included, cf Fig. 1. Bader atomic magnetic moments μ (μ_B) and atomic charges Q (e), based on Eq. (3) and (2), respectively, are included for the four outermost atomic layers.

Surface	Separation	Atom	μ	Q
A	Cr-1 - O-1 = 0.41	Cr-1	−3.44	1.36
	O-1 - Cr-2 = 1.05	O-1	0.05	−1.06
	Cr-2 - Cr-3 = 0.18	Cr-2	2.39	1.73
		Cr-3	−2.50	1.78
B	O-1 - Cr-1 = 1.58	O-1	0.50	−0.64
	Cr-1 - O-2 = 0.67	Cr-1	−2.18	1.83
	O-2 - Cr-2 = 1.10	O-2	0.02	−1.02
	Cr-2 - Cr-3 = 0.17	Cr-2	2.24	1.75
C	O-1 - Cr-1 = 0.64	O-1	0.05	−0.76
	Cr-1 - Cr-2 = 0.44	Cr-1	−0.68	1.96
	Cr-2 - O-2 = 1.06	Cr-2	−2.40	1.83
		O-2	−0.003	−1.09

3. Results

3.1. Adsorption of H atom

The isolated H atom has a half filled valence orbital, and is consequently strongly reactive towards most surfaces. On surface A, H binds to the surface Cr atom (site I in Fig. 3) or to the surface O atom (site II), the latter being in a hollow fcc coordination relative to the surface Cr atoms. Upon adsorption to the Cr atom, the H atom gains a charge of about $-0.34e$. This value is comparable to the gain of $-0.39e$ by an H atom on a Pt surface [26]. However, a notable difference is that H adsorbs at a hollow fcc site on the Pt surface due to the relatively small lattice constant. Our projected density of states (PDOS) calculations (Fig. 4 (I)) indicate that when H adsorbs to Cr, the valence states of H (the 1s orbital) shift to higher energy (i.e., lower binding energy) by about 3 eV. The origin of this shift is electrostatic. The Cr 3d band width is slightly increased, by about 0.5 eV. A site atop of Cr is prefered to bridge or hollow sites between surface Cr atoms. We believe this is due to the large surface unit cell of $Cr_2O_3(0001)$. The charge gained by the H atom, $-0.34e$, is considerable, but still sufficiently small to allow us to categorize the Cr-H bond of site I as covalent. A covalent bonding character is also suggested by the electron difference plots in Fig. 5, i.e., the spatial dependence of the electron distribution between the atoms.

Photoelectron spectroscopy (PES) experiments on Cr(110) [24] reveal a bonding state corresponding to Cr 3d - H 1s hybridization at binding energies 5.5 eV (low coverage) and 7.8 eV (high coverage), relative to the Fermi level. Our calculations predict bonding states at an energy of 3 eV below the Fermi level and antibonding states at an energy of 3 eV above the Fermi level. In the bonding state, the H 1s orbital dominates, with roughly 70% weight, and only about 30% for Cr 3d (mainly the $d_{x^2-y^2}$). In the antibonding state, the Cr 3d states (i.e., the d_{z^2} and $d_{x^2-y^2}$ species) dominate strongly.

In the case of adsorption at site II, the H atom bonds to the surface oxygen atom with an *sp* type O 2p - H 1s hybridization. Here the H atom donates while the surface O atom accepts electrons (see Table 2). The bonding state has about 60% O 2p (specifically the p_z species) - 40% H 1s character. The adsorption to the O atom here results in shifts of the O 2p, H 1s, and Cr 3d states by 4.5, 3.5, and 0.5 eV, respectively, towards lower energies. The adsorption energy in this site is about 1 eV smaller than in site I. That is likely due to the oxygen atoms being in a subsurface position in site II, about 0.4 Å below the surface Cr atoms. A similar reduction in adsorption energy, when comparing adsorption to subsurface sites with adsorption to surface sites, was also implied in a study on a different system [25].

On surface B, the H atom adsorbs in three different sites, III, IV, and V, with decreasing adsorption energy in that order. At the sites III and IV, the H atom bonds to surface oxygen atoms (see Figs. 3 (III) and (IV)). In each case, the bonding state has about 70% O 2p - 30% H 1s character. The H atom donates electrons while the O atom serves as the acceptor in this case. The Cr 3d states appear to shift slightly down the energy scale, by about 0.3 eV.

Although the O atoms of site IV are in a subsurface position, about 0.7 Å below the Cr atoms of site V, the adsorption energy of site IV is greater than that of site V. This is different from the trend observed at sites I and II, and also different from findings of a previous study [25]. One reason could be the presence of a dangling bond at the subsurface threefold coordinated oxygen atom.

Atomic H was found to reduce and stay intact with surfaces such as $VO_2(110)$ and vanadyl groups of $V_2O_3(0001)$ [23]. This is in line with our findings (sites III and IV), that atomic H reduces the surface by forming a stable OH group which could stay intact on the surface at temperatures of several hundreds of kelvin.

Table 2: Adsorption of H. Sites I - VII are illustrated in Fig. 3. Adsorption energies E_{ads} (eV) are based on Eq. (1). $d_{\mathrm{H-O}}$ and $d_{\mathrm{H-Cr}}$ are H-O and H-Cr bond lengths, respectively. The geometric, magnetic, and electronic influence on the surface upon adsorption of H is expressed in terms of changes in interlayer spacings Δz(Cr-O) and Δz(Cr-Cr) (underlined in Table 1), changes in atomic magnetic moments, $\Delta\mu$, and changes in atomic charges, ΔQ. (Units as in Table 1.) Superscripts: [a] (2×1) surface unit cell; [c] Ref. (20); [d] Ref. (24).

Surface	Site	E_{ads}	$d_{\mathrm{H-O}}$	$d_{\mathrm{H-Cr}}$	Δz(Cr-O)	Δz(Cr-Cr)	Atom	$\Delta\mu$	ΔQ
A	I	3.36,3.39[a]	2.71,2.68[a]	1.58,1.60[d]	0.13	0.01	H	0.02	−0.34
							O-1	0.05	0.66
							Cr-1	2.13	0.29
	II	2.34	0.99	2.48	−0.14	0.03	H	0.0	0.91
							O-1	−0.12	−0.56
							Cr-2	0.16	−0.16
B	III	4.12,4.14[a]	0.98,0.98[a]	2.39,2.40[a]	0.19	−0.01	H	0.0	0.88
							O-1	0.51	−0.91
							Cr-1	−0.38	−0.03
	IV	3.58	0.99	2.43	0.02	0.01	H	0.0	0.91
							O-2	−0.05	−0.56
							Cr-1	0.38	−0.06
	V	1.77	2.25	1.58	−0.10	0.09	H	0.03	−0.09
							O-1	−0.35	0.07
							Cr-1	1.17	−0.05
C	VI	4.00	0.98,0.95[c]	2.49	0.08	−0.02	H	0.0	0.90
							O-1	−0.06	−0.74
							Cr-1	1.65	0.0
	VII	2.33	2.56	1.57	−1.08	1.24	H	0.01	−0.22
							O-1	−0.04	−0.04
							Cr-1	0.29	−0.12

In the case of adsorption at site V, the bonding state of Cr 3d - H 1s hybridization is located below the antibonding state by about 6 eV. The adsorption geometry (Fig. 3 (V)) shows that the H atom is oriented above the hollow site between three surface Cr atoms but bonds only to one Cr atom. The missing bond to the other two Cr atoms is due to the large value of the lattice constant (mentioned already). This appears natural, since the preference of atomic H to adsorb at hollow sites in different metallic systems has been reported [26],[45]. The bonding state has a 60% H 1s - 40% Cr 3d character while the antibonding state has about 90% Cr 3d - 10% H 1s character. The Cr 3d band appears to widen by about 0.5 eV due to the CrH complex formed at the surface.

On surface C, the H atom adsorbs at sites VI and VII. Upon adsorption at site VI, the H atom bonds to a surface oxygen atom, which in turn is at a bridge site between surface Cr atoms. An *sp* type O 2p - H 1s hybridization is formed. The bonding state appears to have about 67% O 2p - 33% H 1s character. The Cr 3d and O 2p states seem to shift towards higher binding energy by about 1 eV. A vacuum environment is an idealistic condition for the highest natural interaction between an H atom and surface oxygen atoms to take place. According to a previous report [20], the presence of dielectric solvents such as H_2O could poison the reactivity of atomic H to the surface oxygen atom by weakening the attractive potential between the two atoms. Upon adsorption at site VII, the H atom bonds to a surface

Cr atom, with an *sd* type Cr 3d - H 1s hybridization. This particular adsorption geometry has also resulted in breaking some of the surface bonds between Cr and O atoms (see Fig. 3 (VII)). The bonding state of the Cr 3d - H 1s hybridization is located below the antibonding state by 6 eV, with about 60% H 1s - 40% Cr 3d character, to be compared with the 90% Cr 3d - 10% H 1s character of the antibonding state.

3.2. Adsorption of Cl atom

The interaction between atomic Cl and the chromium oxide surface is characterized by a significant hybridization between Cl 3s, Cl 3p, Cr 3d, and O 2p orbitals. On surface A, the Cl atom adsorbs at atop site (Fig. 6) to the surface Cr atom (site *i*). The Cr 3d band is slightly broadened as a consequence. The Cl atom gains a charge $-0.39e$ (see Table 3) mainly from the surface Cr $3d_{z^2}$ states. The bonding and antibonding states of the Cl 3p - Cr 3d hybridization are separated by about 5.5 eV (see PDOS plot in Fig. 7*i*). The bonding states of Cl 3s - Cr 3d and Cl 3p - Cr 3d hybridizations are separated by 11 eV, indicating that Cl 3p - Cr 3d hybridization is the dominant character of the interaction between these atoms. The Cl atom appears to interact strongly with this suface, compared with e.g. noble metal surfaces [27].

On surface B, atomic Cl may form a bond to either atom of the Cr=O group. Bonding to the Cr atom (site *ii*) results in Cl being located nearly above the hollow surface Cr atom. Bonding to the O atom (site *iii*) results in Cl being located more towards the hollow surface O atom. The bonding and antibonding states are separated by about 2.8 eV with the adsorption at site *ii*. Electrons are donated from Cr $3d_{xy}$ states to the Cl 3s and $3p_{xy}$ states. With adsorption at site *iii*, the bonding and antibonding states are separated by 5.5 eV. In this case, electrons are donated from O $2p_x$ to Cl $3p_y$ states. The band gap increases slightly upon adsorption at site *iii*, but decreases upon adsorption at site *ii*. Energetically, adsorption at site *ii* is slightly more favorable than adsorption at site *iii*. Such a preference of adsorption of Cl to the metal site rather than to the oxygen site was also implied in a previous investigation in a different system [28].

On the O terminated surface C, Cl adsorbs atop of a surface Cr atom (site *iv*) or atop of a surface O atom (site *v*), with adsorption energies of about 2.5 and 0.7 eV, respectively. Significant relaxation of the surface takes place upon adsorption at site *iv*. The Cr atom of the Cr-1 layer (see Fig. 1c) moves outwards and beyond the surface O-1 layer. Initially sixfold coordinated, the Cr atom becomes fourfold coordinated since three Cr-O bonds are broken and one Cr-Cl bond is formed. The bonding and antibonding states of Cl 3p - Cr 3d hybridization are separated by 3.2 eV while the bonding states of Cl 3s - Cr 3d and Cl 3p - Cr 3d hybridizations are separated by 12.7 eV, indicating the dominance by Cl 3p - Cr 3d interactive overlap. The band gap has decreased while the band width has increased slightly. The charge gained by Cl, $-0.35e$, is mainly donated from the Cr $3d_{z^2}$ to the Cl 3s and Cl $3p_z$ states. Upon adsorption at site *v*, the changes in band gap and band width are not significant. However, in both cases *iv* and *v* our investigation reveals a chemisorptive interaction of Cl with the O terminated surface, as opposed to physisorption processes reported previously [20].

3.3. Adsorption of S atom

Atomic S interacts with the chromium oxide surface both through its 3s and 3p orbitals. The relevant geometries are shown in Fig. 9. On surface A, the favorable adsorption sites are atop of the surface Cr atom (site *a*) or in a bridge site between surface Cr and O atoms (site *b*). With adsorption at site *a*, most of the gained charge of $-0.38e$ (see Table 4) is donated by the surface Cr $3d_{x^2-y^2}$ to the S 3s and S $3p_x$ states. The calculated adsorption energy of 5.04 eV at this site is comparable to the reported values of 3.74 eV [30] and 6.08 eV [31] in different systems. The band width increases slightly. However, the band gap has decreased by 0.3 eV with adsorption at site *a* and increased by 0.2 eV with adsorption at site *b*.

On surface B, the S atom adsorbs atop of the surface O atom (site *c*) or in a bridge site between surface Cr and O atoms (site *d*). The band width increases slightly, and the band gap with adsorption at site *c* has increased by 0.1 eV. The bonding and antibonding states of Cl 3p - Cr 3d hybridization are separated by 5 eV while the bonding states of Cl 3s - Cr 3d and Cl 3p - Cr 3d hybridization are separated by about 7 eV. The adsorption at site *d* resulted in substitutional bonding and bond breaking, i.e., one Cr-O bond per unit cell is broken and substituted by a Cr-S bond. A similar example of metal-oxygen bond substitution by a metal-sulfur bond was observed in a different surface system [29].

On surface C, adsorption of atomic S takes place at a bridge between surface O atoms (site *e*) or atop of a surface O atom (site *f*). The former case results in the formation of an SO_2 complex, a scenario which could have a catalytic effect. The band width increases and the band gap increases by about 0.3 eV (see Fig. 10). Most of the charge donated by the S atom (from the 3s and $3p_z$ states) are gained by the surface oxygen atoms, mainly through O $2p_z$ states (see Fig. 11). One Cr-O

Table 3: Adsorption of Cl. Sites *i* - *v* are illustrated in Fig. 6. Adsorption energies E_{ads} (eV) are based on Eq. (1). $d_{\mathrm{Cl-O}}$ and $d_{\mathrm{Cl-Cr}}$ are Cl-O and Cl-Cr bond lengths, respectively. The geometric, magnetic, and electronic influence on the surface upon adsorption of Cl is expressed in terms of changes in interlayer spacings Δz(Cr-O) and Δz(Cr-Cr) (underlined in Table 1), changes in atomic magnetic moments, $\Delta\mu$, and changes in atomic charges, ΔQ. (Units as in Table 1.) Superscripts: [a] (2×1) surface unit cell; [b] (2×2) surface unit cell; [c] Ref. (20).

Surface	Site	E_{ads}	$d_{\mathrm{Cl-O}}$	$d_{\mathrm{Cl-Cr}}$	Δz(Cr-O)	Δz(Cr-Cr)	Atom	$\Delta\mu$	ΔQ
A	*i*	3.72,3.79[a]	3.25,3.26[a]	2.13,2.14[a]	0.25	−0.02	Cl	0.0	−0.39
							O-1	−0.05	0.04
							Cr-1	1.69	0.39
B	*ii*	1.25	2.73	2.21	−0.46	0.07	Cl	−0.02	−0.31
							O-1	−0.33	0.13
							Cr-1	1.36	0.04
	iii	1.07,1.08[a]	1.71,1.70[a]	2.86,2.84[a]	0.19	0.05	Cl	0.15	−0.01
							O-1	−0.23	0.09
							Cr-1	0.07	−0.07
C	*iv*	2.48,2.53[a],2.56[b]	3.11	2.13	−1.21	1.36	Cl	−0.02	−0.35
							O-1	−0.03	−0.06
							Cr-1	0.31	0.03
	v	0.72	1.70,2.60[c]	3.13	0.05	−0.03	Cl	0.03	0.26
							O-1	−0.03	−0.03
							Cr-1	1.47	−0.07

bond is broken and substituted by a S-O bond, per unit cell. Such a preference by the S atom to bond to non-metals rather than to metals has also been mentioned previously [30].

4. Discussion

The calculated hydrogen-chromium bond distances of about 1.58 Å, presented in Table 2, show covalent type bond between the atoms. These values are in perfect agreement with the hydrogen-chromium bond distances on the Cr(110) surface [24] and are well above the ionic bond distances. The reported bond distances of 1.8 - 1.9 Å on a Pt surface [26] also indicate that the hydrogen-platinum bond is of covalent type. The hydrogen-oxygen and chlorine-oxygen bonds are of covalent nature as expected and are well above the direct sum of the atomic radii. The chlorine-chromium bond distances, shown in Table 3, can be considered as of covalent type on model B while it is largely of ionic nature on models A and C. The sulfur-chromium bonds (Table 4), with bond distances of 1.70 - 1.72 Å, are largely of covalent nature, as are the sulfur-oxygen bonds. However, the relatively shorter sulfur-oxygen bond distances of 1.60 - 1.61 Å are actually the same as the direct sum of the atomic radii. This indicates a possible similarity in the reactive properties between the S and O atoms, and thus explains why substitutional bonds could appear on the surface upon adsorption of S atoms. The calculated sulfur-metal bond distances in different systems [30],[31] also indicate that the sulfur-metal bonds exhibit significant covalent character.

The adsorption studies of the atomic adsorbates on the Cr_2O_3(0001) surface indicate atop sites to be energetically favoured. That is due to the large surface lattice constants ($a = b = 4.95$ Å), which tend to separate identical atoms on the surface. For example, adsorption at a hollow site is reported to be energetically favoured for atomic H on Cr(110) [24] and Pt(111) [26], atomic Cl on Au(111) [27], and atomic S on TiC(001) [30] where the surface interatomic distances are less than or about 2.77 Å. The bridge and hollow site adsorptions on the present surface are typically between the surface Cr and O atoms and typically yield lower adsorption energies because of the location of the atoms on different

Table 4: Adsorption of S. Sites *a* - *f* are illustrated in Fig. 9. Adsorption energies E_{ads} (eV) are based on Eq. (1). d_{S-O} and d_{S-Cr} are S-O and S-Cr bond lengths, respectively. The geometric, magnetic, and electronic influence on the surface upon adsorption of S is expressed in terms of changes in interlayer spacings Δz(Cr-O) and Δz(Cr-Cr) (underlined in Table 1), changes in atomic magnetic moments, $\Delta\mu$, and changes in atomic charges, ΔQ. (Units as in Table 1.) Superscripts: [a] (2×1) surface unit cell.

Surface	Site	E_{ads}	d_{S-O}	d_{S-Cr}	Δz(Cr-O)	Δz(Cr-Cr)	Atom	$\Delta\mu$	ΔQ
A	*a*	5.04	3.13,3.15[a]	2.01,2.02[a]	0.23	−0.01	S	0.0	−0.38
							O-1	−0.04	0.05
							Cr-1	3.50	0.35
	b	3.06	1.75	2.46	0.53	−0.01	S	0.01	−0.07
							O-1	0.01	0.04
							Cr-1	3.56	0.17
B	*c*	2.77,2.77[a]	1.60,1.60[a]	3.10,3.07[a]	0.17	0.04	S	0.74	0.49
							O-1	−0.28	−0.35
							Cr-1	−0.40	−0.08
	d	2.57	1.72	2.16	−0.10	−0.04	S	−0.03	0.34
							O-1	−0.4	0.0
							Cr-1	1.32	−0.12
C	*e*	2.77	1.60	2.79	0.67	−0.04	S	−0.34	1.51
							O-1	−0.13	−0.40
							Cr-1	2.94	−0.25
	f	2.51	1.61	3.18	0.09	−0.09	S	0.62	0.67
							O-1	0.08	−0.32
							Cr-1	1.57	−0.05

planes along the outward axis. This is in agreement with previous studies which noted a reduction in adsorption energies upon adsorption to subsurface atoms [25] or to different types of surface atoms [26].

As shown in Tables 2 through 4, the adsorbates have the effect of reducing or reversing the magnetic moments of the surface Cr-1 or O-1 atoms. This indicates that when the surface atoms gain charge from an adsorbate, the spin state of those electrons largely become spin up, and when the surface atoms lose electrons to an adsorbate, the spin state of those electrons is largely spin down. The adsorbates can gain a higher amount of electrons on surface A than on surfaces B and C. This indicates the degree of favorability of the models for pitting corrosion. Previous studies [15],[17] have shown that surfaces B and C are likely to exist at high temperature and/or pressure. Our investigation (presented in Figs. 3, 6, and 9) shows that significant bond breaking and substitutional bonds can take place on surfaces B and C where the degree to which this happens on surface B is somewhat less than on surface C. This is consistent with the high temperature corrosions which are expected to be accompanied by voids and cracks at a macroscopic level. Moreover, this indicates that the chromyl terminated phase (surface B) should be an intermediate phase in the transition to an oxygen terminated phase (surface C), as expected.

5. Conclusion

Adsorption energies corresponding to the most prefered adsorption geometries are in the range 2.0 - 5.0 eV. This shows that the atomic species can stay intact with the surface over several hundreds of kelvin. These particular adsorptions are also accompanied by significant outward relaxations by the surface atoms, in the range 0.1 - 1.25 Å, bond breakings at the surface, and substitutional bonds as well as bond breakings. The adsorption

of an H atom can cause relaxations of as much as 1.07 Å, while Cl and S atoms cause relaxations of as much as 1.25 and 0.52 Å, respectively. The adsorption of all these atoms on the O terminated surface is observed to result in significant surface bond breakings along with the relaxations. Substitutional bonds are observed to appear upon the adsorption of atomic S, since it can adsorb in bridge sites on all the surface models. The adsorption of H and Cl atoms on Cr and Cr=O terminated surfaces mainly result in outward relaxations.

Atomic Cl binds stronger to Cr than to O on all the surface models. These particular adsorptions are accompanied by charge transfers of the order $-0.35e$ from the surface to the Cl atoms. Atomic H and S bind stronger to O than to Cr on the Cr=O and O terminated surfaces. On the Cr terminated surfaces, the binding is stronger to Cr than to O. With the adsorption of H and S atoms to the Cr terminated surface, charge transfers of about $-0.34e$ and $-0.38e$, respectively, can take place from the surface to the atoms. As a part of a detailed investigation of adsorptive properties on this surface, studies with molecules containing these atomic species are currently under review.

Acknowledgments

We greatly acknowledge NOTUR for providing computer time.

References

[1] H. Cetinel, E. Celik, M. Kusoglu, Journal of Materials Processing Technology 196 (2008) 259.
[2] B. Cho, E. Choi, S. Chung, K. Kim, T. Kang, C. Park, B. Kim, Surf. Sci. 439 (1999) L799.
[3] A. Ashary, R. Tucker, Surface and Coatings Technology 39/40 (1989) 701.
[4] L. Ma, B. Gong, T. Tran, M. Wainwright, Catalysis Today 63 (2000) 499.
[5] E. Ezzo, G. El-Shobaky, M. Selim, Surface Technology 10 (1980) 47.
[6] E. Sourty, J. Sullivan, M. Bijker, Tribology International 36 (2003) 389.
[7] S. Yang, D. Macdonald, Electrochimica Acta 52 (2007) 1871.
[8] S. Nagarajan, N. Rajendran, Corrosion Science 51 (2009) 217.
[9] C. Li, H. Zhao, M. Matsumura, T. Takahashi, M. Asahara, H. Yamaguchi, Surface and Coatings Technology 124 (2000) 53.
[10] J. Robertson, Corrosion Science 32 (1991) 443.
[11] S. Ningshen, U. Mudali, G. Amarendra, R. D. P. Gopalan, H. Khatak, Corrosion Science 48 (2006) 1106.
[12] T. Pan, F. Gesmundo, Y. Niu, Corrosion Science 49 (2007) 1362.
[13] E. McCafferty, Corrosion Science 29 (1989) 391.
[14] K. Kumar, M. Sujata, M. Venkataswamy, S. Bhaumik, Engineering Failure Analysis 15 (2008) 497.
[15] X.-G. Wang, J. Smith, Phys. Rev. B 68 (2003) 201402.
[16] A. Rohrbach, J. Hafner, G. Kresse, Phys. Rev. B 70 (2004) 125426.
[17] B. Dillmann, F. Rohr, O. Seiferth, G. Klivenyi, M. Bender, K. Homann, I. Yakovkin, D. Ehrlich, M. Bäumer, D. Ehrlich, H. Kuhlenbeck, H.-J. Freund, Faraday Disc. 105 (1996) 295.
[18] M. Pykavy, V. Staemmler, O. Seiferth, H.-J. Freund, Surf. Sci. 479 (2001) 11.
[19] C. Rehbein, N. Harrison, A. Wander, Phys. Rev. B 54 (1996) 14066.
[20] S. Petrosyan, A. Rigos, T. Arias, J. Phys. Chem. B 109 (2005) 15436.
[21] Q. Guo, L. Gui, P. Moller, K. Binau, Appl. Surf. Sci. 92 (1996) 513.
[22] C. Xu, B. Dillmann, H. Kuhlenbeck, H.-J. Freund, Phys. Rev. Lett. 67 (1991) 3551.
[23] B. Tepper, B. Richter, A.-C. Dupuis, H. Kuhlenbeck, C. Hucho, P. Schilbe, M. bin Yarmo, H.-J. Freund, Surf. Sci. 496 (2002) 64.
[24] T. Komeda, Y. Sakisaka, M. Onchi, H. Kato, S. Suzuki, K. Edamoto, Y. Aiura, Phys. Rev. B 38 (1988) 7349.
[25] U. Bischler, P. Sandl, E. Bertel, T. Brunner, W. Brenig, Phys. Rev. Lett. 70 (1993) 3603.
[26] C. Pistonesi, E. Pronsato, A. Juan, Appl. Surf. Sci. 254 (2008) 5827.
[27] T. Baker, C. Friend, E. Kaxiras, J. Chem. Phys. 129 (2008) 104702.
[28] M. Menetrey, A. Markovits, C. Minot, Surf. Sci. 566-568 (2004) 693.
[29] J. Rodriguez, J. Hrbek, Z. Chang, J. Dvorak, T. Jirsak, A. Maiti, Phys. Rev. B 65 (2002) 235414.
[30] J. Rodriguez, P. Liu, J. Dvorak, T. Jirsak, J. Gomes, Y. Takahashi, K. Nakamura, Phys. Rev. B 69 (2004) 115414.
[31] M. Chen, P. Clark, Jr., T. Mueller, C. Friend, E. Kaxiras, Phys. Rev. B 60 (1999) 11783.
[32] S. Krasnikov, G. Hughes, A. Cafolla, Surf. Sci. 601 (2007) 3506.
[33] D. Vanderbilt, Phys. Rev. B 41 (1990) 7892.
[34] H. Monkhorst, J. Pack, Phys. Rev. B 13 (1976) 5188.
[35] J. Perdew, J. Chevary, S. Vosko, K. Jackson, M. Pederson, D. Singh, C. Fiolhais, Phys. Rev. B 46 (1992) 6671.
[36] W. Press, B. Flannery, S. Teukolsky, W. Vetterling, Numerical Recipes in Fortran 2. ed, Cambridge University Press, Cambridge, 1992.
[37] L. Bengtsson, Phys. Rev. B 59 (1999) 12301.
[38] J. Neugebauer, M. Scheffler, Phys. Rev. B 46 (1992) 16067.
[39] R. Bader, Atoms in Molecules. A Quantum Theory, Oxford, Clarendon, 1990.
[40] V. Maurice, S. Cadot, P. Marcus, Surf. Sci. 458 (2000) 195.
[41] R. Wyckoff, Crystal Structures 2. ed, Interscience, NewYork, 1964.
[42] L. Pauling, S. Hendricks, J. Am. Chem. Soc. 47 (1925) 781.
[43] D. Woodruff, The Chemical Physics Of Solid Surfaces, Elsevier, Amsterdam, The Netherlands, 2001.
[44] Ø. Borck, E. Schröder, J. Phys.: Condens. Matter 18 (2006) 10751.
[45] W. Moritz, R. Imbihl, R. Behm, G. Ertl, T. Matsushima, J. Chem. Phys. 83 (1985) 1959.

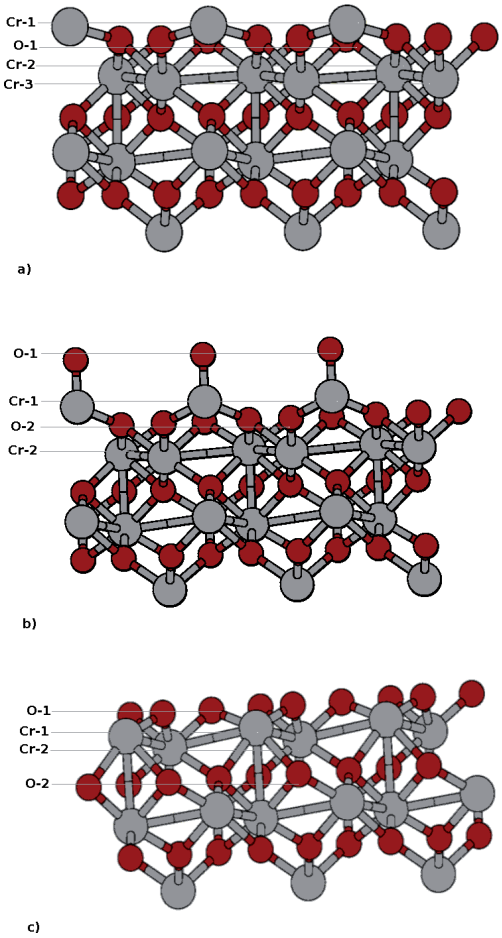

Figure 1: Side view of the three $Cr_2O_3(0001)$ surface models; a) terminated by Cr atoms (surface A); b) terminated by Cr=O groups (surface B); and c) terminated by O atoms (surface C). Colors: O - red, Cr - grey. O-*m* and Cr-*m* denote the *m*-th layer of O and Cr atoms, respectively.

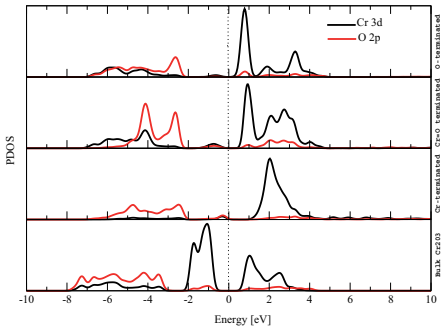

Figure 2: Projected density of states (PDOS, arbitrary units) of Cr 3d (black line) and O 2p (red line) states for bulk Cr_2O_3 (bottom panel) and Cr (surface A, second panel), Cr=O (surface B, third panel), and O (surface C, top panel) terminated $Cr_2O_3(0001)$ surface slab models. The present figure should be seen in conjunction with Fig. 1, where geometries of the surface slab models are shown.

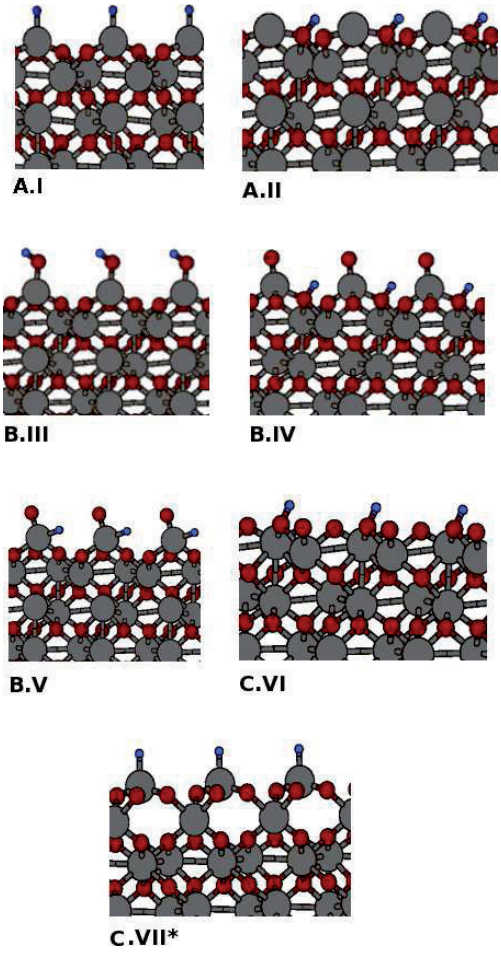

Figure 3: Geometries after adsorption of H atom. A, B, and C denote the surfaces A, B, and C, respectively. The uppercase roman numbers denote adsorption geometries of the sites described in Table 2. The present figure should be seen in conjunction with Figs. 1, 4, and 5. The asterisk (*) implies that bond breaking has taken place in that adsorption geometry. Colors: O - red, Cr - grey, H - blue.

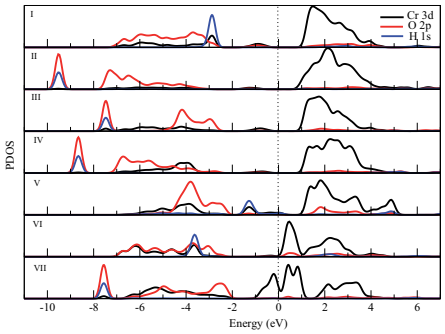

Figure 4: Projected density of states (PDOS, arbitrary units) after adsorption of an H atom on the three surfaces. The present figure should be seen in conjunction with Figs. 3 and 5.

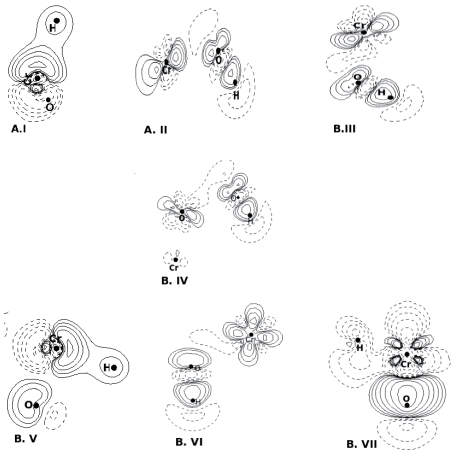

Figure 5: Contour plots of electron differences calculated by Eqn. (4) after adsorption of H atom. A, B, and C denote surfaces A, B, and C, respectively. The solid (broken) lines imply a gain (loss) of electrons, respectively. The plots should be seen in conjunction with Figs. 3 and 4.

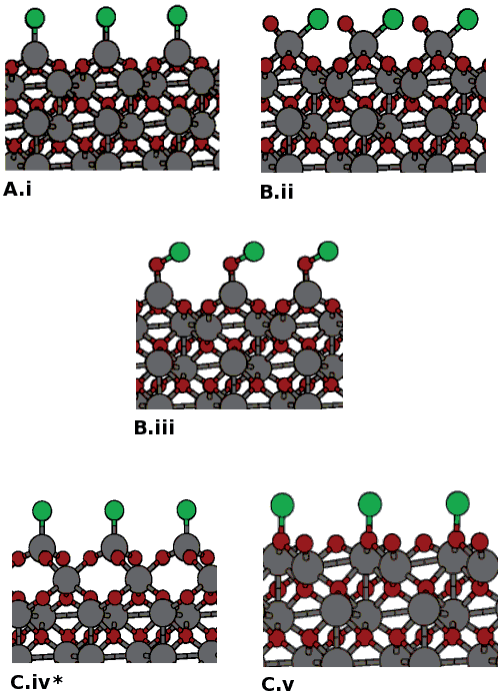

Figure 6: Geometries after adsorption of Cl atom. A, B, and C denote the surfaces A, B, and C, respectively. The lowercase roman numbers denote adsorption geometries of the sites described in Table 3. The present figure should be seen in conjunction with Figs. 1, 7, and 8. The asterisk (*) implies that bond breaking has taken place in that adsorption geometry. Colors: O - red, Cr - grey, Cl - green.

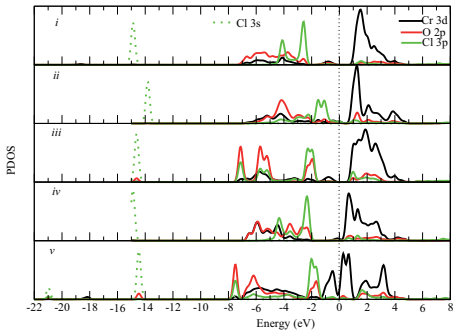

Figure 7: Projected density of states (PDOS, arbitrary units) after adsorption of a Cl atom on the three surfaces. The present figure should be seen in conjunction with Figs. 6 and 8.

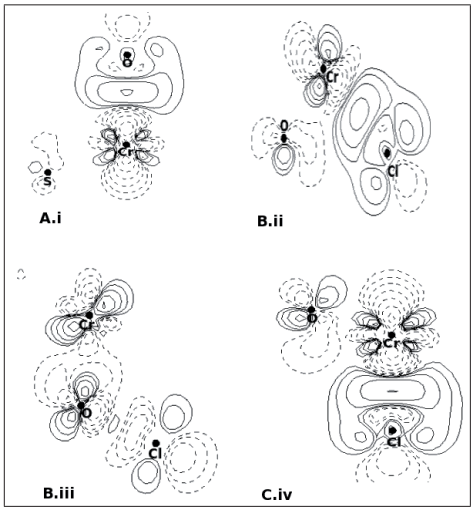

Figure 8: Contour plots of electron differences calculated by Eqn. (4) after adsorption of Cl atom. A, B, and C denote surfaces A, B, and C, respectively. The solid (broken) lines imply a gain (loss) of electrons, respectively. Plots are presented only for selected adsorption sites, indicated by roman numbers, and should be seen in conjunction with Figs. 6 and 7.

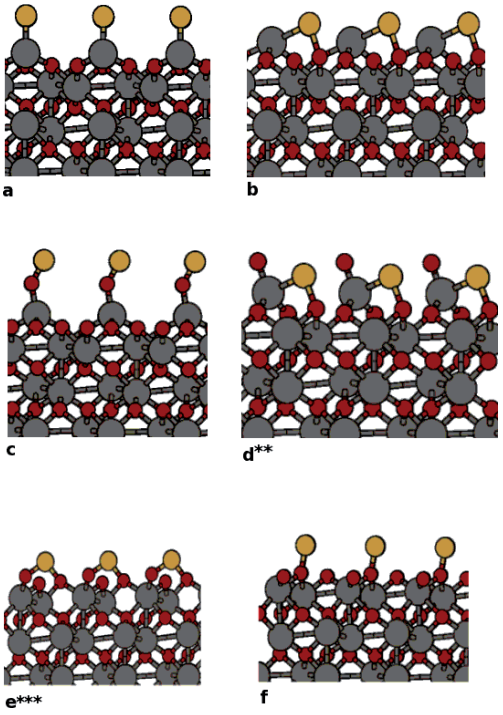

Figure 9: Geometries after adsorption of S atom. A, B, and C denote the surfaces A, B, and C, respectively. The lowercase letters denote adsorption geometries of the sites described in Table 4. The present figure should be seen in conjunction with Figs. 1, 10, and 11. Two asterisks (**) imply that substitutional bonding plus bond breaking has taken place in that adsorption geometry. Three asterisks (***) imply that substitutional bonding has taken place. Colors: O - red, Cr - grey, S - yellow.

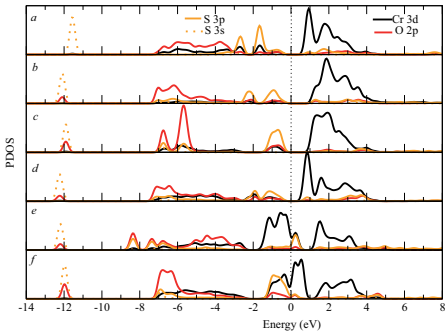

Figure 10: Projected density of states (PDOS, arbitrary units) after adsorption of an S atom on the three surfaces. The present figure should be seen in conjunction with Figs. 9 and 11.

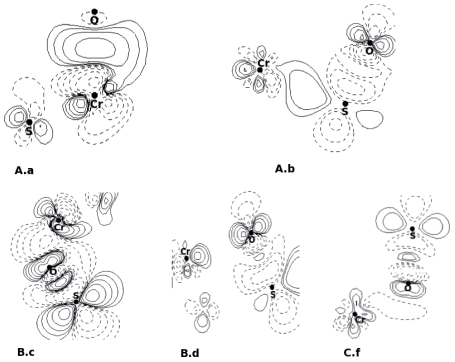

Figure 11: Contour plots of electron differences calculated by Eqn. (4) after adsorption of S atom. A, B, and C denote surfaces A, B, and C, respectively. The solid (broken) lines imply a gain (loss) of electrons, respectively. Plots are presented only for selected adsorption sites, indicated by lowercase letters, and should be seen in conjunction with Figs. 9 and 10.

PAPER II

Adsorption of H_2, Cl_2, and HCl molecules on α-Cr_2O_3(0001) surfaces: A Density Functional Theory investigation

Submitted to Journal of Chemical Physics

Adsorption of H_2, Cl_2, and HCl molecules on α-Cr_2O_3 (0001) surfaces: A Density Functional Theory investigation

K. N. Nigussa, Ø. Borck, and J. A. Støvneng*

Department of Physics, NTNU, N-7491 Trondheim, Norway

K. L. Nielsen

Sør-Trøndelag University College (HiST), N-7004 Trondheim, Norway

(Dated: February 5, 2011)

Abstract

Density functional theory calculations show that H_2, Cl_2, and HCl chemisorb dissociatively on the Cr_2O_3 (0001) surface, which can be terminated by chromyl groups (Cr=O), Cr atoms, or O atoms. Several dissociative adsorption sites have been considered for all the molecules on all the differently terminated surfaces. Dissociation energy barriers and adsorption energies are estimated with the nudged elastic band method. Notable results from the dissociative adsorptions of Cl_2 and H_2 are the formation of a $CrCl_2$ complex on the Cr terminated surface, an H_2O complex on the O and the Cr=O terminated surfaces, and an H_2O layer on the Cr=O terminated surface. Dissociative adsorption of HCl is less favored on the Cr=O and O terminated surfaces than on the Cr terminated surface.

*Correspondence to:jon.stovneng@ntnu.no

1. Introduction

The interaction of H_2, Cl_2, and HCl molecules with different surfaces has been studied for different technological purposes [1],[2]. We have previously found that the adsorption of atomic H, Cl, and S enhances the corrosion prospects of the Cr_2O_3 (0001) surface [3]. These properties are expected to be manifested by the dissociative adsorption of these molecules at adsorbate coverages lower than about 0.25 ML. At higher adsorbate coverages (typically 1.0 ML), an emphasis on the different chemical complexes formed at the surface will be of interest. Such a characterization would be elaborated by investigating conditions under which dissociative adsorption of these molecules happen on the Cr_2O_3 (0001) surface. Adsorption of H_2 has been the focus in studies of hydrogen storage materials [1], semiconductor technology [4], catalysis [5],[6], and various other applications.[7],[8] It was concluded that metal-hydride (MH) or hydroxyl (OH) complexes are formed, depending on the type of substrate surface. Adsorption of larger molecules containing H atoms has been studied experimentally and theoretically on the Cr_2O_3 (0001) surface[9],[10], and it was shown that the molecules can adsorb dissociatively, resulting in O-H formation above the surface. Here, O is the surface oxygen atom and H is the hydrogen atom obtained from the dissociation of the molecules. However, as far as we are aware, the adsorption of H_2 on α-Cr_2O_3 (0001) surface has not been reported.

In a previous work[3], we have argued that the Cr_2O_3 (0001) surface can terminate by Cr=O groups or by Cr or O atoms, depending on the conditions. For example, as one specific condition, plasma spraying on a Cr_2O_3 (0001) surface[9] is found to result in the formation of various surface phases such as CrO_2 (which is similar to what we call O terminated) and CrO on the original Cr terminated surface (before spraying). Hence, we have considered adsorption of H_2 on Cr_2O_3 (0001) surfaces with these possible terminations. Our routine method of investigation is similar to the work by Liao et al.[8]. They studied adsorption of H_2 on the (100), (010), and (001) faces of the Fe_3C alloy which expose C atoms (non-metal) or Fe atoms (metal) to the adsorbates. Another example is the MgO(001) surface, which is more ionic than the Cr_2O_3 (0001) surface. However, it exposes O atoms to the adsorbates, similar to Cr=O or O terminated Cr_2O_3 (0001). The extensive dissociation and diffusion barrier height calculations performed by Wu et al.[7] on the MgO(001) surface have become an inspiration for us. Our investigation shows a markedly different dynamics and a more

chemisorptive interaction of the molecule to the Cr=O and O terminated Cr_2O_3 (0001) surfaces, along with lower values of the barrier energies. This has to do with differences in the chemical nature of the surface atoms.

In addition to the hydroxyl complexes formed at the surface, which have a catalytic effect [11], we also find that H_2O complexes and layers may be formed upon adsorption of H_2 on the O and Cr=O terminated surfaces. Adsorption of H_2O on metal terminated corundum surfaces such as Cr_2O_3 (0001) [9]-[12], Fe_2O_3 (0001) [13],[14], V_2O_3 (0001) [15], and Al_2O_3 (0001) [16] is observed to result in similar configurations, where buckled hexagonal rings or a two-dimensional hexagonal lattice of H_2O are formed above the surface, depending on the adsorbate coverage.

Adsorption of Cl_2 has been investigated on the MgO(001) surface [17],[18], the TiO_2(110) surface [19], and on semiconductor surfaces.[20],[21] However, studies of adsorption of this molecule on corundum transion metal oxides is lacking. In this paper, we report the adsorptive interaction of Cl_2 on the Cr=O, O, and Cr terminated Cr_2O_3 (0001) surface. It has been shown that Cl_2 adsorbs dissociatively on TiO_2(110) [19], whereas the unsupported and defect free MgO(001) surface [17],[18] was found to be inert to Cl_2. This difference may be due to the high concentration of anions at the surface of MgO(001), since it terminates by oxygen ions, and the relatively equally exposed Ti and O atoms on the TiO_2(110) surface. Further, Cl_2 is observed to adsorb dissociatively at the metal support sites [17],[18] without noticeable barrier energies, forming $AgCl_2$ and $NaCl_2$ complexes, respectively. On the Ge(001)-c(2×4) surface [21] and the Si(001)-2×1 surface [22], Cl_2 is observed to dissociate instantly. At low adsorbate coverage, GeCl and SiCl complexes were observed to be formed, and at higher coverages it was predicted that $GeCl_2$ and $SiCl_2$ would be formed. On the GaAs(110) surface [22], the molecule adsorbs dissociatively and forms GaCl and AsCl at low coverage, and $GaCl_2$ and $AsCl_2$ at high coverage. Hence, the results in these papers [17],[18]-[22] indicate that Cl_2 is strongly reactive to metal terminated systems, and inert to anion terminated surfaces. In this paper, we consider the different possible terminations of the Cr_2O_3 (0001) surface which in turn exposes anions or cations based on the type of termination. To investigate mono chloride and dichloride formation, we systematically vary the adsorbate coverage. Chromium dichloride, $CrCl_2$, finds several applications, for example in condensation of aldehydes.[23]

Experimentally, it has been found that Cr_2O_3 is a good candidate for reducing HCl

elimination in plastic engineering, where HCl is produced as a biproduct.[24] This shows that HCl is indeed reactive to Cr_2O_3. In this paper, we make a theoretical investigation of the reactivity of HCl with the Cr_2O_3 (0001) surface. Our analysis is similar with theoretical investigations of adsorption of HCl on α-Al_2O_3 (0001) [2] and Ge(001)-c(2×4).[21]

In summary, this study is devoted to calculating various reaction paths of dissociative adsorption of H_2, Cl_2, and HCl, leading to the formation of various complexes at the Cr_2O_3 (0001) surface. Adsorption coverages of 0.5 and 1.0 ML are chosen, and the corresponding detailed reaction patterns of these molecules to the differently terminated surfaces are provided. Diffusion of H and Cl between surface and subsurface sites is also briefly addressed. The paper is organized as follows. In section 2, a brief account of the computational methods is presented, followed by the results in section 3 and a discussion in section 4. We close the paper with some conclusions in section 5.

2. Computational method

The Dacapo program [25] based on ultrasoft pseudopotentials [26] is used for the DFT calculations. The electronic wavefunctions are obtained with the Kohn-Sham approximation and expanded in a plane wave basis set with the cutoff energy set to 400 eV. For the treatment of the electron exchange and correlation energies, we use the generalized gradient approximation (GGA) of PW91.[27] The k-point meshes are chosen based on the Monkhorst-Pack scheme [28] and values of 4×4×1 and 2×4×1, respectively, are used for the calculations on the (1×1) and (2×1) surface unit cells. The surface is modeled with a four layer slab with terminations by Cr=O groups, or O or Cr atoms in the top layer.[3] The ions in the top three layers are allowed to relax based on the BFGS geometry optimization scheme until the total force on each atom falls below 0.05 eV/Å. Adsorptions are investigated by putting the molecule on one side of the slab, and the corresponding adsorption energies are calculated by

$$E_{ads} = -(E_{SM} - E_S - E_M). \quad (1)$$

Here, E_S is the total energy of the clean surface, E_M is the total energy of the isolated molecule, and E_{SM} is the total energy of the relaxed geometry containing both substrate and molecule. All energies are per supercell.

Adsorbate coverage is expressed in terms of surface Cr atoms: 1.0 ML means one adsorbed

molecule per surface Cr atom, and 0.5 ML means one adsorbed molecule per two surface Cr atoms. The reaction paths are calculated based on the nudged elastic band method [29],[30], and the minimum energy paths are searched for using a quasi-Newton iterative scheme by mapping out images between two preset geometries. The barrier heights are determined by substracting the energy of the initial state (IS) from the energy of the transition state (TS). The initial state corresponds to molecular adsorption on the given surface, physisorption when the binding energy of IS is very low and chemisorption for higher values of the binding energy of IS. For the calculation of diffusion barrier heights, the initial and final states are both equilibrium adsorption geometries where the adsorbate molecules have dissociated into atomic species. For the reaction paths presented in Figs. 1 - 5, we have checked that increasing the number of images in the NEB calculations has only a small effect on barrier heights and transition state geometries. In Figs. 1 - 5, the energy is given relative to separate reactants, i.e., molecule and clean surface.

3. Results

3.1 Adsorption of H_2

The DFT calculations yield a bond length in the free H_2 molecule of 0.75 Å, which is in excellent agreement with literature values.[31] In Table I and Figs. 1 and 2, we present geometries and adsorption and activation energies resulting from the various NEB calculations.

On the Cr=O terminated surface, the dissociated H atoms adsorb in two stable geometries. The two dissociation reactions have equal energy barriers, 1.55 eV, see Table I and Figs. 1(a) and 1(b). The corresponding adsorption energies are 1.16 and 1.05 eV. In the first reaction (Fig. 1(a)), the surface becomes basic as a result of the formation of two OH groups. In the second reaction (Fig. 1(b)), an H_2O layer is formed above the surface, with a distance of 2.40 Å between the surface Cr atom and the O atom of the H_2O adduct. The latter reaction proceeds via a basic transition state (TS) to a neutral final state upon expulsion of the H_2O segment from the surface. Moreover, by losing its O atom, the surface becomes effectively Cr terminated, covered by a layer of H_2O. A reorientation of the H_2O molecule, presumably with a low energy barrier (not calculated), results in a more stable geometry,

TABLE I: Adsorption of 1 ML H_2 on (1×1) surfaces. Surface denotes surface termination type, E_{ads}^{mol} and E_{ads}^{diss} denote molecular (IS) and dissociative (FS) adsorption energies, respectively, and E_a (eV) denotes activation energy. d_1 and d_2 (Å) are the two shortest O-H distances. IS, TS, and FS denote initial, transition, and final state, respectively.

				IS		TS		FS	
Surface/Figure	E_{ads}^{mol}	E_{ads}^{diss}	E_a	d_1	d_2	d_1	d_2	d_1	d_2
Cr=O/1a	0.66	1.16	1.55	2.42	3.17	0.98	2.65	0.98	0.99
Cr=O/1b	0.64	1.05	1.55	2.81	2.85	1.00	2.47	1.00	0.98
O/2a	0.66	2.20	1.27	2.84	2.75	1.49	1.54	0.98	0.99
O/2b	0.66	1.81	1.61	2.71	2.84	0.98	2.70	0.98	1.01
Cr	0.67	−0.34	1.76	3.68	4.08	1.69	2.38	0.98	0.98

an H_2O "complex", with a bond distance between the O atom of the H_2O complex and the Cr atom of the surface of 2.14 Å. The adsorption energy of this complex is 1.41 eV. It is well stabilized by a hydrogen bond between one of the H atoms and one of the subsurface O atoms.

Alternatively, we may view the final states of Figs. 1(a) and 1(b) as the results of dissociative and molecular adsorption, respectively, of H_2O on the Cr terminated surface. The dissociative adsorption of H_2O then has $E_{ads} = 0.56$ eV whereas the molecular adsorption has $E_{ads} = 0.44$ eV. Furthermore, the initial state of Fig. 1(b) may be viewed as a possible final state of dissociative adsorption of H_2O on the Cr terminated surface. This reaction is exothermic by 0.06 eV and has an energy barrier of 1.95 eV, assuming the reaction in Fig. 1(b) is reversible. It would result in an H_2 covered Cr=O terminated surface, and could be relevant for hydrogen production and storage. Chemical oxidation of metals with H_2O resulting in the liberation of H_2 has already been suggested as a method for storing hydrogen in materials.[1]

On the O terminated surface, the two adsorption pathways have significantly different barrier and adsorption energies, as presented in Table I and Figs. 2(a) and 2(b). The most favored adsorption geometry results in the formation of OH groups, with the dissociated H atoms far apart, see Fig. 2(a). Upon the formation of OH groups, the surface becomes basic,

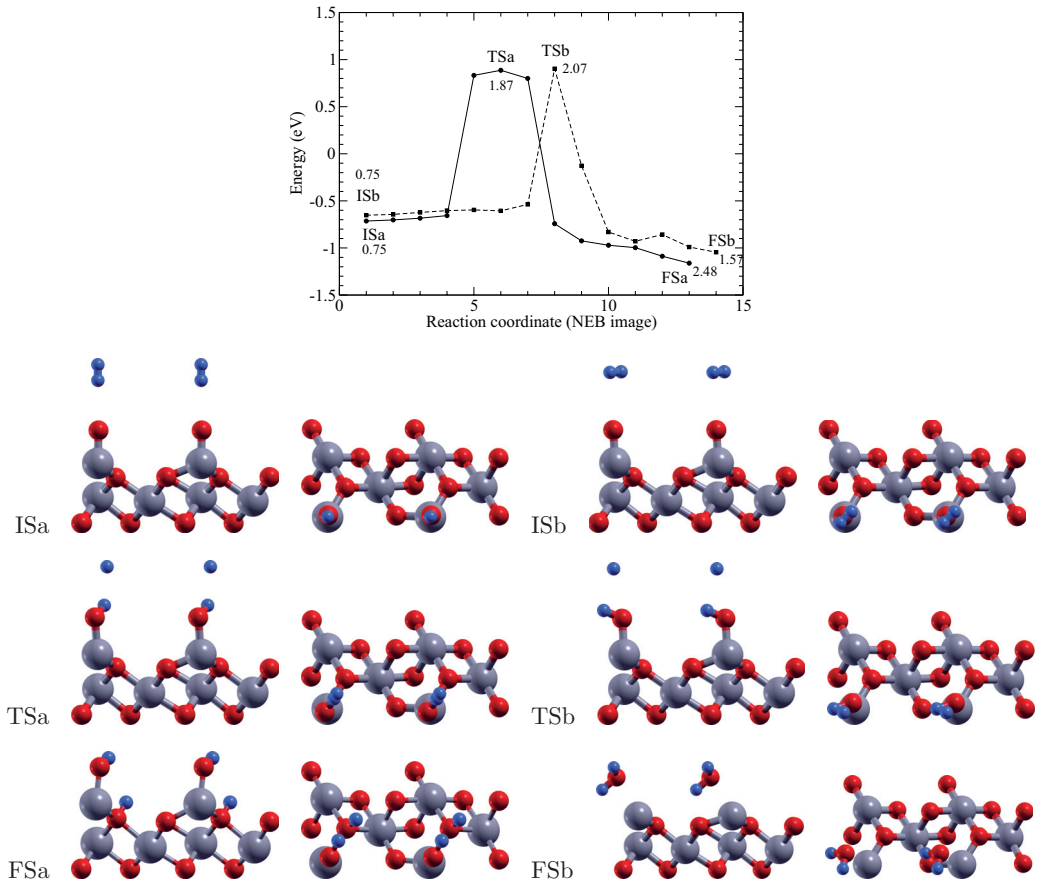

FIG. 1: (Color online) Reaction paths for adsorption of H_2 on the Cr=O terminated surface. a) Dissociation leading to OH complex formation. b) Dissociation leading to H_2O layer formation. The numbers above the curves denote the H-H distance. The top layers ($O_3Cr_2O_3Cr{=}O$) plus the adsorbate of two unit cells are shown, side view (left) and top view (right), in the initial (IS), transition (TS), and final (FS) states. Colors (size, grayscale): Cr-gray (large, medium gray), O-red (medium, dark gray), H-blue (small, medium gray).

and this makes it very reactive towards acidic materials. The second most stable adsorption geometry results in the formation of an H_2O complex, see Fig. 2(b). The adsorption energies of the structures in Figs. 2(a) and 2(b) are 2.20 and 1.81 eV, respectively.

At 1.0 ML coverage, the dissociative adsorption of H_2 on the Cr terminated surface is unfavorable (endothermic). All our calculations suggest that molecular physisorption

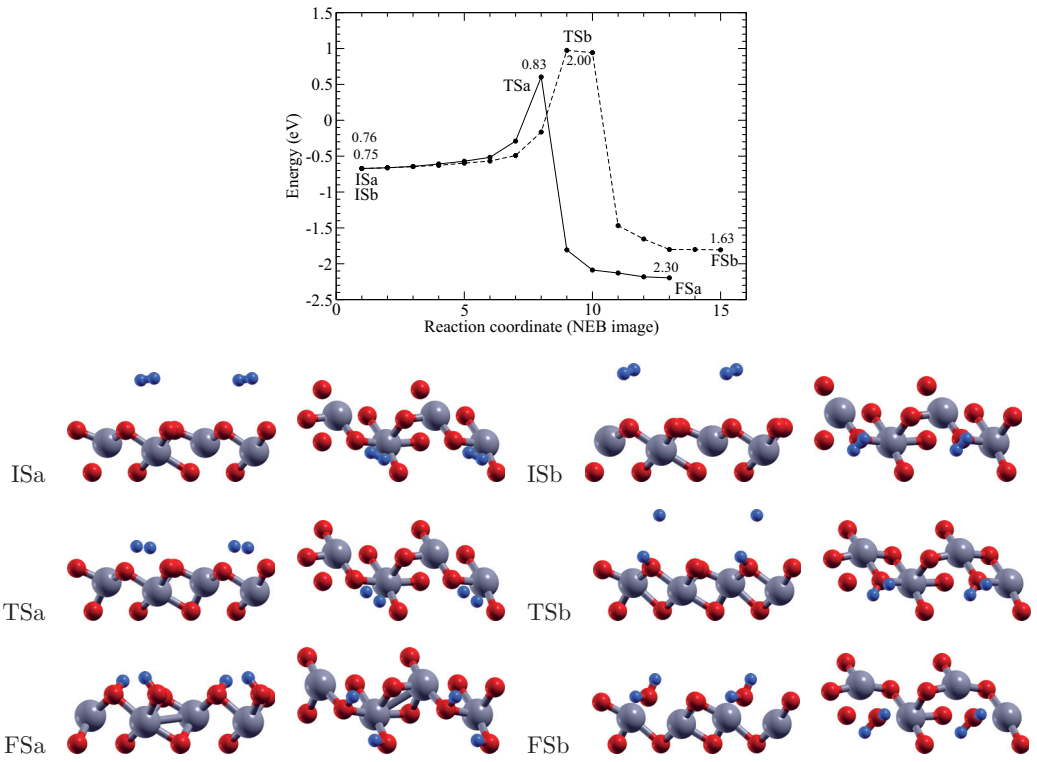

FIG. 2: Reaction paths for adsorption of H_2 on the O terminated surface. a) Dissociation leading to OH complex formation. b) Dissociation leading to H_2O complex formation. The numbers above the curves denote the H-H distance. The top layers ($O_3Cr_2O_3$) plus the adsorbate of two unit cells are shown, side view (left) and top view (right), in the initial (IS), transition (TS), and final (FS) states. Colors (size, grayscale): Cr-gray (large, medium gray), O-red (medium, dark gray), H-blue (small, medium gray).

represents the only stable adsorptive geometry. Molecular physisorption may be of relevance for hydrogen storage applications [1]. The minimum energy barrier for the dissociative adsorption, where the H atoms adsorb to separate O atoms of the surface forming OH groups, is 1.76 eV. In this adsorption geometry, the O atoms are pulled above the Cr atoms in the top surface layer. The large extent of surface reconstruction is consistent with the endothermic nature of this particular adsorption.

Reduction of the adsorbate coverage, from 1.0 to 0.5 ML, will typically result in sig-

nificantly higher adsorption energies and lower energy barriers. For adsorption of H_2 on the Cr=O terminated surface, E_{ads} increases from 1.16 to 2.20 eV for the formation of OH groups. Both hydrogen atoms are bonded to the oxygen of the Cr=O groups in the final geometry, and as expected, this is highly prefered to the geometry in Fig. 1(a), where one H atom is bonded to a subsurface oxygen. On the other hand, for the formation of an H_2O complex, the adsorption energy stays approximately the same upon decreasing the coverage from 1.0 ML to 0.5 ML. The 1 ML H_2O complex discussed above, with adsorption energy 1.41 eV, is not expected to become more stabilized by reducing the coverage. On the O terminated surface, the formation of OH groups is prefered over H_2O complex formation also at 0.5 ML adsorbate coverage. Dissociative adsorption resulting in adsorption of the two H atoms to separate O atoms (i.e., formation of two OH groups), is exothermic, by 2.02 eV. In contrast to the dissociative adsorption of H_2 on the Cr terminated surface at 1.0 ML adsorbate coverage, we find that, at an adsorbate coverage of 0.5 ML, the H atoms adsorb to separate Cr atoms, resulting in a stable adsorption geometry (exothermic by 0.74 eV) and the formation of metal hydride CrH complexes.

3.3 Adsorption of Cl_2

We have calculated the bond length of Cl_2 to be 2.00 Å which is in good agreement with the experimental value of 1.99 Å.[31] In Table II and Figs. 3 and 4, we present geometries and adsorption and activation energies resulting from the various NEB calculations.

At a coverage of 1 ML, we have found one unstable dissociative adsorption geometry of Cl_2 on the Cr=O terminated surface (endothermic by 0.56 eV), stable dissociative adsorption geometries on the Cr terminated surface (exothermic by 1.8 - 2.0 eV), and one stable physisorption (undissociative) geometry on the O terminated surface (exothermic by 0.14 eV). Dissociative adsorption of Cl_2 on the O terminated surface is endothermic.

On the Cr=O terminated surface, the dissociative adsorption faces a significant energy barrier of 1.45 eV, cf Table II and Fig. 3, and results in an endothermic process. The two Cl atoms are far apart, and one adsorbs to the O atom while the other adsorbs to the Cr atom.

On the Cr terminated surface, Cl_2 adsorbs dissociatively and readily forms a $CrCl_2$ complex with no energy barrier, Fig. 4 (IS). A similar high reactivity of the Cl_2 molecule on

TABLE II: Adsorption of 1 ML Cl_2 on (1×1) surfaces. Surface denotes surface termination type, E_{ads}^{mol} and E_{ads}^{diss} denote molecular (IS) and dissociative (FS) adsorption energies, respectively, and E_a (eV) denotes activation energy. d_1 and d_2 (Å) are the two shortest Cr-Cl distances. IS, TS, and FS denote initial, transition, and final state, respectively.

				IS		TS		FS	
Surface/Figure	E_{ads}^{mol}	E_{ads}^{diss}	E_a	d_1	d_2	d_1	d_2	d_1	d_2
Cr=O/3	0.45	−0.56	1.45	2.49	4.50	2.20	3.21	2.18	3.18
O	0.14								
Cr/4 IS	-	1.83	0.00	-	-	-	-	2.29	2.45

Ag supported MgO(001)[17] and Na supported MgO(001)[32] has been reported. On these surfaces, Cl_2 was reported to adsorb dissociatively and form $AgCl_2$ and $NaCl_2$ complexes without a noticeable energy barrier. On the other hand, the adsorption of Cl_2 has been reported to be passive on the unsupported MgO(001) surface [33]. These observations are in agreement with our results, since we may compare the Cr terminated surface with the metal supported MgO(001) surfaces, and the Cr=O and O terminated surfaces with the unsupported MgO(001) surface.

The structure obtained after geometry relaxation represents a local energy minimum, where the Cl atoms are aligned along the $(1\ \sqrt{3}\ 0)$ direction, see Fig. 4 (IS). A rotation of Cl_2 approximately 30 degrees around the z axis brings the structure to the (presumably) global energy minimum, which represents a nearly perfect honeycomb lattice of Cl atoms adsorbed on the Cr terminated surface, see Fig. 4 (FS). This structure is the result of appropriate Cr-Cl bond lengths of 2.21 Å and a Cl-Cr-Cl bond angle of 81 degrees in the $CrCl_2$ fragment, that match the lattice constant of 4.955 Å of the hexagonal unit cell. The energy barrier for this rotation reaction is small, only 0.14 eV. The reverse rotation, from FS to IS, has an energy barrier of 0.29 eV. The binding energies of IS and FS are 2.83 and 2.98 eV, respectively.

With a larger (2×1) surface unit cell (supercell), corresponding to 0.5 ML Cl_2 coverage, the adsorption energy increases, from 1.83 eV (or 1.98 eV) to 2.44 eV, for formation of the $CrCl_2$ group, i.e., with both Cl atoms adsorbing to the same Cr atom. As expected,

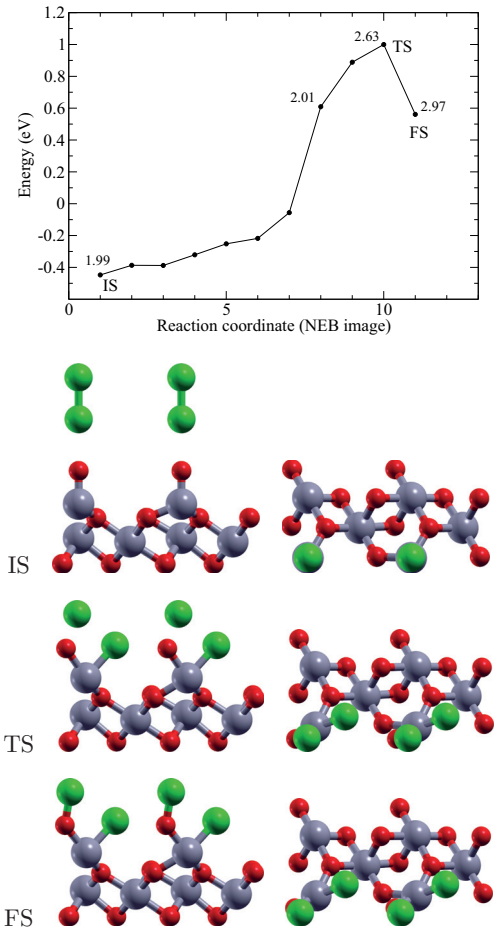

FIG. 3: (Color online) Reaction path for Cl_2. Dissociation on the Cr=O terminated surface, final state with one Cl bonded to O and one Cl bonded to Cr. The numbers above the curve denote the Cl-Cl distance. The top layers ($O_3Cr_2O_3Cr{=}O$) plus the adsorbate of two unit cells are shown, side view (left) and top view (right), in the initial (IS), transition (TS), and final (FS) states. Colors (size, grayscale): Cr-gray (large, medium gray), O-red (medium, dark gray), Cl-green (large, light gray).

the adsorption energy increases even further, to 4.43 eV, when the two Cl atoms adsorb to separate Cr atoms. The latter case corresponds to adsorption of 1 ML atomic Cl on the (1×1) Cr terminated surface [3].

On the (2×1) O terminated surface, dissociative adsorption of 0.5 ML Cl_2 has a sub-

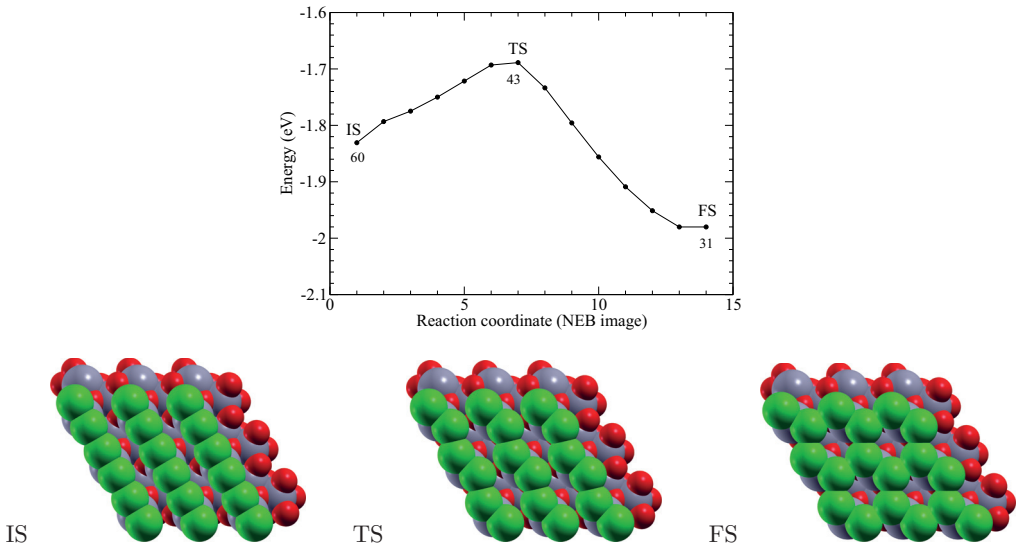

FIG. 4: Reorientation of Cl_2 on the (1×1) Cr terminated surface. In the final state (FS), the Cr-Cl bond lengths and the Cl-Cr-Cl bond angle of the $CrCl_2$ fragment, as well as the orientation of the $CrCl_2$ group with respect to the surface, have values such that a nearly perfect honeycomb lattice of Cl atoms is formed. The three nearest neighbour Cl-Cl distances are 2.81, 2.88, and 2.90 Å. An average of these values multiplied with $2\cos 30°$ yields an average next-nearest neighbour Cl-Cl distance 4.96 Å, very close to the lattice constant 4.955 Å. The numbers below the energy curve represent the angle between the Cl - Cl "bond" and the horizontal axis. A space filling model has been used to emphasize the geometry of the adsorbed chlorine layer. Colors (size, grayscale): Cr-gray (large, medium gray), O-red (medium, dark gray), Cl-green (large, light gray).

stantial activation energy of 2.27 eV and an adsorption energy of 1.74 eV. In the final state, the two Cl atoms are bonded to separate Cr atoms. Significant surface reconstruction has taken place, since the Cr atoms move from an initial position below the surface O atoms to a final position above the O atoms. This is similar to adsorption of 1 ML atomic Cl on the (1×1) O terminated surface [3].

3.4 Adsorption of HCl

The DFT calculations show that the bond length in HCl in the free molecule is 1.25 Å, which is in excellent agreement with literature values.[31] In Table III and Fig. 5, we present geometries and adsorption and activation energies resulting from the various NEB calculations.

We have found two stable adsorption geometries for the dissociative adsorption of HCl on the Cr terminated surface, with adsorption energies of 1.22 and 0.93 eV, and energy barriers of 0.19 and 0.99 eV, respectively. In both adsorption geometries, H is adsorbed to an O atom and Cl is adsorbed to the surface Cr atom. The difference between the two is that H is adsorbed to *different* O atoms. In the most stable geometry, H is bonded to a "next nearest neighbor" O atom, which allows for a stabilizing attraction between H and Cl. This is accompanied by an elongated O-H bond of 1.01 Å (d_1 in FS in Fig. 5(b), see Table III). The geometry is illustrated in Fig. 5(b). At 0.5 ML adsorbate coverage, the dissociative adsorption of HCl on the Cr terminated surface takes place with essentially unchanged adsorption energies of 1.06 and 1.20 eV. Here, the value of 1.06 eV corresponds to the case where the H atom adsorbs to the O atom, and the Cl atom adsorbs to the surface Cr atom, forming OH and CrCl complexes. The adsorption energy of 1.20 eV corresponds to the case where the H and Cl atoms adsorb to separate, but adjacent Cr atoms of the surface, forming CrH and CrCl complexes. Our results are in good agreement with Castillo et al.[21], who studied the dissociative adsorption of HCl on large surface unit cells, and with Alavi et al.[2], who investigated adsorption of HCl on α-Al_2O_3.

On the O terminated surface, the HCl molecule adsorbs dissociatively at 1 ML coverage with adsorption energy 0.21 eV and an energy barrier of 0.90 eV, see Fig. 5(a). In the final state, the Cl atom is bonded to a Cr atom that is pulled outside the surface layer of O atoms, similar to the geometry resulting from adsorption of Cl_2 on the (2×1) O terminated surface, discussed above. The H atom is bonded to one of the O atoms nearby. Dissociative adsorption of HCl becomes significantly more favored at a reduced coverage of 0.5 ML, with an adsorption energy 0.76 eV.

On the Cr=O terminated surface, HCl adsorbs molecularly with adsorption energies in the range 0.3 - 0.5 eV. Dissociative adsorption is slightly endothermic (by 0.13 eV) and needs to be activated by more than 3 eV.

TABLE III: Adsorption of 1 ML HCl on (1×1) surfaces. Surface denotes surface termination type, E_{ads}^{mol} and E_{ads}^{diss} denote molecular (IS) and dissociative (FS) adsorption energies, respectively, and E_a (eV) denotes activation energy. d_1 and d_2 (Å) are the two shortest O-H distances. IS, TS, and FS denote initial, transition, and final state, respectively.

				IS		TS		FS	
Surface/Figure	E_{ads}^{mol}	E_{ads}^{diss}	E_a	d_1	d_2	d_1	d_2	d_1	d_2
Cr=O	0.00	−0.13	3.20	1.99	4.88	2.01	3.11	0.99	2.24
O/5a	0.04	0.21	0.90	2.58	3.88	1.06	2.70	0.99	2.16
Cr	0.10	0.94	0.99	4.19	3.12	2.60	2.37	0.99	2.19
Cr/5b	0.07	1.22	0.19	3.72	3.12	2.94	3.14	1.01	2.24

3.5 Surface diffusion of H and Cl

After dissociative adsorption of H_2, Cl_2, or HCl, the chemisorbed H and Cl atoms may diffuse on the surface to nearby sites, which may be more or less stable than the initial site. We have chosen to model two such diffusion reactions with NEB calculations, as explained in Section 2. We have focused on "vertical diffusion", with the adsorbate atom bonded to the O atom of the Cr=O group in the initial state and the adsorbate atom bonded to the Cr atom of the Cr=O group in the final state.

With H as the adsorbate, the initial state is 2.35 eV more stable than the final state. The energy barrier is 2.69 eV for this diffusion reaction, where H moves from the exposed OH group at the surface to the subsurface Cr atom. Assuming reversibility, the opposite diffusion reaction has an energy barrier of 0.34 eV. With Cl as the adsorbate, the initial state is 0.18 eV less stable than the final state. The energy barrier is only 0.22 eV. The reverse reaction, where Cl diffuses from the subsurface Cr to the surface O atom also has a low energy barrier, 0.40 eV. The calculated diffusion barriers are comparable with results obtained by Wu et al.[7] on the MgO(001)surface, where barrier heights for the diffusion of atomic H from the surface to the subsurface region are found to be in the range 0.37 - 1.52 eV.

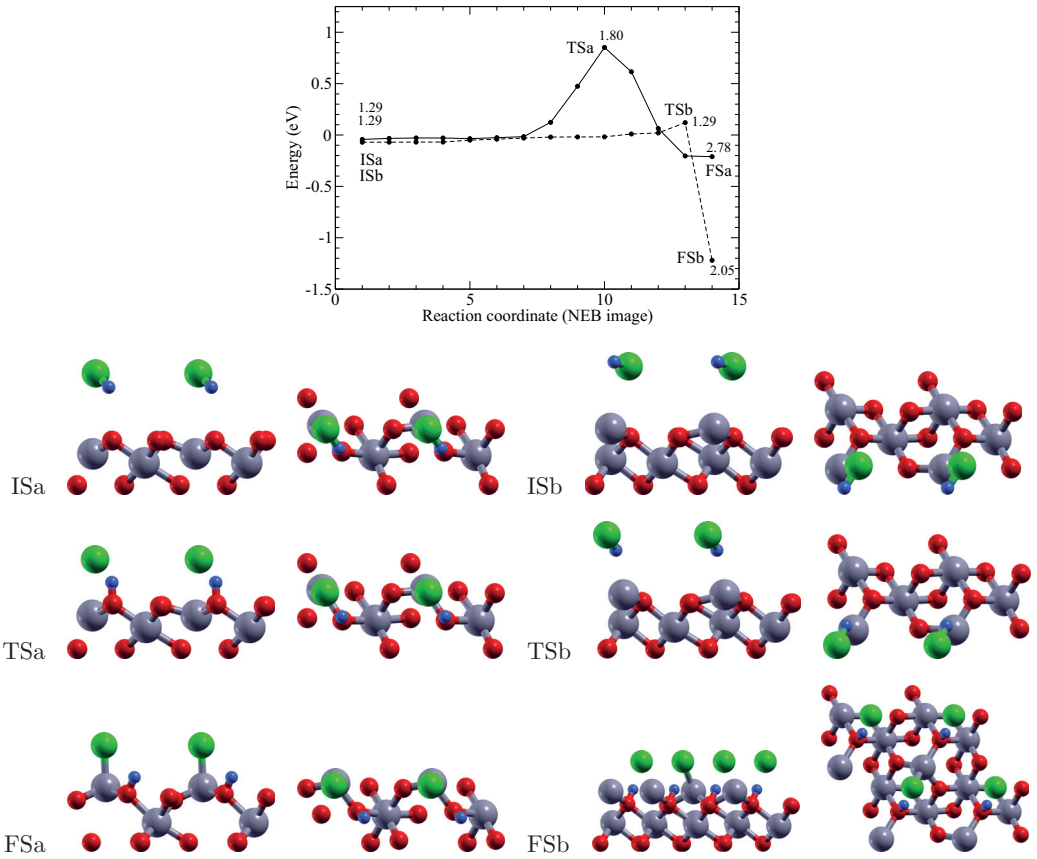

FIG. 5: (Color online) Reaction paths for HCl. a) Dissociation on the O terminated surface, leading to O-H and Cr-Cl complex formation. b) Dissociation on the Cr terminated surface, leading to O-H and Cr-Cl complex formation. The numbers above the curves denote the H-Cl distance. The top layers ($O_3Cr_2O_3$ in a and $O_3Cr_2O_3Cr$ in b) plus the adsorbate of two unit cells are shown, side view (left) and top view (right), in the initial (IS), transition (TS), and final (FS) states. Colors (size, grayscale): Cr-gray (large, medium gray), O-red (medium, dark gray), H-blue (small, medium gray), Cl-green (large, light gray).

4. Discussion

Dissociative adsorption of H_2, Cl_2, and HCl molecules are generally observed to be activated, with relatively high energy barriers, in the range 0.9 - 1.6 eV. Exceptions are the dissociative adsorption of Cl_2 and HCl on the Cr terminated surface, which happen with

energy barriers of 0.0 and 0.2 eV, respectively. This high reactivity of the Cl_2 molecule with surface metal atoms is also reported in previous studies on different surfaces, such as Ag/Mg(001), GaAs(110), MgO(001), TiO_2, and Si(001).[17],[18]-[22] Factors which may affect the energy barriers are the presence of defects (vacancies), temperature, and pressure. In the presence of defect sites, Cl_2 is observed to dissociate faster.[17],[18] At an increased temperature and pressure, H_2O is reported to dissociate with low or vanishing energy barrier depending on the extent of heating.[15]

In general, the rate of dissociative adsorption can be manipulated by varying the above mentioned factors as required. Thus, the obtained results for the energy barriers could imply different things in different experimental settings. For an experimenter working in ultrahigh vacuum conditions, a low or vanishing energy barrier for dissociation means that the molecules adsorb dissociatively at low temperatures. The desorption temperature depends on the adsorption energy, with the qualitative relation that high adsorption energy corresponds to high desorption temperature. A high dissociation energy barrier means that the molecules adsorb molecularly at low temperature and dissociatively at high temperature (i.e., after sufficient thermal activation is provided). For example, H_2O is reported to adsorb molecularly at 120 K and dissociatively at temperatures above 205 K.[13],[14] This observation is consistent with our findings, that H_2O may form a layer and sit above the Cr_2O_3(0001) surface with adsorption energies around 1 eV. Similar investigations have been reported.[9],[11]-[16] The variation in adsorption energies may be due to different monolayer phases being formed, as suggested by Harju et al.[9] They have suggested the formation of hexagonal buckled rings at low temperatures and the formation of a two-dimensional condensed hexagonal lattice at temperatures near a critical temperature of 319 K. This is analogous to our result for dissociative adsorption of H_2 on the Cr=O terminated surface, which may result in the formation of a relatively weakly bound H_2O layer or a somewhat more strongly bound H_2O complex (see Fig. 6).

For an experimenter working on an isotherm, a vanishing dissociation barrier would imply that the molecules adsorb dissociatively even at very low pressure. A high dissociation barrier would suggest that the molecules adsorb molecularly at low pressure and dissociatively at high pressure. For example, pressure activated dissociative adsorption of H_2O has been reported.[9],[15] Similarly, the impact of defect sites on dissociative adsorption of H_2O on Cr_2O_3 (0001) surface [34] and Cl_2 on Ag/MgO(001) [17] has been reported.

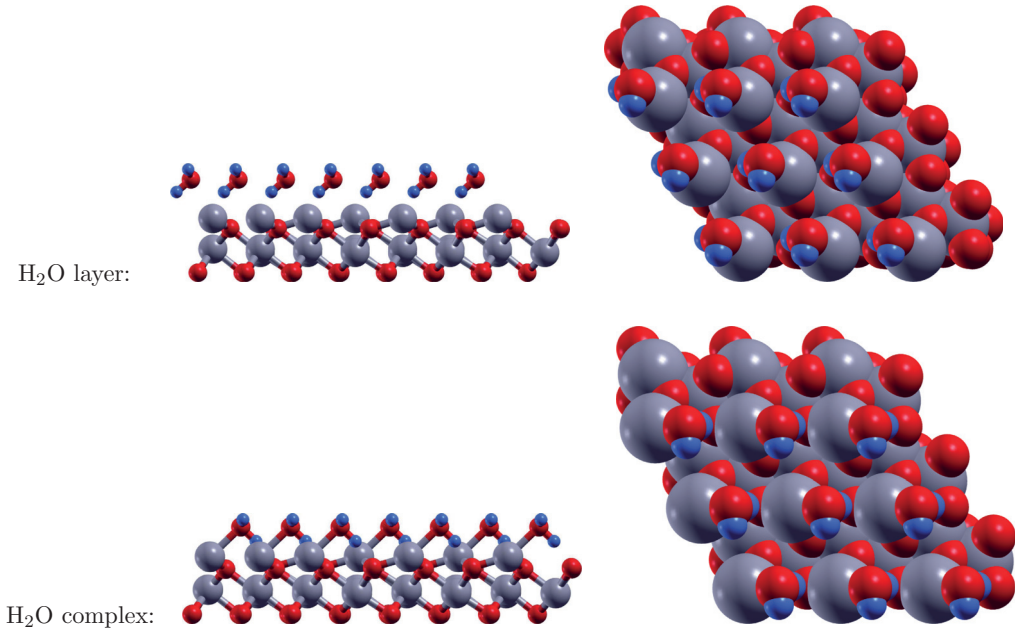

FIG. 6: Hexagonal structures of water formed by dissociative adsorption of H_2 on the Cr=O terminated surface. Upper figures: Weakly bound layer, Cr-O = 2.40 Å, E_{ads} = 1.05 eV. Bottom figures: More strongly bound complex, Cr-O = 2.14 Å, E_{ads} = 1.41 eV. A space filling model has been used in the top view (right figures) to emphasize the geometry of the adsorbed water layer. Colors (size, grayscale): Cr-gray (large, medium gray), O-red (medium, dark gray), H-blue (small, medium gray).

In ground state DFT calculations, temperature and pressure effects are to some extent addressed by varying the adsorbate coverage. Our calculations show that for dissociative adsorption, the energy barrier usually increases with increasing adsorbate coverage. There may be competing desorption phenomena taking place upon varying the temperature or the pressure, or alternatively, the adsorbate coverage. In a paper by Liao et al.[8], it is found that adsorption of H_2 on the Fe_3C (100) surface results in the formation of a CH_4 layer above the surface at high adsorbate coverages and the formation of CH complexes at lower coverages. This is similar to the adsorption of H_2 on the Cr=O terminated Cr_2O_3 (0001) surface, where we observe the possibility of formation of an H_2O layer at coverage 1 ML, but a strong preference for the formation of OH complexes at lower coverages.

The dissociative adsorption of HCl on the Cr_2O_3 (0001) surface is energetically comparable with that on the Al_2O_3 (0001) surface [2], especially when one compares the metal terminated versions of each surface (i.e., Cr and Al terminated, respectively). We have found dissociative adsorption energies upto 1.22 eV for HCl on the Cr terminated Cr_2O_3 (0001) surface at 1 ML adsorbate coverage. This value is about 0.3 eV smaller than for dissociative adsorption of HCl on Al terminated Al_2O_3 (0001).[2] Similar to the finding that HCl can adsorb molecularly with an adsorption energy of about 0.5 eV on the Al_2O_3 (0001) surface [2], we have observed molecular adsorption on the Cr=O terminated Cr_2O_3 (0001) surface with adsorption energies in the range 0.3 - 0.5 eV. Our investigation shows that HCl can adsorb dissociatively with an energy barrier as low as 0.19 eV on the Cr terminated surface at 1 ML adsorbate coverage. This indicates that the molecule can adsorb dissociatively essentially without energy barrier at low adsorbate coverages, similar to results obtained on Al_2O_3 (0001) [2], TiO_2 [21], and Ge(001)-c(2×4) [21]. It is also consistent with an experimental study on Cr_2O_3 (0001).[24]

5. Conclusion

Dissociative adsorption of H_2, Cl_2, and HCl on Cr, Cr=O, and O terminated surfaces of Cr_2O_3 (0001) has been studied with DFT calculations. Our main findings may be summarized as follows:

- Dissociative adsorption of H_2 is predicted to be activated with energy barriers E_a in the range 1.3 - 1.8 eV and adsorption energies in the range 1.0 - 2.2 eV.
- Adsorption of H_2 on the Cr=O terminated surface may result in the formation of a weakly bound H_2O layer, or a stronger bound H_2O complex above a Cr terminated surface. The opposite reaction, i.e., adsorption of water on the Cr terminated surface may therefore be relevant for hydrogen production and storage.
- Dissociative adsorption of Cl_2 is predicted to have zero barrier on the Cr terminated surface. However, it has high energy barriers of about 1.4 and 2.3 eV on the Cr=O and O terminated surfaces, respectively, the latter obtained at 0.5 ML coverage.
- Adsorption of 1 ML Cl_2 on the Cr terminated surface may result in a nearly perfect honeycomb lattice of Cl atoms, that may be interesting for further adsorption studies,

both from a theoretical and an experimental point of view. Rotation of the Cl_2 group between different conformations has low energy barriers of about 0.1 - 0.3 eV.

- Dissociative adsorption of HCl is predicted to have energy barriers as low as 0.2 eV on the Cr terminated surface. On the O terminated surface, the energy barrier is predicted to be 0.9 eV. In contrast, the Cr=O terminated surface is found to be essentially unreactive towards HCl, with $E_a > 3$ eV.

- The formation of H_2O complexes, H_2O layers, and $CrCl_2$ complexes are general characteristics at high adsorbate coverage (1.0 ML). At adsorbate coverages below 1 ML, the dissociated subunits of the molecules tend to adsorb to sites which are significantly far apart. As a result, only O-H and Cr-Cl bonds are energetically preferred. The investigated molecules are also observed to dissociate with lower or even vanishing energy barriers when the coverage is reduced from 1 to 0.5 ML.

Acknowledgments

NOTUR is gratefully acknowledged for computer time.

---

[1] A. Züttel, Mater Today **6**, 24 (2003).

[2] S. Alavi, D. C. Sorescu, and D. L. Thompson, J. Phys. Chem. B **107**, 186 (2003).

[3] K. N. Nigussa, K. L. Nielsen, Ø. Borck, and J. A. Støvneng, submitted to Corrosion Science.

[4] A. Biedermann, E. Knoesel, Z. Hu, and T. F. Heinz, Phys. Rev. Lett. **83**, 1810 (1999).

[5] K. D. Rendulic, G. Anger, and A. Winkler, Surf. Sci. **208**, 404 (1989).

[6] S. Wilke and M. Scheffler, Surf. Sci. **329**, L605 (1995).

[7] G. Wu, J. Zhang, Y. Wu, Q. Li, K. Chou, and X. Bao, Journal of alloys and compounds **480**, 788 (2009).

[8] X.-Y. Liao, D.-B. Cao, S.-G. Wang, Z.-Y. Ma, Y.-W. Li, J. Wang, and H. Jiao, Journal of Molecular Catalysis A: Chemical **269**, 169 (2007).

[9] M. Harju, T. Mäntylä, K. Vähä-Heikkilä, and V.-P. Lehto, Appl. Surf. Sci. **249**, 115 (2005).

[10] Ø. Borck, P. Hyldgaard, and E. Schröder, Phys. Rev. B **75**, 035403 (2007).

[11] S. Takada, M. Fukawa, Y. Hayashi, and K. Matsumoto, Thin Solid Films **339**, 220 (1999).

[12] S. Kittaka, T. Sasaki, N. Fukuhara, and H. Kato, Surf. Sci. **282**, 255 (1993).

[13] R. L. Kurtz and V. E. Henrich, Phys. Rev. B **36**, 3413 (1987).

[14] M. Hendewerk, M. Salmeron, and G. A. Somorjai, Surf. Sci. **172**, 544 (1986).

[15] D. S. Toledano, P. Metcalf, and V. E. Henrich, Surf. Sci. **472**, 21 (2001).

[16] Z. Łodziana, J. K. Nørskov, and P. Stoltze, J. Chem. Phys. **118**, 11179 (2003).

[17] Y. Li, Y. Zhang, L. Wu, Y. Xu, W. Chen, and J. Li, Chem. Phys. **328**, 236 (2006).

[18] Y.-J. Xu, J.-Q. Li, Y.-F. Zhang, and W.-K. Chen, J. Chem. Phys. **120**, 8753 (2004).

[19] M. Ménétrey, A. Markovits, and C. Minot, J. Mol. Sci. **808**, 71 (2007).

[20] A. Marcellini, C. A. Pignedoli, M. Ferrario, and C. M. Bertoni, Surf. Sci. **402-404**, 47 (1998).

[21] A. S. Castillo, G. H. Cocoletzi, and N. Takeuchi, Surf. Sci. **521**, 95 (2002).

[22] H. Okada, K. Inagaki, H. Goto, K. Endo, K. Hirose, and Y. Mori, Surf. Sci. **515**, 287 (2002).

[23] J. R. Falck, A. Bandyopadhyay, D. K. Barma, D.-S. Shin, A. Kundu, and R. V. K. Kishore, Tetrahedron Letters **45**, 3039 (2004).

[24] H. Pi, Y. Xiong, and S. Guo, Polymer-Plastics Technology and Engineering **44**, 275 (2005).

[25] http://wiki.fysik.dtu.dk/Dacapo.

[26] D. Vanderbilt, Phys. Rev. B **41**, 7892 (1990).

[27] J. P. Perdew, J. A. Chevary, S. H. Vosko, K. A. Jackson, M. R. Pederson, D. J. Singh, and C. Fiolhais, Phys. Rev. B **46**, 6671 (1992).

[28] H. J. Monkhorst and J. D. Pack, Phys. Rev. B **13**, 5188 (1976).

[29] H. Jonsson, G. Mills, and K. W. Jacobsen, in *Classical and Quantum Dynamics in Condensed Phase Simulations*, edited by B. Berne, G. Ciccoti, and D. Coker (World-Scientific, Singapore, 1998).

[30] G. Henkelman and H. Jonsson, J. Chem. Phys. **113**, 9901 (2000).

[31] D. R. Lide, *CRC Handbook of Chemistry and Physics* (CRC press, Boca-Raton, FL, 2004).

[32] J. Q. Li, Y. J. Xu, and Y. F. Zhang, Solid State Communications **126**, 107 (2003).

[33] M. I. McCarthy, A. C. Hess, N. M. Harrison, and V. R. Saunders, J. Chem. Phys. **98**, 6387 (1993).

[34] T. Bredow, Surf. Sci. **401**, 82 (1998).

PAPER III

Adsorption of H_2S on α-Cr_2O_3(0001) surfaces: A Density Functional Theory investigation

Submitted to Journal of Chemical Physics

Adsorption of H_2S on α-Cr_2O_3(0001) surfaces: A Density Functional Theory investigation

K. N. Nigussa, J. A. Støvneng,* and Ø. Borck

Department of Physics, NTNU, N-7491 Trondheim, Norway

(Dated: February 11, 2011)

Abstract

The interaction between dihydrogen sulfide (H_2S) and Cr as well as Cr=O terminated Cr_2O_3(0001) surfaces is studied with density functional theory (DFT). Calculations are carried out at 0.5 and 1.0 monolayer (ML) adsorbate coverages. We find that the reactivity of H_2S and its dissociated species is stronger to the Cr terminated surface than to the surface terminated by Cr=O groups. For the coverages studied, the dissociative adsorption as H and HS species is found to be favored on the Cr terminated surface, with adsorption energies around 0.9 eV when CrS fragments are formed, with S located above the hollow fcc site of the surface O atoms. Calculated adsorption energies are in the range 0.4 - 0.6 eV for molecular adsorption on the Cr terminated surface. Activation energies for dissociative adsorption are predicted in the range 0.3 - 0.5 eV at 0.5 ML coverage and in the range 0.6 - 1 eV at 1.0 ML coverage. For coverages well below 0.5 ML, the dissociative adsorption as H, H, and S species is predicted to be the favored process, with formation of CrH and CrS fragments and with S located above the hollow fcc site of surface O atoms on the Cr terminated surface, and in a bridging site between surface Cr and O atoms on the Cr=O terminated surface.

*Correspondence to:jon.stovneng@ntnu.no

1. Introduction

The presence of H_2S in various systems has been reported to have corrosive [1],[2], catalyst poisoning [3],[4], and atmospheric poisoning effects [5] . The S component of the molecule is believed to be the cause of the poisoning. The literature indicates a loss of resources every year due to the S poisoning, with an estimated worth of millions of dollars [6]. Designing good solutions to the problem requires a detailed understanding of the decompositive reaction of the molecule in the systems of interest. The mechanism of decomposition can be seen as twofold. In systems with excess oxygen, the molecule can decompose to form sulfur dioxide and water [7]. Here, the formed SO_2 is harmful in two ways. When it is released to the atmosphere, it pollutes the air and causes acidic rain [5]. On the other hand, when it is bound to the system, it can react with O centers, leading to the formation of acidic sulfates such as SO_3 and SO_4 [8]. In systems without enough oxygen present, the decomposition leads to the formation of elemental sulfur and water [7],[9]. The sulfur species interact with metal centers of the surface, forming complexes of metal sulfides [10].

A comparison of the dissociation tendency of the H_2S molecule with other sulfur containing molecules, such as alkanethiols on Au(111) [11], Cu(111) [12], and Ag(111) [13], indicates that H_2S prefers to adsorb dissociatively rather than molecularly, as opposed to the alkanethiols. Hence, at room temperature, the major source of sulfur poisoning would be H_2S. Rodriguez et al. [14],[15] have shown that H_2S dissociates faster on oxides with small band gaps. Thus, one may expect significant dissociation of H_2S on oxides such as Cr_2O_3, which can have surface band gaps close to zero when terminated by O atoms, or which tend to have a metallic character when terminated by Cr atoms. At room temperature, and at very low adatom coverages, low-energy electron diffraction (LEED) patterns show that the S atom binds to the metal sites of surfaces resuming $(\sqrt{3} \times \sqrt{3})$R30° [13], p$(2 \times 2)$ [16], and diffuse $(\sqrt{3} \times \sqrt{3})$R30° [17] super structures.

In a broader sense, studies of the interaction of H_2S with different surfaces is useful for several reasons. First, it can be used to find oxides that could be used as sorbents for removing molecules containing sulfur [18]. Second, it helps to design approaches [19] that minimize the effect of sulfur poisoning, thereby increasing the lifetime of a surface once it is exposed to such molecules. A comparison can be made with studies of H_2O on $Cr_2O_3(0001)$ [20], where it is shown that desorption of the molecularly chemisorbed H_2O

occurs at temperature $T = 295$ K, while desorption of the dissociatively adsorbed H_2O occurs at $T = 345$ K. For the interaction of H_2S with $Cr_2O_3(0001)$ [21], desorption of molecularly adsorbed H_2S occurs at temperatures $T \sim 100 - 200$ K, while the desorption of dissociated H_2S occurs at temperature $T = 300$ K. This shows that although the two molecules have a similar structure, their interaction with the chromium oxide surface is rather different.

Dissociative adsorption of H_2O has been found to have a corrosive effect [22]. An analysis of the interaction between atomic species and $Cr_2O_3(0001)$ [23] shows that it is the reduction of the surface oxygen atoms by the H cations that predominantly leads to the corrosion. Due to the presence of hydrogen, the two molecules H_2O and H_2S are similar when it comes to corrosive effects. However, the poisoning effect is rather caused by the sulfur species, which is absent in the water molecule. We have previously emphasized the corrosive effect of sulfur [23]. Here, we focus on its poisoning effect.

The interaction of H_2O and H_2S with the chromium oxide surface is not always harmful. For example, through oxidation of surface Cr atoms by the H_2O molecule, H_2 could be liberated and be used as a source of energy [24]. A similar technique of hydrogen recovery by oxidation [25] could be envisioned via decomposition of H_2S. Several studies of the interaction of H_2S with different oxides have been carried out by Rodriguez et al. [14],[17],[21]. The present study offers supplementary understanding through first principles calculations on the interaction of this molecule specifically on the $Cr_2O_3(0001)$ surface considering the possibilities of termination by Cr atoms or Cr=O groups. We focus on the adsorptive interaction of the intermediate (HS and H) and final (S, H, and H) decompositive species with the surface, in addition to the molecular state. The paper is organized as follows. In section 2, we present the computational method. The results are presented in section 3. Sections 4 and 5 contain a discussion and the conclusions, respectively.

2. Computational method

The DFT calculations are carried out using the Dacapo code [26] based on ultrasoft pseudopotentials [27]. The wave functions of the electrons are expanded in a plane wave basis with cutoff energy set to 400 eV. For the treatment of the electron exchange and correlation energies, we have used the generalized gradient approximation (GGA) of PW91 [28]. The k-point meshes are chosen based on the Monkhorst-Pack [29] scheme and values

of $4 \times 4 \times 1$, $2 \times 4 \times 1$, and $2 \times 2 \times 1$, respectively, are used for the calculations on the (1×1), (2×1), and (2×2) surface unit cells. The surfaces are modeled by a four layer slab with terminations by Cr=O groups or Cr atoms in the top layer. The ions in the top three layers are allowed to relax based on a BFGS geometry optimization scheme until the total force on each atom falls below 0.05 eV/Å. Adsorptions are modeled by putting the molecules on one side of the slab, and the corresponding adsorption energies are calculated by

$$E_{ads} = -(E_{SM} - E_S - E_M), \tag{1}$$

Here, E_S, E_M, and E_{SM} are the total energies of the clean surface, isolated molecule, and relaxed geometry containing both substrate and molecule, respectively. All energies are per supercell. The GGA based DFT calculations are known to predict adsorption energies within an error of about 0.2 eV [30]. Adsorbate coverage is expressed in terms of surface Cr atoms: 1.0 ML means one adsorbed molecule per surface Cr atom, and 0.5 ML means one adsorbed molecule per two surface Cr atoms. The reaction paths are calculated with the nudged elastic band (NEB) method [31],[32], and the minimum energy paths are searched for using a quasi-Newton iterative scheme by mapping out images between two preset geometries. The Bader analysis [33] of charges is based on work by Henkelman et al. [34] and Sanville et al. [35].

From the general exponential relation between desorption rate and temperature [37], the amount of desorbed species in a thermal desorption (TPD) experiment can be assumed to be uniform around the maximum desorption peak. For a first order type of kinetics, this assumption would imply a linear relation between the predicted desorption (or activated adsorption) temperature and the calculated adsorption (or activation) energy, which can be given as follows,

$$T \simeq \frac{E}{33 k_B}. \tag{2}$$

Here, k_B is the Boltzmann constant, and T yields an estimate for the desorption temperature T_d when the adsorption energy E_{ads} is used for E, or the activated adsorption temperature T_a when the activation energy E_a is used for E. The numerical factor in this expression can also be estimated on the basis of a comparison between calculated adsorption (or activation) energies and the corresponding measured desorption (or activated adsorption) temperatures. For example, a previously obtained adsorption energy of 0.80 eV at 1 ML coverage of molecular H_2O on the Cr terminated surface [39] and the corresponding experimentally observed

desorption temperature of 295 K [20] yields approximately 1/31 in the above equation. When appropriate, calculated values of E_{ads} (or E_a) will be compared to experimental values for T_d (or T_a).

3. Results

The calculated values of the bond length $d_{\mathrm{H-S}}$ and the bond angle $\angle$HSH of the gas phase H_2S molecule are 1.35 Å and 91.7°, respectively. These are in good agreement with the experimental values [38] of 1.33 Å and 92.2°. The interaction of the molecule with the surfaces terminated by Cr atoms (denoted as surface **A**) and Cr=O groups (denoted as surface **B**) is presented in the following subsections.

3.1 Surface A: Termination by Cr atoms.

3.1.1 Molecular adsorption

The H_2S molecule adsorbs molecularly with adsorption energies in the range 0.22 - 0.37 eV at 1 ML coverage (Fig. 1), and in the range 0.24 - 0.62 eV at 0.5 ML coverage (Fig. 2). The rather low adsorption energies, at least when compared to the H_2O molecule (see end of section 2), indicate that in the molecular state, H_2S interacts only weakly with the surface. Estimating the desorption temperatures from Eq. (2), we obtain values in the range 77 - 130 K at 1 ML coverage and 84 - 218 K at 0.5 ML coverage. This is comparable with the experimental values in the range 100 - 200 K [21]. Moreover, it was explained in Ref. [21] that H_2S physisorbs at lower temperatures and gradually forms a multilayer as the temperature is increased, before it desorbs. In Figs. 1 and 2, we present various orientations of H_2S at 1 and 0.5 ML coverage, respectively, corresponding to physisorption (Figs. 1a, 1b, 2a) or molecular chemisorption (Figs. 1c, 2b, 2c, 2d). Here, we have, somewhat arbitrarily, chosen a minimum binding energy of 0.3 eV for using the term chemisorption.

At 1 ML coverage, the physisorption of H_2S with S located on top of the surface Cr atom, Fig. 1a, is less favorable than with S located above the hollow fcc site of the surface O atoms, Figs. 1b and 1c. This trend is opposite to what we have found for adsorption of an isolated S atom [23]. The observed above hollow site preference is different from the strict on top sites found in metallic systems such as Cu(111), Au(111), Pd(111), and Pt(111) [40],[41].

TABLE I: Molecular (adsorbate H_2S), partly dissociative (adsorbates HS, H), and fully dissociative (adsorbates S, H, H) adsorption of dihydrogen sulfide on Cr terminated (surface **A**) and Cr=O terminated (surface **B**) $Cr_2O_3(0001)$ at adsorbate coverages of 1 monolayer (ML) ($\Theta = 1$) and 0.5 ML ($\Theta = 1/2$). E_{ads}: adsorption energy (eV); Q_S: atomic (Bader) charge on S (e).

Adsorbate	Surface	Θ	Figure	E_{ads}	Q
Free H_2S					−0.11
H_2S	**A**	1	1c	0.37	−0.11
		$\frac{1}{2}$	2c	0.52	−0.12
		$\frac{1}{2}$	2d	0.62	
	B	1	6a	0.19	−0.14
		$\frac{1}{2}$	7a	0.24	−0.17
		$\frac{1}{2}$	7b	0.26	
HS, H	**A**	1	3d	0.90	−0.31
		$\frac{1}{2}$	4c	0.91	−0.41
	B	1	6b	−0.12	−0.42
		$\frac{1}{2}$	7c	0.34	−1.06
S, H, H	**A**	1	-	0.06	−0.43
		$\frac{1}{2}$	5	0.56	−0.62
	B	1	6c	−0.37	−0.63
		$\frac{1}{2}$	7d	0.32	−1.32

The calculated separation distances between the atoms are as follows: In the site on top of Cr, $d_{\mathrm{Cr-S}} = 2.94$ Å and the shortest O-S distance is 3.55 Å (Fig. 1a). In the least stable hollow fcc site, $d_{\mathrm{Cr-S}} = 2.78$ Å and the shortest O-S distance is $d_{\mathrm{O-S}} = 3.24$ Å (Fig. 1b). In the most stable hollow fcc site, $d_{\mathrm{Cr-S}} = 2.79$ Å and the shortest O-S distance is $d_{\mathrm{O-S}} = 3.23$ Å (Fig. 1c).

At 0.5 ML, the trend in site preference is the same, but the molecule sits closer to one of the adjacent CrO_3 units of the surface. The corresponding separation distances between the atoms are as follows: In the site on top of Cr (Fig. 2a), $d_{Cr-S} = 2.85$ Å and the shortest O-S distance is 3.51 Å. In the site above the bridge (Fig. 2b), $d_{Cr-S} = 2.92$ Å and the shortest O-S distance is $d_{O-S} = 3.50$ Å. In the first hollow fcc site (Fig. 2c), $d_{Cr-S} = 2.69$ Å and the shortest O-S distance is $d_{O-S} = 3.05$ Å. In the second hollow fcc site (Fig. 2d), $d_{Cr-S} = 2.76$ Å and the shortest O-S distance is $d_{O-S} = 3.15$ Å. More interesting, perhaps, is the short $O\cdots H$ distance of 2.01 Å, indicative of stabilizing hydrogen bonding. This is confirmed by a corresponding elongation of one of the S-H bonds, from the typical value of 1.35 Å to 1.37 Å.

As expected, the calculated adsorption energy becomes somewhat higher for a given site, when the adsorbate coverage is reduced from 1 to 0.5 ML. This is accompanied by reduced Cr-S and O-S distances, in particular for the most stable location of S above the hollow fcc of the surface O atoms.

3.1.2 Partly dissociative adsorption as H and HS subunits

The partial dissociation of H_2S on the surface as H and HS subunits is strongly favorable, with adsorption energies in the range 0.54 - 0.90 eV at 1 ML (Fig. 3) and 0.66 - 0.91 eV at 0.5 ML coverage (Fig. 4). Corresponding estimates of desorption temperatures, on the basis of Eqn. (2), lie in the range 190 - 319 K. Photoemission experiments [21] suggest the presence of the HS fragment on the Cr_2O_3 surface at temperatures down to 100 K and up to somewhere between 250 and 300 K.

The HS fragment bonds to the surface by the formation of a Cr-S bond. At 1 ML coverage, the Cr-S bond length lies in the range 2.23 - 2.44 Å (Fig. 3). At 0.5 ML coverage, it lies in the range 2.20 - 2.26 Å (Fig. 4). Studies on different systems, such as MgO(100), ZnO(0001), Ru(110), and Au(111) [14],[42],[44] have also demonstrated that HS bonds to the metal centers at the surface, via the S atom.

At 1 ML coverage, the prefered geometry has the S atom located above the hollow fcc site of the surface O atoms (Fig. 3d). The structure appears to be stabilized by an attractive interaction between the S atom and the H atom of the OH fragment, resulting in an elongated O-H bond of 1.02 Å and a relatively short $S\cdots HO$ distance of 2.10 Å. The structure in Fig.

3c is similar to the one in Fig. 3d, but here, the S atom is located above a Cr-Cr bridge, and the S$\cdots$HO distance is somewhat longer, 2.28 Å. The preference of having S located in a hollow fcc site *or* above a Cr-Cr bridge site at 1 ML coverage on Cr_2O_3 may be compared with the pure bridge site preference found on noble metal surfaces, such as Cu(111) and Au(111) [40], and on transition metal surfaces, such as Pd(111) and Pt(111) [41]. Naturally, the H atom prefers to bond to the surface O atoms at 1 ML coverage (Fig. 3), since each surface Cr atom is already occupied by an HS fragment. However, at 0.5 ML coverage, the H atom prefers to bond to the second surface Cr atom of the (2×1) supercell (Fig. 4c) rather than to the (sub-)surface O atom (Figs. 4a and 4b). This is consistent with the observation that atomic hydrogen prefers to form a metal hydride (CrH) rather than a hydroxyl (OH) group on the Cr terminated surface [23].

3.1.3 Fully dissociative adsorption as H, H, and S subunits

At 1 ML coverage, the full dissociative adsorption on the Cr terminated surface results in the formation of one CrS and two OH complexes, with a low adsorption energy of 0.06 eV (see Table I). The S atom is located above the hollow fcc site of surface O atoms at an average O-S distance of 3.17 Å and with $d_{\mathrm{Cr-S}} = 2.08$ Å. This geometry (not shown here) is obtained e.g. by transfering the H atom of the HS fragment in Fig. 3d to one of the surface O atoms below. In view of the discussion above, it is not surprising to find that the adsorption energy increases to 0.56 eV when the coverage is reduced to 0.5 ML. In the resulting geometry (shown in Fig. 5), one of the H atoms is bonded to the second surface Cr atom of the (2×1) supercell, once again illustrating the preference of forming CrH groups instead of OH groups on this surface.

This trend is expected to continue at even lower coverage, since below a coverage of 1/3 ML, the optimal configuration with S and the two H atoms bonded to individual surface Cr atoms becomes possible. If interactions between the CrS and CrH groups are neglected, the expected adsorption energy at low coverage is 0.91 eV. This estimate is based on adsorption of atomic H and S on the Cr terminated surface [23]. Studies of adsorption of H_2S at 0.25 ML adsorbate coverage on different oxide systems such as MgO(100) and ZnO(0001) [14] have indeed shown that full decompositive adsorption as H, H, and S is energetically the most favorable, and even with adsorption energies considerably higher than for the present

surface. Our estimate of 0.91 eV on $Cr_2O_3(0001)$ corresponds to a characteristic temperature of about 319 K. This is consistent with the experimental observation that Cr_2O_3 decomposes H_2S into S around or somewhat below 300 K [21]. The S adatom is known to stay on certain surfaces even after heating beyond 500 K [14]. Around 500 K, the presence of the S adatom likely changes the surface morphology of the substrate [21].

Dissociation of H_2S by formation of a CrS fragment on the surface and the liberation of an H_2 molecule is endothermic by 0.48 eV. The corresponding H_2 liberating dissociative adsorption of H_2O on the Cr terminated surface is endothermic by 0.61 eV. Therefore, it seems that H_2 extraction [24] on this surface is approximately equally easy with H_2S and with H_2O, at least from a thermodynamic point of view. Various methods [25] have been used as alternative ways of extracting hydrogen from H_2S.

3.2 Surface B: Termination by Cr=O groups.

3.2.1 Molecular adsorption

Our calculations show that H_2S is much less reactive to the Cr=O terminated surface (surface **B**) than to the Cr terminated surface (surface **A**). At 1 ML coverage, the most stable adsorption geometry has the molecule located in the threefold hollow site between the surface Cr=O groups (Fig. 6a), with one of the H atoms pointing towards the surface. The adsorption energy is 0.19 eV, and the corresponding estimate of the desorption temperature is 68 K. At 0.5 ML coverage, the adsorption energy has increased slightly, to 0.24 eV (Fig. 7a) or 0.26 eV (Fig. 7b), with corresponding desorption temperatures of 84 K and 91 K. The adsorption energies are significantly lower with surface **B** than with surface **A**. Reduced coverages of 0.25 ML or lower would probably increase the adsorption energies and the corresponding desorption temperatures slightly, but the trend that H_2S is less reactive to surface **B** than to surface **A** is expected to remain.

3.2.2 Partly dissociative adsorption as H and HS subunits

As shown in Table I, the dissociative adsorption of H_2S as H and HS is endothermic by 0.12 eV at 1 ML coverage on surface **B**. In the resulting geometry, shown in Fig. 6b, both the HS and the OH fragment are bonded to the surface Cr atom. The O-H bond of the

hydroxyl group is slightly elongated (1.01 Å), indicating a weakly stabilizing hydrogen bond between the hydroxyl H atom and the S atom (see top view in Fig. 6b). The situation is quite different at 0.5 ML coverage. The most favorable adsorption geometry (Fig. 7c) has the HS subunit bonded to the surface O atom through the S atom, and it is located above a hollow fcc site of the deep lying surface O atoms, whereas the H atom bonds to the O atom of the adjacent Cr=O fragment. The various bond distances are $d_{\mathrm{O-S}} = 1.66$ Å, $d_{\mathrm{S-H}} = 1.37$ Å, and $d_{\mathrm{O-H}} = 0.99$ Å. The normal O-H bond length shows that there is no stabilizing hydrogen bonding in this geometry. The adsorption is exothermic, by 0.34 eV. A decomposition temperature of about 119 K is estimated corresponding to this energy. Also here, it is reasonable to expect a slight increase in the decomposition temperature at lower coverages. However, the stability of the H and HS species on this surface is expected to be rather low.

3.2.3 Fully dissociative adsorption as H, H, and S subunits

At 1 ML coverage, the full decompositive adsorption as H, H, and S subunits is found to be endothermic by 0.37 eV. The S atom bonds to the Cr atom, one H atom bonds to the O atom of the Cr=O group, and one H atom bonds to a subsurface O atom (see Fig. 6c). The location of the S atom enables hydrogen bonding to the H atom bonded to the subsurface O atom. The most relevant bond lengths are are $d_{\mathrm{Cr-S}} = 2.07$ Å, $d_{\mathrm{O-H}} = 0.99$ Å (surface OH group) and 1.01 Å (subsurface OH group), and $\mathrm{H}\cdots\mathrm{S} = 2.09$ Å. At 0.5 ML coverage, the energetics is significantly improved, and the reaction is exothermic by 0.32 eV. The estimated decompositive temperature is 112 K. The adsorption geometry (Fig. 7d) has the S atom in a bridging position between the surface Cr and one of the subsurface O atoms. The two H atoms are bonded to O atoms in separate Cr=O fragments. The bond distances are $d_{\mathrm{Cr-S}} = 2.21$ Å, $d_{\mathrm{O-S}} = 1.67$ Å, and $d_{\mathrm{O-H}} = 0.98$ Å and 1.00 Å. The latter value suggests hydrogen bonding between the two hydroxyl groups, and the relevant $\mathrm{O}\cdots\mathrm{H}$ distance is indeed rather short, 1.92 Å.

3.3 Surface reactions: molecular reorientation and partial and full dissociation.

In the previous subsections, we have presented minimum energy structures corresponding to molecular adsorption, as well as partial and full dissociative adsorption of H_2S on the Cr and Cr=O terminated surfaces. In an attempt to estimate activation energies for the various surface reactions resulting in these minimum energy structures, a number of nudged elastic band (NEB) calculations have been performed, with a selection of the structures presented in Table I and Figs. 2 - 7 as initial (IS) and final (FS) states of the NEB reaction paths.

A summary of these calculations is presented in Table II and Figs. 8 - 10. Note that the activation energies E_a and the corresponding transition state (TS) geometries should be considered as approximate, in the sense that they have not been subject to formal verification in terms of vibrational analyses. As such, we expect our E_a values to be upper rather than lower estimates of the true activation energies.

As expected, the energy barriers for reorientation of molecularly adsorbed H_2S are relatively low, 0.02 eV and 0.23 eV on surface **A** and **B**, respectively (see Fig. 8). The reverse reactions have barriers of 0.30 and 0.25 eV, respectively. Partial dissociative adsorption at 1.0 ML coverage is found to be activated with energy barriers of 0.65 and 1.01 eV on surface **A** and **B**, respectively (see Fig. 9). In terms of Eqn. (2), this corresponds to adsorption activation temperatures T_a of about 228 and 355 K, respectively. The reaction on surface **A** is predicted to proceed via a transition state (TS9A) where the H atom is transfered to Cr before it reaches its final destination on oxygen (Fig. 3d). On surface **B**, transfer of an H atom to O in the Cr=O group (TS9B) is predicted to take place prior to formation of the Cr-S bond between Cr and the SH fragment (Fig. 6b).

Full dissociative adsorption into H, H, and S subunits is modeled at 0.5 ML, with molecularly adsorbed H_2S as initial states (Figs. 2d and 7b). The transition states (TS10A and TS10B) correspond to activation energies of 0.45 and 0.37 eV on surface **A** and **B**, respectively, and represent transfer of one of the H atoms, to Cr and O, respectively, as the first of two reaction steps. This is particularly clear on surface **A**, where a well defined intermediate state (Fig. 4c) is reached, with the SH and H subunits bonded to separate Cr atoms. A second barrier of 0.52 eV must be overcome in order to have the second H atom transfered, from S to O (Fig. 5). On surface **B**, the intermediate structure is less well defined (in terms of complete atom transfer and bond formation), but also in this case, a (low) second en-

ergy barrier must be overcome before the final state is reached, with two hydroxyl groups and the S atom in a bridging position between Cr and a subsurface O (Fig. 7d). For the full dossociative adsorption reactions, the estimated activation energies would correspond to adsorption activation temperatures in the range 130 to 183 K. Taking into account the two step character of these reactions, it is reasonable to arrive at lower activation energies in Fig. 10 than in Fig. 9. After all, the individual reaction steps essentially amount to the transfer of an H atom, to Cr or O, at 1.0 ML coverage in Fig. 9 and at 0.5 ML coverage in Fig. 10.

4. Discussion

Our results show that surface **A** is more reactive to the H_2S molecule than surface **B**. This is consistent with the literature [14] from the point of view that the presence of more Cr atoms at the surface gives it a metallic character in the top layer, and hence a lower band gap. Note, however, that the reactivity in the present case is low compared to truly metallic systems [41]. We find that partial dissociation in terms of H and HS subunits represents the most stable configuration on surface **A** at 1.0 and 0.5 ML coverages. However, the trends in adsorption energies (Table I) suggest that the full decompositive adsorption yielding S adatoms could be the most stable adsorptive process at lower coverages. As already mentioned, the latter case has also been found in different oxide and metallic systems [14],[41]. With adsorbate coverages significantly greater than 1 ML, it is likely that molecular adsorption dominates. However, the investigated molecular adsorptions are already relatively weak at 0.5 and 1 ML adsorbate coverage, and going to higher coverages would likely give even lower adsorption energies.

For all three types of adsorption on surface **A**, the favored location of the S subunit (i.e., H_2S, HS, or S) tends to be above the hollow fcc site of the surface oxygen atoms (Figs. 1b, 1c, 2c, 3d, 5), with S bonded to Cr. The charge calculations show that there is strongest charge transfer in the case of adsorption as S adatom. This indicates that the full decompositive adsorption as H, H, and S adatoms likely poses the most serious threat to the reactive functioning of the surface. In fact, studies [43] have shown that the S adatom could persist on surfaces well above 1000 K by forming superstructures. The surface would then have different catalytic and other properties compared to the clean one.

The decompositive adsorption appears to form CrS and CrH complexes at low coverage (shown in Fig. 5). The latter complex (metal hydride) has not been mentioned in the relevant literature [7]-[10]. Compared with the results for adsorption of water on this surface [20],[39], molecular adsorption of H_2S is weaker than molecular adsorption of H_2O. On the other hand, dissociative adsorption as HS admolecule is stronger than dissociative adsorption as OH admolecule on surface **A**.

The dynamics is rather different on surface **B**. At 1 ML coverage, the molecular adsorption as H_2S, itself being weak, is found to be the most stable. By decreasing the coverage to 0.5 ML, the stability of the dissociated species (i.e., HS admolecule and S adatom) increases, surpassing that of the molecular adsorption. The dissociative adsorption as HS admolecule seems to be slightly favored. The trend in the adsorption energies (Table I) shows also here that the dissociative adsorption as S adatom would probably be most stable at lower coverages, while the molecular adsorption continues to be more stable at higher coverages, although it is being further weakened.

At 1 ML coverage, the most stable adsorption geometries have the S subunit located above or in the hollow fcc site of the surface O atoms (Fig. 6a, 6b) or the subsurface O atoms (Fig. 6c). At 0.5 ML coverage, the S subunit rather tends to be located in various bridging positions (Fig. 7b, 7c, 7d). These results can be compared with the reports of a bridge site preference by the HS admolecule and a hollow fcc site preference by the S adatom [40],[41], and a bridge site preference by both the HS admolecule and the S adatom [45]. The full decompositive adsorption here yields CrS and hydroxyl complexes. The prospect of decompositive adsorption producing metal sulfide and H_2O complexes [7],[9],[10] is somewhat better on surface **B** than on surface **A**. This is due to the higher presence of oxygen atoms at surface **B**. The scenario can be traced back to the oxygen terminated surface [23], which has an even higher presence of oxygen atoms at the surface than surface **B**. In that case, the decompositive adsorption could result in the formation of SO_2 and H_2O complexes, which in turn could be similar to what has been reported in the literature [7]. However, this process would likely also be an endothermic (activated) process.

5. Conclusion

Molecular and dissociative adsorption of H_2S on Cr and Cr=O terminated surfaces of $Cr_2O_3(0001)$ has been investigated with DFT calculations. The main results of this study are:

- The Cr terminated surface (surface **A**) is more reactive to H_2S and its dissociated species than the Cr=O terminated surface (surface **B**).
- In general, adsorption energies increase upon reducing the adsorbate coverage. This effect is most pronounced for full decompositive adsorption as H, H, and S adatoms, and suggests that the latter represents the favored situation at low coverage. This poses the largest threat to the reactive functioning of the surface.
- For molecular adsorption as H_2S, adsorption energies lie in the range 0.4 - 0.6 eV on surface **A** and around 0.2 eV on surface **B**.
- Partially dissociative adsorption as HS and H is favored on surface **A**, especially at high coverage, with adsorption energies around 0.9 eV.
- Reaction path calculations provide estimates of activation energies for molecular reorientation on the surface (0 - 0.3 eV), as well as decompositive adsorption at low coverage (0.3 - 0.5 eV) and high coverage (0.6 - 1 eV).
- The low reactivity of the Cr=O terminated surface suggests a mechanistic design in terms of preexposing the surface to oxygen in order to prevent the attack by H_2S. The oxygen atoms could subsequently be removed from the surface by exposing the surface to H_2.
- Adsorption on sulfur covered α-$Cr_2O_3(0001)$ could represent a way to investigate quantitatively how properties change when compared to adsorption on the clean surface.

Acknowledgments

NOTUR is gratefully acknowledged for computer time.

[1] J. Speight, *The Chemistry and Technology of Petroleum*, 2nd ed. (New York, 1991).

[2] T.J. Pan, F. Gesmundo, and Y. Niu, Corrosion Science **49**, 1362 (2007).

[3] J. Oudar and H. Wise, *Deactivation and Poisoning of Catalysts* (New York, 1991).

[4] C. Bartholomew, P. Agrawal, and J. Katzar, Adv. Catal. **31**, 135 (1982).

[5] A. Stern, R. Boubel, D. Turner, and D. Fox, *Fundamentals of Air Pollution*, 2nd ed. (Academic, Orlando, Florida, 1984).

[6] H. Topsøe, B. Clausen, and F. Massoth, *Hydrotreating Catalysis* (Springer-Verlag, New York, 1996).

[7] J. Uhm, M. Shin, J. Zhidong, and J. Chung, Appl. Catal. B: Environmetal **22**, 293 (1999).

[8] G. Pacchioni, A. Clotet, and J. Ricart, Surf. Sci. **315**, 337 (1994).

[9] T.V. Reshetenko, S.R. Khairulin, Z.R. Ismagilov and V.V. Kuznetso, International Journal of Hydrogen Energy **27**, 387 (2002).

[10] T. Jirsak, J. Dvorak, and J.A. Rodriguez, J. Phys. Chem. B **103**, 5550 (2000).

[11] P.G. Lustemberg, M.L. Martiarena, A.E. Martinez, and H.F. Busnengo, Langmuir **24**, 3274 (2008).

[12] J. Zhou, Q.L. Williams, and F. Hagelberg, Phys. Rev. B **77**, 035402 (2008).

[13] R. Heinz and J.P. Rabe, Langmuir **11**, 506 (1995).

[14] J.A. Rodriguez and A. Maiti, J. Phys. Chem. B **104**, 3630 (2000).

[15] J.A. Rodriguez, S. Chaturvedi, M. Kuhn, and J. Hrbek, J. Phys Chem B **102**, 5511 (1998).

[16] S.R. Kelemen and T.E. Fischer, Surf. Sci. **87**, 53 (1979).

[17] J.A. Rodriguez, S. Chaturvedi, M. Kuhn, J. van Ek, U. Diebold, P.S. Robbert, H. Geisler, and C.A. Ventrice, J. Chem. Phys. **107**, 9146 (1997).

[18] J.N. Armor, *Environmental Catalysis* (ACS Symposium Series No. 552, American Chemical Society, Washington DC, 1994).

[19] N.M. Galea, J.M.H. Lo, and T. Ziegler, Journal of Catalysis **263**, 380 (2009).

[20] M.A. Henderson and S.A. Chambers, Surf. Sci. **449**, 135 (2000).

[21] J.A. Rodriguez, T. Jirsak, M. Pérez, S. Chaturvedi, M. Kuhn, L. González, and A. Maiti, J. Am. Chem. Soc. **122**, 12362 (2000).

[22] H. Amsteman, K. Segerdahl, J.-E. Svensson, and L.-G. Johansson, Materials Science Forum **369**, 277 (2001).

[23] K.N. Nigussa, K.L. Nielsen, Ø. Borck, and J.A. Støvneng, *Adsorption of hydrogen, chlorine, and sulfur atoms on α-Cr_2O_3(0001) surfaces: A Density Functional Theory investigation*, submitted to *Corrosion Science*.

[24] A. Züttel, Mater. today **6**, 24 (2003).

[25] B.L. Yang and H.H. Kung, Ind. Eng. Chem. Res. **33**, 1090 (1994).

[26] http://dcwww.fysik.dtu.dk/campos/Dacapo.

[27] D. Vanderbilt, Phys. Rev. B **41**, 11 (1990).

[28] J.P. Perdew, J.A. Chevary, S.H. Vosko, K.A. Jackson, M.R. Pederson, D.J. Singh, and C. Fiolhais, Phys. Rev. B **46**, 6671 (1992).

[29] H.J. Monkhorst and J.D. Pack, Phys. Rev. B **13**, 12 (1976).

[30] J.A. White, D.M. Bird, M.C. Payne, and I. Stich, Phys. Rev. Lett. **73**, 1404 (1994).

[31] H. Jónsson, G. Mills, and K.W. Jacobsen, in : B.J. Berne, G. Ciccotti, and D.F. Coker, *Classical and Quantum Dynamics in Condensed Phase Simulations* (World Scientific, Singapore, 1998).

[32] G. Henkelman and H. Jónsson, J. Chem. Phys. **113**, 9978 (2000).

[33] R.F.W. Bader, *Atoms in Molecules. A Quantum Theory* (Oxford, Clarendon, 1990).

[34] G. Henkelman, A. Arnaldsson and H. Jónsson, Comput. Mater. Sci. **36**, 254 (2006).

[35] E. Sanville, S.D. Kenny, R. Smith, and G. Henkelman, J. Comp. Chem. **28**, 899 (2007).

[36] https://wiki.fysik.dtu.dk/ase.

[37] R.L. Park and M.G. Legally, *Experimental Physics, Solid State Physics, Surfaces* (Vol. 22, Academic Press. Inc., Orlando, Florida, 1985).

[38] J.M. Chase, textitNIST-JANAF Thermodynamical Tables (Hemisphere, New York, 1998).

[39] K.N. Nigussa, K.L. Nielsen, Ø. Borck, and J.A. Støvneng, *Adsorption of H_2, Cl_2, and HCl molecules on α-Cr_2O_3(0001) surfaces: A Density Functional Theory investigation*, submitted to *Journal of Chemical Physics*.

[40] P. Abufager, P. Lustemberg, C. Crespos, and H. Busnengo, Langmuir **24**, 14022 (2008).

[41] D.R. Alfonso, Surf. Sci. **602**, 2758 (2008).

[42] G.B. Fisher, Surf. Sci. **87**, 215 (1979).

[43] R.J. Koestner, M. Salmeron, E.B. Kollin, and J.L. Gland, Surf. Sci. **172**, 668 (1986).

[44] A.J. Leavitt and T.P. Beebe, Surf. Sci. **314**, 23 (1994).

[45] D.E. Jiang and E.A. Carter, Surf. Sci. **583**, 60 (2005).

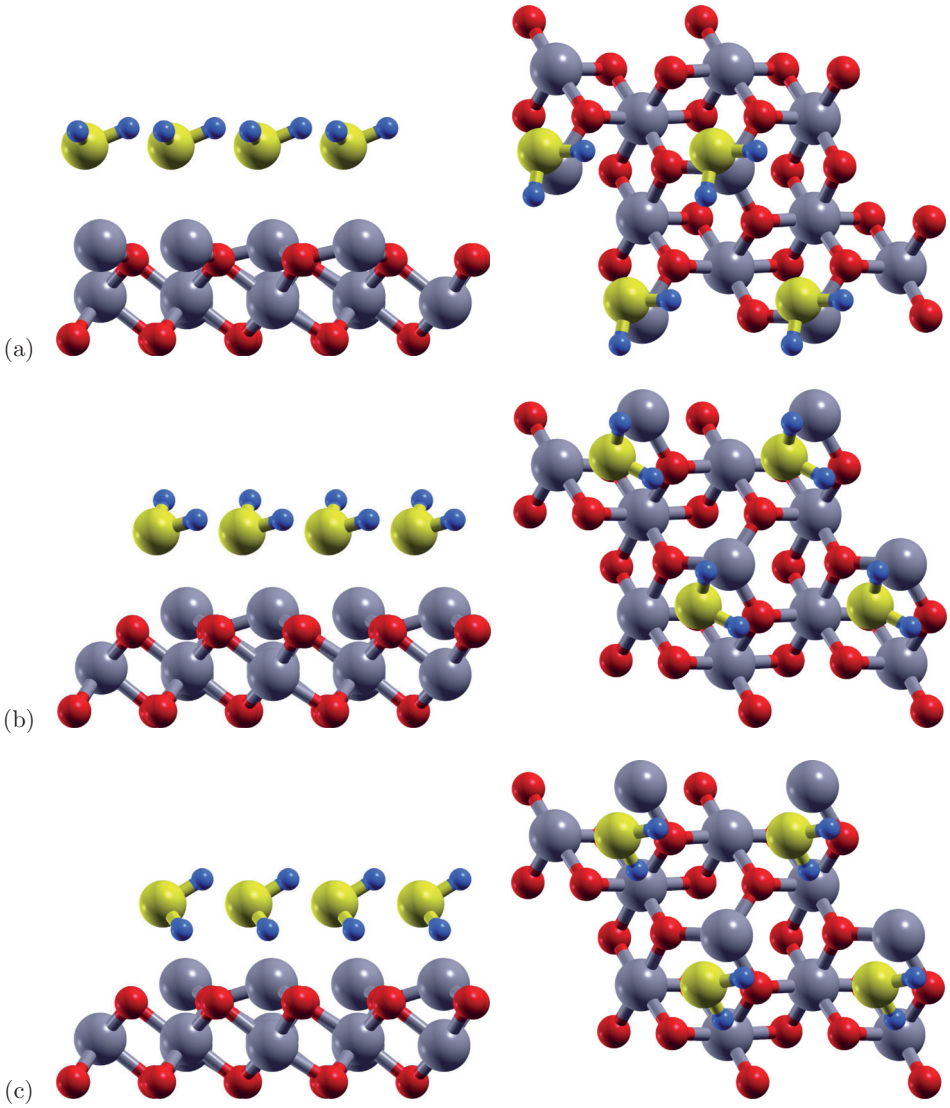

FIG. 1: Molecular adsorption of H_2S on surface **A** at 1 ML coverage. (a) S on top of Cr, E_{ads} = 0.22 eV, T_d = 77 K; (b) S in hollow fcc, E_{ads} = 0.28 eV, T_d = 98 K, dihedral O-Cr-S-H = 110°; (c) S in hollow fcc, E_{ads} = 0.37 eV, T_d = 130 K, dihedral O-Cr-S-H = 163°. (c) is obtained from (b) by a rotation around the Cr-S bond. Colors (size, grayscale): Cr - gray (large, medium gray), O - red (medium, dark gray), S - yellow (large, light gray), H - blue (small, medium gray). E_{ads} and T_d are related via Eqn. (2).

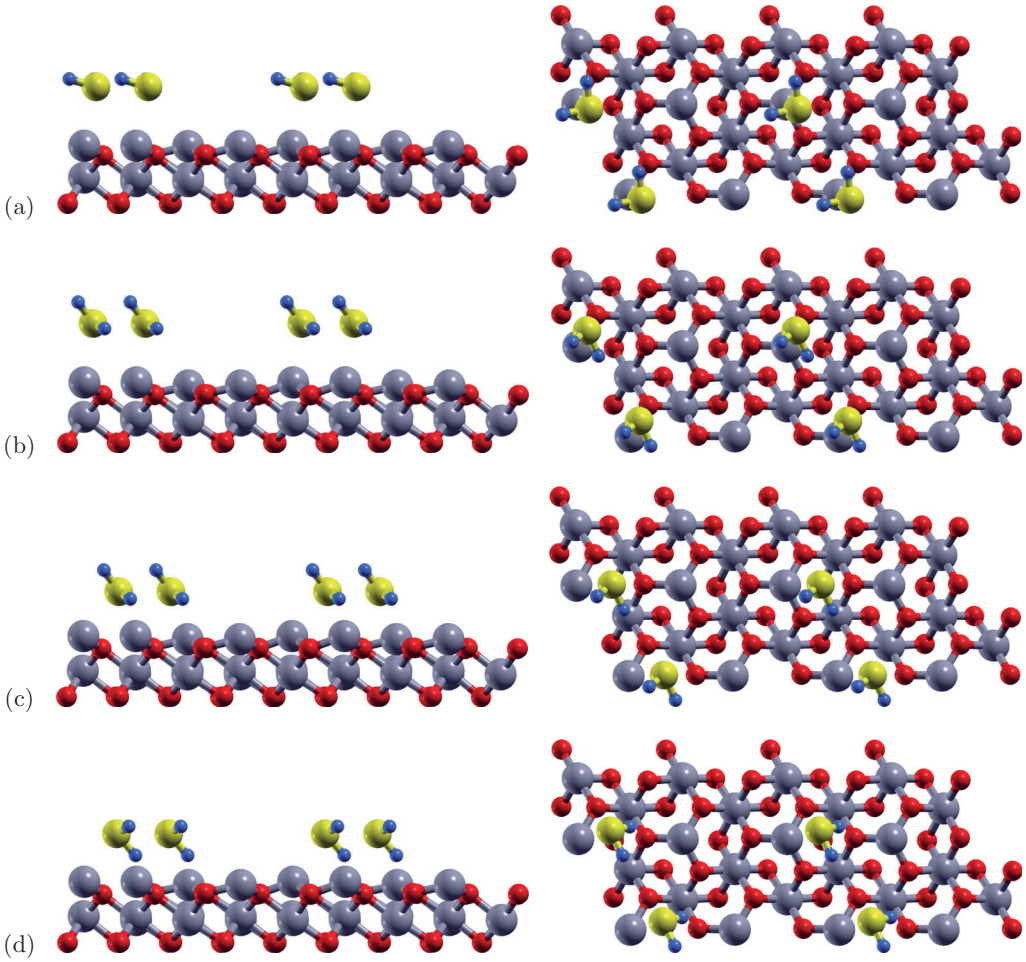

FIG. 2: Molecular adsorption of H_2S on surface **A** at 0.5 ML coverage. (a) S on top of Cr, E_{ads} = 0.24 eV, T_d = 84 K; (b) S in bridge site, E_{ads} = 0.32 eV, T_d = 112 K; (c) S in hollow fcc, E_{ads} = 0.52 eV, T_d = 183 K. (d) S in hollow fcc, E_{ads} = 0.62 eV, T_d = 218 K. Colors (size, grayscale): Cr - gray (large, medium gray), O - red (medium, dark gray), S - yellow (large, light gray), H - blue (small, medium gray). E_{ads} and T_d are related via Eqn. (2).

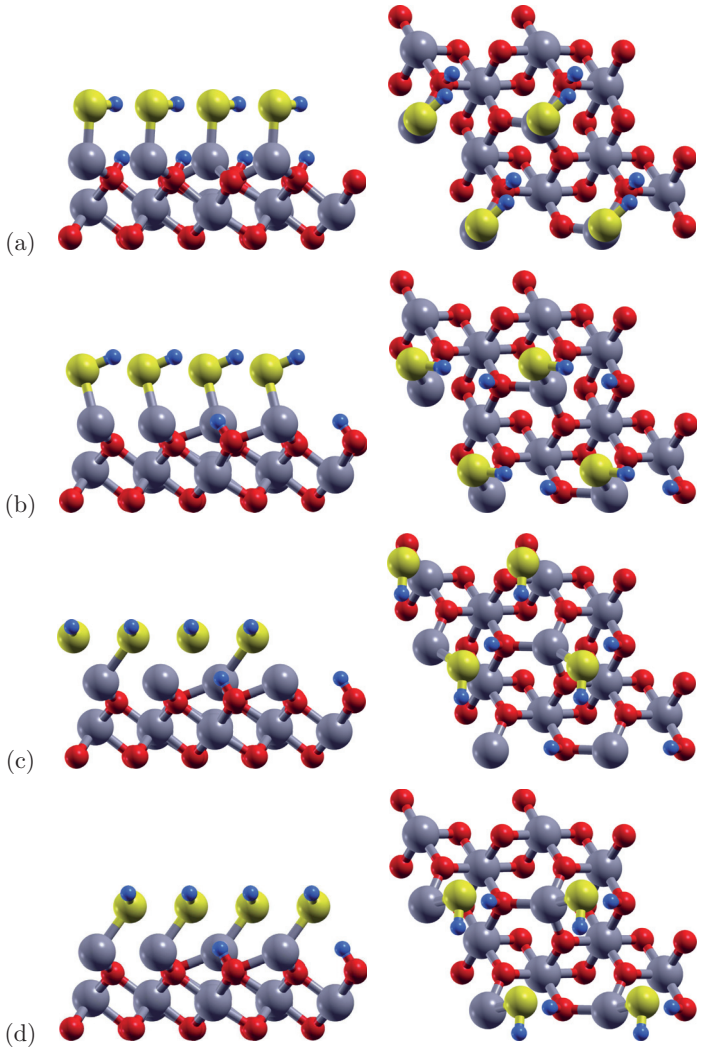

FIG. 3: Partly dissociative adsorption of H_2S, as H and HS subunits, on surface **A** at 1 ML coverage. (a) S on top of Cr, S-H towards O-H, $E_{ads} = 0.54$ eV, $T_d = 190$ K; (b) S above Cr-O bridge, S-H away from O-H, $E_{ads} = 0.57$ eV, $T_d = 200$ K; (c) S above Cr-Cr bridge, S-H orthogonal to O-H, $E_{ads} = 0.89$ eV, $T_d = 312$ K. (d) S in hollow fcc, S-H orthogonal to O-H, $E_{ads} = 0.90$ eV, $T_d = 316$ K. Colors (size, grayscale): Cr - gray (large, medium gray), O - red (medium, dark gray), S - yellow (large, light gray), H - blue (small, medium gray). E_{ads} and T_d are related via Eqn. (2).

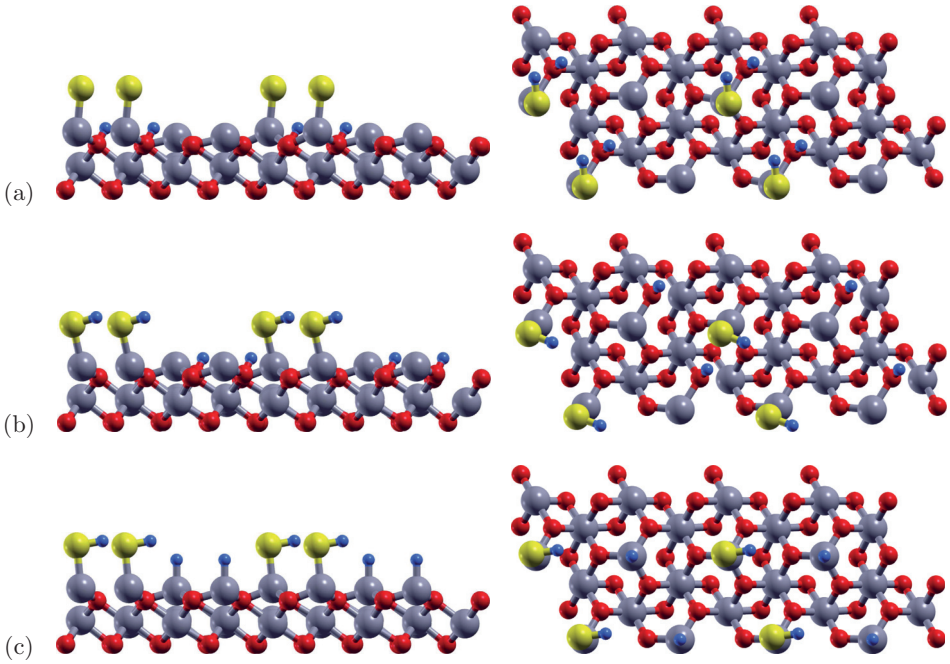

FIG. 4: Partly dissociative adsorption of H_2S, as H and HS subunits, on surface **A** at 0.5 ML coverage. (a) S on top of Cr, H bonded to O, $E_{ads} = 0.66$ eV, $T_d = 232$ K; (b) S above Cr-O bridge, H bonded to O, $E_{ads} = 0.67$ eV, $T_d = 235$ K; (c) S on top of Cr, H bonded to Cr, $E_{ads} = 0.91$ eV, $T_d = 319$ K. Colors (size, grayscale): Cr - gray (large, medium gray), O - red (medium, dark gray), S - yellow (large, light gray), H - blue (small, medium gray). E_{ads} and T_d are related via Eqn. (2).

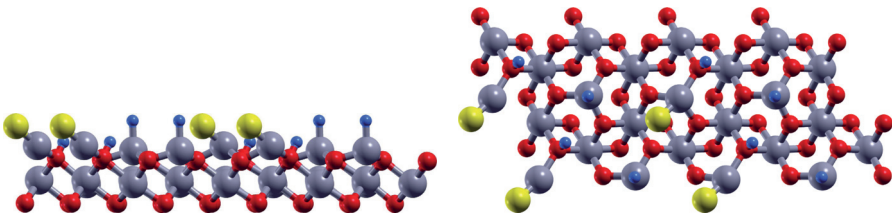

FIG. 5: Fully dissociative adsorption of H_2S, as H, H, and S subunits, on surface **A** at 0.5 ML coverage. S in hollow fcc site, one H bonded to Cr, one H bonded to O, $E_{ads} = 0.56$ eV, $T_d = 197$ K. Colors (size, grayscale): Cr - gray (large, medium gray), O - red (medium, dark gray), S - yellow (large, light gray), H - blue (small, medium gray). E_{ads} and T_d are related via Eqn. (2).

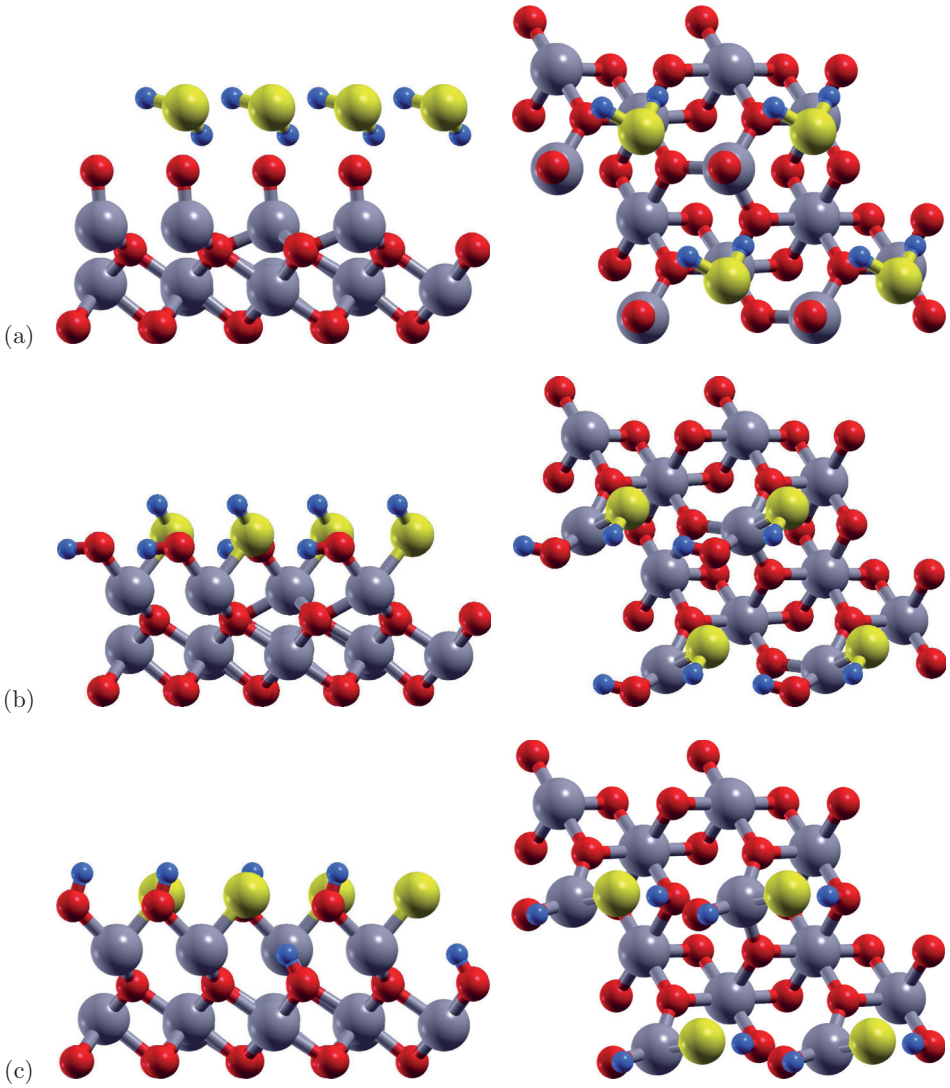

FIG. 6: Adsorption of H_2S on surface **B** at 1 ML coverage. (a) Molecular adsorption, with molecule in 3-fold hollow site between the Cr=O groups, E_{ads} = 0.19 eV, T_d = 67 K. (b) Partly dissociative adsorption as H and HS, with H bonded to O and HS bonded to Cr of the Cr=O group, E_{ads} = -0.12 eV. (c) Fully dissociative adsorption as H, H, and S, with S bonded to Cr, one H bonded to O of the Cr=O group, and one H bonded to a subsurface O, E_{ads} = -0.37 eV. Colors (size, grayscale): Cr - gray (large, medium gray), O - red (medium, dark gray), S - yellow (large, light gray), H - blue (small, medium gray). E_{ads} and T_d are related via Eqn. (2).

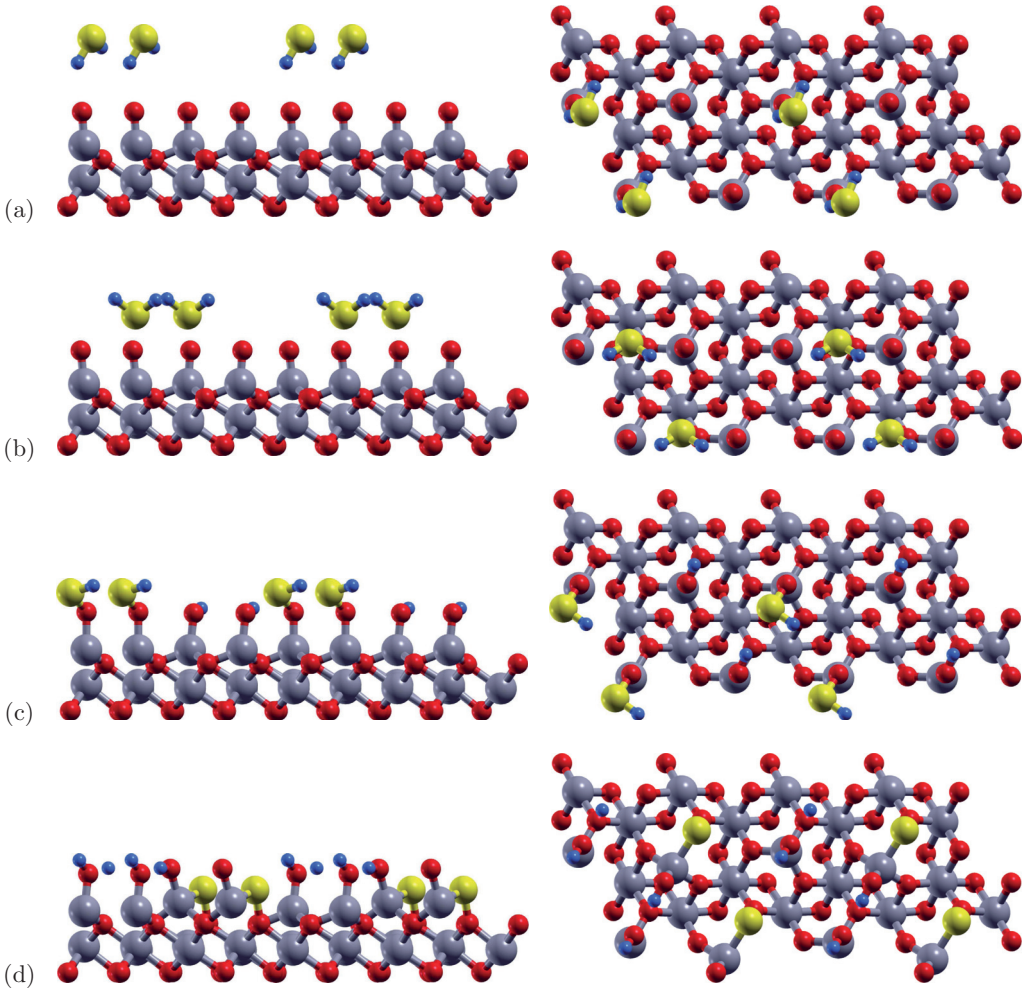

FIG. 7: Adsorption of H_2S on surface **B** at 0.5 ML coverage. (a) Molecular adsorption, with molecule above Cr=O group, $E_{ads} = 0.24$ eV, $T_d = 84$ K. (b) Molecular adsorption, with molecule in bridging position between two Cr=O groups, $E_{ads} = 0.26$ eV, $T_d = 91$ K. (c) Partly dissociative adsorption as H and HS, with H and HS bonded to the O atom of separate Cr=O groups, $E_{ads} = 0.34$ eV, $T_d = 119$ K. (d) Fully dissociative adsorption as H, H, and S, with S in a bridging position between a surface Cr atom and a subsurface O atom, and with the two H atoms bonded to the O atom of separate Cr=O groups, $E_{ads} = 0.32$ eV, $T_d = 112$ K. Colors (size, grayscale): Cr - gray (large, medium gray), O - red (medium, dark gray), S - yellow (large, light gray), H - blue (small, medium gray). E_{ads} and T_d are related via Eqn. (2).

TABLE II: Summary of surface reactions modeled with nudged elastic band (NEB) calculations. 8A/B: Molecular reorientation at 0.5 ML on surface **A**/**B**. 9A/B: Partial dissociation at 1.0 ML on surface **A**/**B**. 10A/B: Full dissociation at 0.5 ML on surface **A**/**B**. E: energy (eV) relative to separate reactants, H_2S molecule and clean surface. E_a: activation energy (eV).

Reaction	Coverage	State	Adsorbate(s)	Figure	Relative E	E_a
8**A**	0.5	IS	H_2S	2a	−0.24	
		TS		8A	−0.22	0.02
		FS	H_2S	2c	−0.52	
8**B**	0.5	IS	H_2S	7a	−0.24	
		TS		8B	−0.01	0.23
		FS	H_2S	7b	−0.26	
9**A**	1.0	IS	H_2S	1c	−0.37	
		TS		9A	0.28	0.65
		FS	H, HS	3d	−0.90	
9**B**	1.0	IS	H_2S	6a	−0.19	
		TS		9B	0.82	1.01
		FS	H, HS	6b	0.12	
10**A**	0.5	IS	H_2S	2d	−0.62	
		TS		10A	−0.22	0.45
		IS	H, HS	4c	−0.91	
		TS			−0.39	0.52
		FS	H, H, S	5	−0.56	
10**B**	0.5	IS	H_2S	7b	−0.26	
		TS		10B	0.11	0.37
		FS	H, H, S	7d	−0.32	

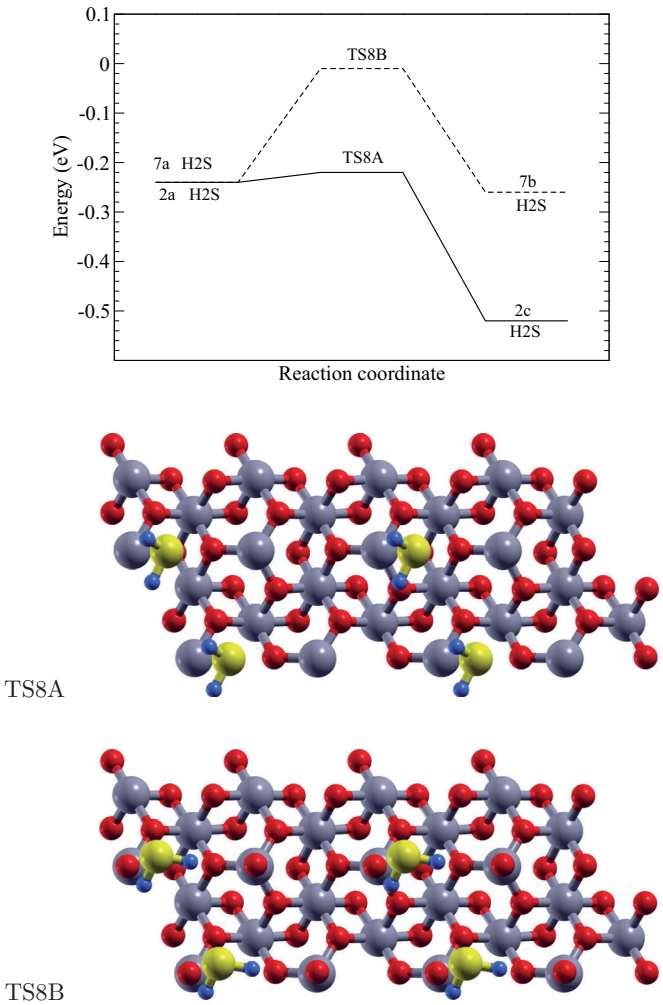

FIG. 8: Upper figure: Stationary points on the NEB reaction paths for molecular reorientation of H_2S on surface **A** (solid curve) and surface **B** (dashed curve) at 0.5 ML adsorbate coverage. Text labels indicate adsorbate configuration (H2S) and corresponding geometry figures for initial (IS) and final states (FS). TS8A: Approximate transition state, surface **A**. TS8B: Approximate transition state, surface **B**. Colors (size, grayscale): Cr - gray (large, medium gray), O - red (medium, dark gray), S - yellow (large, light gray), H - blue (small, medium gray).

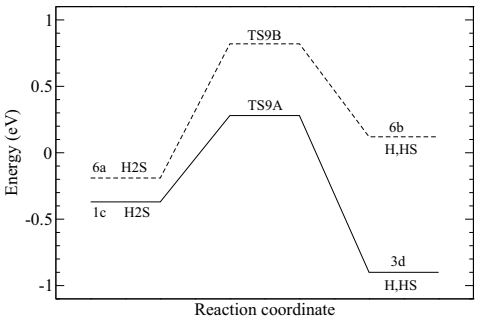

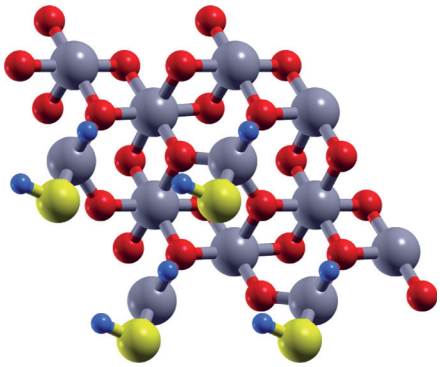

TS9A

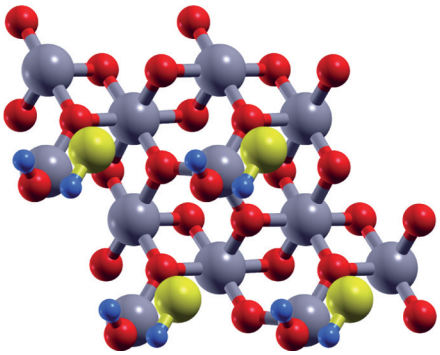

TS9B

FIG. 9: Upper figure: Stationary points on the NEB reaction paths for partly dissociative adsorption as H and HS subunits on surface **A** (solid curve) and surface **B** (dashed curve) at 1.0 ML adsorbate coverage. Text labels indicate adsorbate configuration (H2S or H,HS) and corresponding geometry figures for initial (IS) and final states (FS). TS9A: Approximate transition state, surface **A**. TS9B: Approximate transition state, surface **B**. Colors (size, grayscale): Cr - gray (large, medium gray), O - red (medium, dark gray), S - yellow (large, light gray), H - blue (small, medium gray).

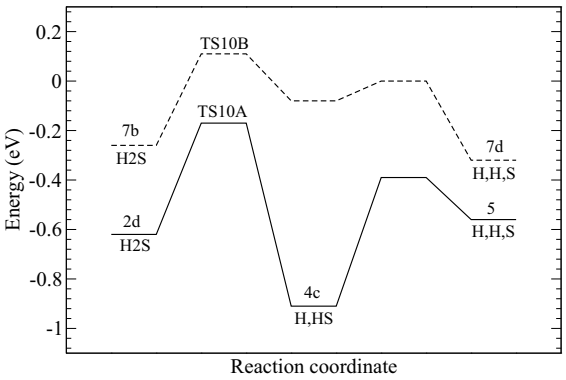

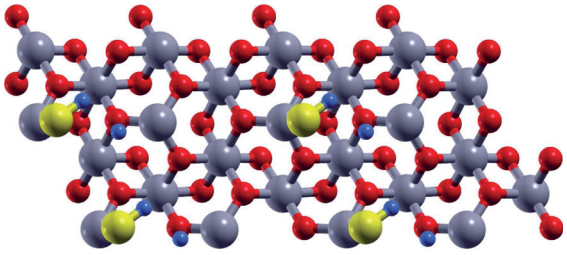

TS10A

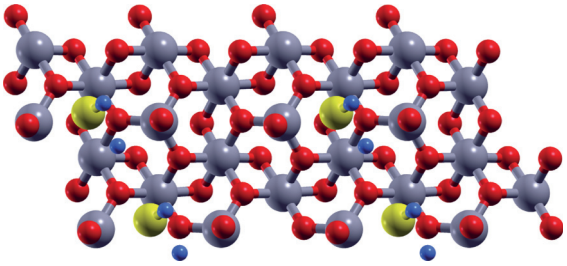

TS10B

FIG. 10: Upper figure: Stationary points on the NEB reaction paths for fully dissociative adsorption as H, H, and HS subunits on surface **A** (solid curve) and surface **B** (dashed curve) at 0.5 ML adsorbate coverage. Text labels indicate adsorbate configuration (H2S, H,HS, or H,H,S) and corresponding geometry figures for initial (IS), intermediate (IS), and final states (FS). TS10A: Approximate transition state, surface **A**. TS10B: Approximate transition state, surface **B**. Colors (size, grayscale): Cr - gray (large, medium gray), O - red (medium, dark gray), S - yellow (large, light gray), H - blue (small, medium gray).

PAPER IV

Oxidation of pure and potassium-doped NiTi shape memory surface: A density functional theory investigation

Physical Review B **82**, 245401 (2010)

PHYSICAL REVIEW B **82**, 245401 (2010)

Oxidation of pure and potassium-doped NiTi shape memory surface: A density functional theory investigation

K. N. Nigussa and J. A. Støvneng*
Department of Physics, NTNU, N-7491 Trondheim, Norway
(Received 2 July 2010; revised manuscript received 11 October 2010; published 1 December 2010)

The oxidation of Ti-terminated NiTi surfaces is investigated with density functional theory. The surfaces considered are (001) and (110) of the austenite phase (B2) and (010) of the martensite phase (B19′). The favored adsorption sites for atomic oxygen are fourfold hollow on B2 (001), and twofold bridged between two surface Ti atoms on B2 (110) and B19′ (010). Adsorption of one oxygen molecule per surface Ti atom results in the formation of a rutilelike protective layer of TiO_2. The oxidation results in outward and inward movement of surface Ti and Ni atoms, respectively, signaling depletion of Ni atoms from the surface region. Substitution of Ni by K near the surface is found to enhance the formation of TiO_2 at the expense of TiO, and increase the stability and facilitate the growth of thicker layers of titanium oxides on the NiTi surfaces. This is of importance for the biofunctionality of the alloy.

DOI: 10.1103/PhysRevB.82.245401 PACS number(s): 73.20.At, 68.43.Fg

I. INTRODUCTION

NiTi alloy with equiatomic composition (Ti-50 at. % Ni) is known to be a shape memory material.[1,2] By application of force or temperature, it undergoes a change in structure from the parent austenite phase (B2) to the martensite phase (B19′) or vice versa.[2] If an impact is applied and released in one of the phases, the original shape would be recovered in the other phase. The intermetallic composition is also being tailored for various purposes by varying the Ni content in the binary alloy or making a ternary alloy by replacing some of the Ni atoms with other transition metals.[1,3] However, this will typically lead to significant loss of the initial shape memory property. The alloy has also been confirmed to be biocompatible with body tissue, and as a consequence it is being used in various medical applications including dentistry, orthopaedics, and vascular surgery.[1,4,5]

The best biofunctionality of the NiTi alloy is achieved when the presence of Ni atoms at the surface is minimized. This follows from numerous reports showing that high amounts of Ni atoms at the surface could result in a leakage to the body and cause hazards.[6,7] Appropriate surface treatment or coating is widely seen as the best remedy to this problem. Titanium oxides including TiO and TiO_2 are in general considered to offer good chemical stability and biocompatibility.[8–10] It is noted that TiO_2 is the most stable form and TiO is a transient phase to TiO_2. Under ultrahigh-vacuum conditions, TiO_2 is found to dominate at low temperatures and TiO is found to dominate at high temperatures.[8] Under high-pressure conditions, TiO dominates at low temperatures and TiO_2 dominates at high temperatures.[9,10] Several studies have been devoted to quantitative characterization of surface oxidation, where exposure of the surface to a sufficient amount of oxygen was found to result in the formation of a TiO_2 protective layer.[8,11,12] In addition to increasing the corrosion resistance of the NiTi alloy surface,[13] a TiO_2 layer is believed to promote its biofunctionality.[14]

The B2 phase of NiTi has a CsCl type structure and exists at temperatures higher than about 330 K.[15,16] The B2 phase has also been found in several Ti-based alloys[17,18] and even in NiTi-based ternary alloys.[19,20] However, the B19′ phase with monoclinic structure is unique to the NiTi alloys and exists at temperatures lower than about 320 K. The B19′ phase is sensitive to the composition of the alloy, and as a consequence, Ti- and NiTi-based alloys with different composition histories have different martensite transformation processes and martensite start temperatures (M_s).[8,15–17,19–21] The (near) equiatomic NiTi alloy attracts attention because it undergoes the structural transformation from B2 to B19′ in just one step (i.e., with no other intermediate structure in between).[1,22] Increasing the Ni content or alloying with a third transition metal by replacing some of the Ni atoms, extends the number of steps to at least two, with an intermediate structure of rhombohedral *R* (Refs. 20 and 21) or orthorhombic (B19),[22] provided that the amount of Ni replacement is significant. When the amount of Ni replacement is small, the transformation occurs in just one step where the M_s temperature decreases slightly below 320 K, depending on the type of added transition metal.[23] However, it is not clear what health impact these transition metals have when used in alloys in medical implants. Alkali metals, typically Na and K, when present in small amounts, are known to be harmless for the body. They have been found to promote oxidation of semiconductor surfaces.[24] A recent experimental study[8] showed that the presence of a thin layer of K on the NiTi surface enhances the oxidation of surface Ti atoms to TiO_2.

In addition to the many experimental efforts carried out to characterize the oxide growth on NiTi, *ab initio* atomic level investigations have recently also been reported.[11,25,26] In the present work, we use density functional theory (DFT) to address the oxidation of selected surfaces of NiTi in the B2 and B19′ phases. On the basis of both experimental and theoretical reports, we focus on the (110) and (001) surfaces of B2 and the (010) surface of B19′. Coverages ranging from 0.5 to 2.0 oxygen atoms per surface Ti atom are explored, resulting in various TiO and TiO_2 surface layers that are conveniently compared with, and categorized in terms of, the corresponding clean titanium oxide surfaces. The influence of

exposing the NiTi surfaces to potassium is addressed by replacing near surface Ni atoms with K.

The paper is organized as follows: in Sec. II, details of the computational method are presented. In Sec. III, we report the results of our calculations. We close the paper with a discussion in Sec. IV and a conclusion in Sec. V.

II. COMPUTATIONAL METHODS

All calculations presented are based on DFT. The Kohn-Sham equations are solved within the generalized gradient approximation, using Vosko, Wilk, and Nusair's parametrization (VWN, Ref. 27) of the correlation energy within the local-density approximation (LDA), contribution and the PW91 (Ref. 28) gradient corrections to the exchange and correlation energy.

A slab type model with five layers of NiTi is used for the surface calculations. Three layers are constrained to the bulk geometry while two layers are allowed to relax together with the adsorbate (O or O_2). In most of our calculations, an adsorbate coverage of one or two oxygen atoms per surface Ti atom is being used. We refer to this as 1 ML O and 1 ML O_2 (ML=monolayer), respectively. In these calculations, prior to oxidation, the undoped (1×1) supercell contains five Ti and five Ni atoms. The influence of K (K doping) is modeled by replacing one Ni atom near the surface by K, i.e., the (1×1) supercell contains one K, five Ti, and four Ni atoms. A lower coverage of 0.5 O per surface Ti requires a (2×1) supercell with ten Ti and ten Ni atoms (undoped surface). The influence of K doping is also in this case modeled by replacing one near surface Ni by K, i.e., the supercell prior to oxygen adsorption consists of one K, ten Ti, and nine Ni atoms.

Calculations with (1×1) supercells are performed with the ADF/BAND program package.[29] The electronic wave functions are constructed as linear combinations of atomic orbitals.[30] The wave functions of the core electrons (O: 1*s*; K, Ti, Ni: 1*s*, 2*s*, 2*p*) are expressed in terms of Herman-Skillman-type numerical atomic orbitals (NAOs) whereas those of the valence electrons are described by one NAO plus two Slater-type orbitals, in what is called triple ζ quality. To allow for angular flexibility, two shells of higher angular momentum have been included in the basis set, i.e., triple ζ plus two polarization functions. Relativistic effects in a scalar form[31] have been included in the kinetic energy of the electrons. This typically lowers the energy by about 1 eV pr unit cell. Consequently, the calculated adsorption energies are not much affected (less than 0.1 eV) by including relativistic effects. The *k*-space integrations employ a quadratic tetrahedron method,[32] with the KSPACE parameter equal to 5. Depending on the degree of symmetry, the number of symmetry unique *k* points typically ranges from 15 to 34 in the slab calculations.[33]

Isolated adsorbates, O (atomic oxygen) and O_2 (molecular oxygen), were optimized in a cubic structure with lattice constant 15 Å. This is sufficient to avoid adsorbate-adsorbate interactions prior to adsorption. For both O and O_2, a triplet ground state is found, with a preference over the lowest singlet state of 1.52 eV and 1.16 eV, respectively, in reasonable agreement with experimental and theoretical values in the literature.[34,35] The reaction $O+O\rightarrow O_2$ is found to be exothermic by 6.83 eV with the chosen method. Except for the isolated adsorbates, all calculations presented in Sec. III are spin restricted (i.e., spin unpolarized). Test calculations allowing spin polarization indeed predict net atomic magnetization in some of the slab models, and typically, the surface Ti atoms are predicted to have the largest spin values, up to 1.4 μ_B. However, the energy differences between the spin restricted and spin unrestricted calculations are small (less than 0.5 eV), and will not affect the trends in our calculations. The relaxed geometries are also little influenced by this choice. Therefore, only spin restricted calculations have been included. For all the relevant bulk systems (B2 and B19′ NiTi and hcp Ti), the ground states possess no spin polarization.

With (2×1) supercells, i.e., for an adsorbate coverage of 0.5 oxygen atom per surface Ti, the computational time turned out to become prohibitively long with the ADF/BAND program. For these systems, the plane-wave-based DFT program DACAPO (Ref. 36) was used. In DACAPO, Vanderbilt[37] ultrasoft pseudopotentials are implemented, and relativistic effects are not taken into account. The comments above, concerning spin restricted vs spin unrestricted calculations, are equally valid when the DACAPO program is used for these systems, i.e., energy differences after geometry relaxation with and without allowance for spin polarization are below 0.5 eV, and geometry differences are negligible. In our DACAPO calculations, the triplet ground state of O and O_2 are favored by 1.96 eV and 1.10 eV, respectively, over the lowest singlet state, and the $O+O\rightarrow O_2$ reaction is exothermic by 5.59 eV.

In DACAPO, the system is always periodic in all three dimensions, so for the slab calculations, a vacuum layer of 10 Å is introduced to minimize artificial interactions between the slabs.[38] A *k*-point mesh of $4\times4\times1$ is used for the slab calculations. For the bulk crystals, a *k*-point mesh of $4\times4\times4$ is used. The *k* points are chosen based on the Monkhorst-Pack scheme.[39] The electron wave functions are expanded in plane waves with a cut-off energy of 400 eV.

Clearly, the adsorption energies calculated for (2×1) supercells with DACAPO cannot be directly compared with those calculated for (1×1) supercells with ADF/BAND. However, the DACAPO results do indicate certain trends concerning low (submonolayer) oxygen coverage.

We define the adsorption energy as

$$E_{ads} = -(E_{S+O} - E_S - E_O), \tag{1}$$

for adsorption of a single oxygen atom. The coverage is then 0.5 and 1.0 oxygen atoms per surface Ti, i.e., 0.5 and 1.0 ML O, respectively, for the (2×1) and (1×1) supercells. The adsorption energy is defined as

$$E_{ads} = -(E_{S+O_2} - E_S - E_{O_2}), \tag{2}$$

for adsorption of an oxygen molecule. This corresponds to a coverage of 1.0 and 2.0 oxygen atoms per surface Ti, i.e., 0.5 and 1.0 ML O_2, respectively, for the (2×1) and (1×1) supercells. Here E_{S+O}, E_{S+O_2}, E_S, E_O, and E_{O_2} are total energies,

TABLE I. Adsorption of oxygen on the B2 phase of Ti-terminated NiTi. In each case, one O atom or one O_2 molecule is adsorbed. $z_{Ti}-z_{Ni}$ is the (vertical) distance between the surface Ti layer and the first Ni layer below, and $\Delta z_{Ti\text{-}Ni}$ is the change in this distance upon oxidation of the surface, (both measured in angstrom). ΔQ is the total (Mulliken) charge gained by the adsorbate (number of gained electrons per O atom or O_2 molecule). E_{ads} is the adsorption energy per O atom or O_2 molecule (in electron volt).

Surface, supercell	Figure	Adsorbate	$z_{Ti}-z_{Ni}$	$\Delta z_{Ti\text{-}Ni}$	E_{ads}	ΔQ
(001), (1×1)	1(a) and 1(b)	O	1.89	0.39	8.87	0.88
(001), (1×1)	3(a) and 3(b)	O_2	2.52	1.02	8.00	1.30
(001), (1×1)	3(c) and 3(d)	O_2	2.85	1.35	8.17	1.42
(001), (2×1)		O	1.92	0.62	8.48	
(001), (2×1)		O_2	1.80	0.50	10.76	
(110), (1×1)	1(c) and 1(d)	O	0.62	0.48	8.30	0.70
(110), (1×1)	3(e) and 3(f)	O_2	1.12	0.98	7.52	1.41
(110), (1×1)	3(g) and 3(h)	O_2	0.90	0.76	6.76	1.31
(110), (2×1)		O	0.54	0.23	7.64	
(110), (2×1)		O_2	0.63	0.32	9.56	

per supercell, of surface with one adsorbed oxygen atom, surface with two adsorbed oxygen atoms, clean surface, and isolated atomic and molecular oxygen, respectively. A positive E_{ads} implies an exothermic reaction. The reader who prefers to refer E_{ads} to molecular oxygen also in the case of adsorption of a single oxygen atom, should subtract half of the calculated dissociation energy for molecular oxygen, 3.42 eV [2.80 eV for the DACAPO calculations with (2×1) supercells], from the energy values in Tables I–IV.

In ADF/BAND, atomic charges are calculated based on a Mulliken analysis. In addition, the electronic structure is discussed in terms of the partial density of states (PDOS) on Ti, O, and K atoms, at or near the surface. Whenever the adsorbate is O_2, the PDOS for oxygen represents a sum of the PDOS of the two O atoms in the supercell.

In the discussion of the surface structures that result from adsorption of oxygen on the various Ti-terminated NiTi surfaces, we have found it convenient to make comparison with TiO (rocksalt structure) and TiO_2 (rutile structure), and in particular with selected low-index surfaces of these oxides. The oxide layer grown on the three different NiTi surfaces that we have investigated, has a geometric and electronic structure that compares well with one particular *as cleaved* single layer of TiO or TiO_2. Hence, we categorize the grown oxides on NiTi accordingly. We justify this categorization by comparing the surface Ti and O PDOS of the grown oxide on NiTi with the Ti and O PDOS of the as cleaved single layers of TiO or TiO_2. Since rutile TiO_2 has a unit cell with two Ti and four O atoms, a "single layer of TiO_2" is a slab with a thickness given by the unit cell. Hence, the supercell of this slab contains two Ti and four O atoms. The Ti PDOS is for the Ti atom with coordination equal to the coordination of the Ti atom in the oxide grown on NiTi. The O PDOS is obtained by summing over the three oxygen atoms that are bonded to the chosen Ti atom, i.e., one of the four O atoms is not included in the PDOS sum.

Finally, in order to assess the calculated adsorption energies, it is of interest to compare oxidation of NiTi with the corresponding adsorption reactions on surfaces of pure Ti (hexagonal close-packed structure). For bulk hcp Ti, we have calculated lattice parameters $a=b=2.93$ Å and $c=4.67$ Å, which are subsequently used for obtaining slab geometries representing the (001) and the (110) surfaces of Ti. Oxide formation on NiTi will be compared with oxygen adsorption on the triangular Ti(001) and the rectangular Ti(110) surfaces.

TABLE II. Adsorption of oxygen on the B2 phase of K-doped Ti-terminated NiTi. In each case, one O atom or one O_2 molecule is adsorbed. $z_{Ti}-z_{Ni}$ is the (vertical) distance between the surface Ti layer and the first Ni layer below, and $\Delta z_{Ti\text{-}Ni}$ is the change in this distance upon oxidation of the surface, (both measured in angstrom). ΔQ is the total (Mulliken) charge gained by the adsorbate (number of gained electrons per O atom or O_2 molecule). E_{ads} is the adsorption energy per O atom or O_2 molecule (in electron volt).

Surface, supercell	Figure	Adsorbate	$z_{Ti}-z_{Ni}$	$\Delta z_{Ti\text{-}Ni}$	E_{ads}	ΔQ
(001), (1×1)	5(a) and 5(b)	O	7.95	−0.15	9.67	0.98
(001), (1×1)	7(a) and 7(b)	O_2	8.55	0.44	9.68	1.47
(110), (1×1)	5(c) and 5(d)	O	2.01	0.27	9.23	0.91
(110), (1×1)	7(c) and 7(d)	O_2	1.99	0.25	10.94	1.75
(110), (2×1)	5(e) and 5(f)	O	0.34	0.16	7.35	
(110), (2×1)	5(g) and 5(h)	O	0.29	0.11	8.99	

TABLE III. Adsorption of oxygen on the B19′ phase of Ti-terminated NiTi. In each case, one O atom or one O_2 molecule is adsorbed. $z_{Ti}-z_{Ni}$ is the (vertical) distance between the surface Ti layer and the first Ni layer below, and $\Delta z_{Ti\text{-}Ni}$ is the change in this distance upon oxidation of the surface, (both measured in angstrom). ΔQ is the total (Mulliken) charge gained by the adsorbate (number of gained electrons per O atom or O_2 molecule). E_{ads} is the adsorption energy per O atom or O_2 molecule (in electron volt).

Surface, supercell	Figure	Adsorbate	$z_{Ti}-z_{Ni}$	$\Delta z_{Ti\text{-}Ni}$	E_{ads}	ΔQ
(010), (1×1)	9(a) and 9(b)	O	0.95	0.67	8.01	0.65
(010), (1×1)	9(c) and 9(d)	O_2	1.71	1.43	7.49	1.42
(010), (2×1)		O	0.70	0.32	7.54	

III. RESULTS

A. Adsorption of oxygen on the B2 phase of NiTi

1. Bulk B2 NiTi and its low index surfaces

The bulk modulus of the B2 phase of NiTi is estimated from a Birch fit[40] to be 160.7 GPa. This is in good agreement with experimental [140.3 GPa (Ref. 41)] and calculated [157.8 GPa (Ref. 42)] values. The lattice constant is calculated to be 3.02 Å, in good agreement with the experimental value of 3.00 Å.[16]

Cleavage of the crystal along planes that result in (001) and (111) surfaces will inevitably lead to both Ni and Ti terminated surfaces. However, since oxygen preferably reacts with Ti, only the Ti-terminated surfaces are considered here. The as cleaved (110) surface has equal amounts of Ni and Ti atoms in the surface layer. However, upon geometry relaxation, the Ti atoms move outward and the Ni atoms move inward, resulting in an essentially Ti terminated surface. This is consistent with previously reported calculations.[11,25]

For the three Ti terminated surfaces, we find that the (001) surface is 0.35 eV more stable than the (110) surface and 1.64 eV more stable than the (111) surface. These values are based on total energies per supercell (i.e., per Ni_5Ti_5). Since the supercell surface area is smallest for the (001) and largest for the (111) surface, an evaluation of surface energies per unit area reveals the highest stability for the (110) surface and approximately equally stable (001) and (111) surfaces. In this work, we have limited ourselves to investigating oxidation of the (001) and (110) surfaces of the B2 phase. In Sec. II, we discuss the undoped NiTi surfaces. In Sec. III, we study the effects of potassium doping, i.e., substitution of near surface Ni atoms by K.

2. Oxygen adsorption on undoped B2 NiTi (001) and (110)

Both the (001) and the (110) surfaces of B2 NiTi interact strongly with oxygen. The calculated adsorption energies are large (in the range 7–11 eV), both for atomic and molecular oxygen, and both for low and high oxygen coverage (see Table I). These values are comparable to the heat of formation of TiO_2, 9.9 eV.[43]

On the (001) surface, at coverage (up to) one O per surface Ti, i.e., 1 ML O, oxygen adsorbs most favorably at the fourfold hollow site where it is bonded to four Ti atoms [Figs. 1(a) and 1(b)]. The adsorbed oxygen has equal bond distance 2.09 Å to each Ti atom. It is natural to categorize the grown surface layer as TiO(001), and we will call the structure TiO(001)/NiTi(001). A corresponding notation will be used in the following. In Fig. 2, the electronic structure of the oxide layer in TiO(001)/NiTi(001) is compared with a single layer of TiO(001), as cleaved from the bulk TiO crystal. Here, the PDOS is plotted for the Ti and O atoms in the surface layer of TiO(001)/NiTi(001), Fig. 2, (II), as well as for the single layer of TiO(001), Fig. 2, (III). Both the Ti and O PDOS curves are indeed very similar in Fig. 2, (II) and (III). The calculated Mulliken charges on oxygen are also similar, $0.88e$ for TiO(001)/NiTi(001) and $1.01e$ for the single layer of TiO(001).

The adsorption energy of 8.87 eV suggests the formation of strong Ti-O bonds. In comparison, for the adsorption of atomic oxygen in the threefold hollow site on the (001) surface of hcp Ti, we find an adsorption energy of 8.02 eV. In other words, a stronger oxide seems to be formed on the NiTi alloy than on the pure Ti crystal. This difference may be ascribed to weaker bonds between Ti and Ni atoms in the alloy than between Ti atoms in the Ti crystal. It appears that the presence of Ni below the Ti surface stabilizes the grown oxide layer without affecting its electronic structure significantly.

Increasing the coverage of oxygen to 1 ML O_2 leads to the formation of one TiO_2 layer on the parent NiTi(001) substrate. The most stable structures are shown in Figs. 3(a) and 3(b) and Figs. 3(c) and 3(d), for which the adsorption energies are 8.00 and 8.17 eV, respectively. Common to the

TABLE IV. Adsorption of oxygen on the B19′ phase of K-doped Ti-terminated NiTi. In each case, one O atom or one O_2 molecule is adsorbed. $z_{Ti}-z_{Ni}$ is the (vertical) distance between the surface Ti layer and the first Ni layer below, and $\Delta z_{Ti\text{-}Ni}$ is the change in this distance upon oxidation of the surface, (both measured in angstrom). ΔQ is the total (Mulliken) charge gained by the adsorbate (number of gained electrons per O atom or O_2 molecule). E_{ads} is the adsorption energy per O atom or O_2 molecule (in electron volt).

Surface, supercell	Figure	Adsorbate	$z_{Ti}-z_{Ni}$	$\Delta z_{Ti\text{-}Ni}$	E_{ads}	ΔQ
(010), (1×1)	11(a) and 11(b)	O	2.00	0.05	9.00	0.92
(010), (1×1)	11(c) and 11(d)	O_2	2.38	0.42	12.63	1.73

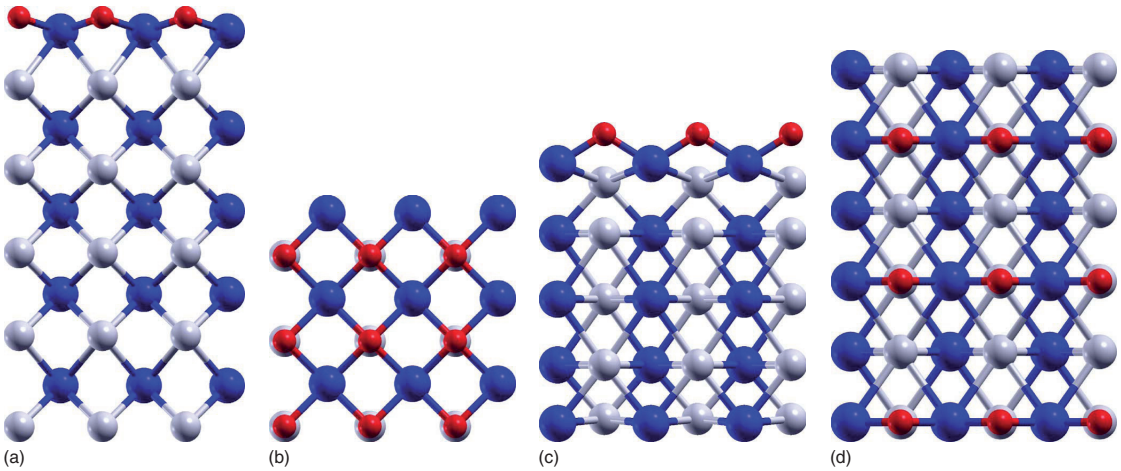

FIG. 1. (Color online) Adsorption of 1 ML O on B2 NiTi; (a) and (b) side and top view, fourfold hollow site on the (001) surface; (c) and (d) side and top view, twofold bridge site on the (110) surface. Colors (size, grayscale): Ti-blue (large gray), O-red (small, gray), Ni-white (large, white).

two geometries is the O atom in the fourfold hollow site. The second O atom is located on top of Ti in Figs. 3(a) and 3(b) whereas in Figs. 3(c) and 3(d) it is in a bridging position between two Ti atoms. In Figs. 3(a) and 3(b), the Ti-O bond lengths are 2.14 Å and 1.61 Å for O in the fourfold hollow site and on top of Ti, respectively. In Figs. 3(c) and 3(d), the Ti-O bond lengths are 2.25 Å and 1.83 Å for O in the fourfold hollow site and in the twofold bridging site, respectively.

Whereas the adsorption of 1 ML O on NiTi(001) clearly suggested a comparison with TiO(001), similar comparisons with specific surfaces of TiO_2 are in general less obvious. However, on the basis of the coordination of the Ti and O atoms involved, the oxide layers formed in Figs. 3(a) and 3(b), and Figs. 3(c) and 3(d), are best categorized as $TiO_2(100)$ and $TiO_2(110)$, respectively. As shown by Perron

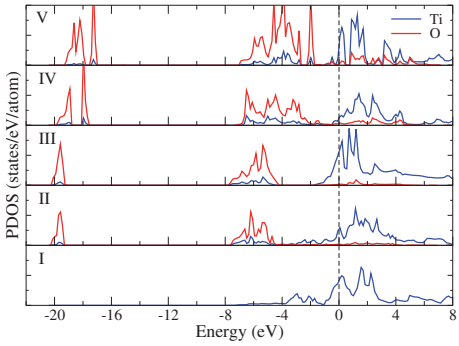

FIG. 2. (Color online) Partial density of states of Ti and O atoms: (I) clean Ti-terminated B2 NiTi(001) surface; (II) I+1 ML O adsorbed [Figs. 1(a) and 1(b)]; (III) one layer of TiO(001); (IV) I+1 ML O_2 adsorbed [Figs. 3(c) and 3(d)]; (V) one layer of $TiO_2(110)$.

et al.,[44] the $TiO_2(110)$ surface contains Ti(5), Ti(6), and bridging O(2) and O(3). Here, Ti(5) means fivefold coordinated Ti, etc. The $TiO_2(100)$ surface contains Ti(5) bonded to bridging O(2) at the surface and subsurface O(3). The surface structures in Figs. 3(a) and 3(b), and Figs. 3(c) and 3(d) have Ti(5) and Ti(6), respectively. Hence, the suggested categorization. In Fig. 2, (IV) and (V), the surface Ti and O PDOS are plotted for $TiO_2(110)/NiTi(001)$, i.e., the structure in Figs. 3(c) and 3(d), and for a single (as cleaved) layer of $TiO_2(110)$, respectively. [Actually, Ti_2O_4, see Sec. II for a description of which Ti and O atoms contribute to the PDOS plotted in Fig. 2, (V).] The comparison is perhaps not quite as evident as in the case of TiO(001)/NiTi(001). However, both for O and Ti, the PDOS curves reveal similar profiles, in particular below the Fermi level. A comparison between the structure in Figs. 3(a) and 3(b) and a single layer of $TiO_2(100)$ (not included here) reveals corresponding similarities in the PDOS curves.

Note the reduced value of the surface Ti PDOS at the Fermi level as a result of the oxidation, i.e., going from clean B2 (001) NiTi in Fig. 2, (I) via a coverage of 1 ML O in Fig. 2, (II) to a coverage of 1 ML O_2 in Fig. 2, (IV), where a layer of TiO_2 has formed on the surface. This is a general trend in all our calculations, and a clear signature of the reduced metallic character of the surface, as one would expect. A similar effect was pointed out by Nolan *et al.*[25]

As with atomic oxygen, we find significantly higher adsorption energies for dissociative adsorption of molecular oxygen on NiTi(001) than on the (001) surface of Ti. Adsorption of 1 ML O_2 on the Ti(001) surface is exothermic by only 3.37 eV per oxygen molecule. This, again, underscores the catalytic role played by Ni atoms, due to their relative inertness toward oxygen.

On the B2 NiTi(110) surface, at a coverage of one O per surface Ti (1 ML O), oxygen preferably adsorbs in a twofold bridge site between two Ti atoms, as shown in Figs. 1(c) and 1(d).[45] The Ti-O bond distance is 1.84 Å. We categorize the

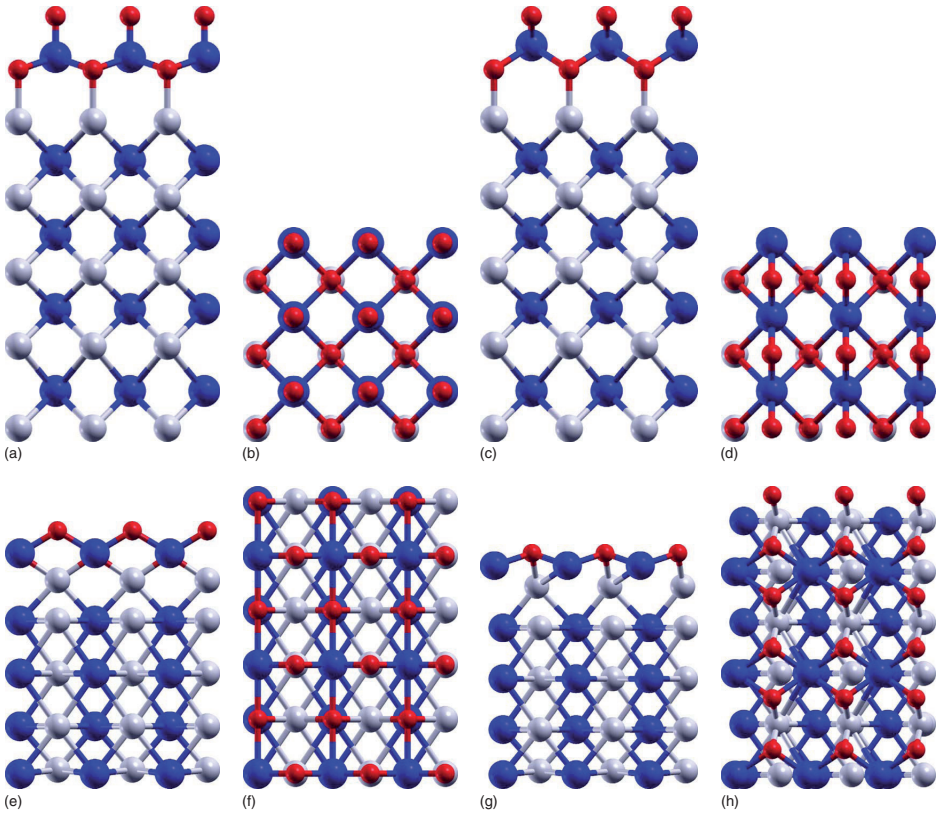

FIG. 3. (Color online) Adsorption of 1 ML O_2 on B2 NiTi; (a) and (b) side and top view, hollow and top sites on the (001) surface; (c), and (d) side and top view, hollow and bridge sites on the (001) surface; (e) and (f) side and top view, bridge and in-plane sites on the (110); (g) and (h) side and top view, bridge and bridge sites on the (110) surface. Colors (size, grayscale): Ti-blue (large, gray), O-red (small, gray), Ni-white (large, white).

grown surface layer as TiO(110). In Fig. 4, (II) and (III), the PDOS of surface Ti and O atoms are plotted for the structure in Figs. 1(c) and 1(d) and a single (as cleaved) layer of TiO(110), respectively. As in the case of NiTi(001) discussed above, the PDOS curves have similar features, with comparable peak profiles, although not as striking as in Fig. 2, (II) and (III). In Figs. 1(c) and 1(d), oxygen has gained a total charge of 0.70*e* from the surface, which is close to the value 0.78*e* in the single layer of TiO(110).

The adsorption energy of atomic oxygen on NiTi(110) is 8.30 eV, which is about 0.6 eV less than for oxygen adsorbed in the fourfold hollow site on NiTi(001). Adsorption of atomic oxygen in a similar bridging site on the (110) surface of Ti is found to be exothermic by 7.84 eV. Hence, the presence of Ni atoms near the NiTi(110) surface has a stabilizing effect on the grown oxide, as found for the NiTi(001) surface.

Increasing the adsorbate coverage to 1 ML O_2 leads to the growth of one TiO_2 layer on the NiTi(110) substrate. The most stable structure that we have found is shown in Figs. 3(e) and 3(f). The adsorption energy is 7.52 eV. In this geometry, all Ti atoms in the grown oxide are fourfold coordinated, with bonds to two bridging surface O atoms (1.81 Å) and two "in-plane" O atoms (2.20 Å). The latter O atoms

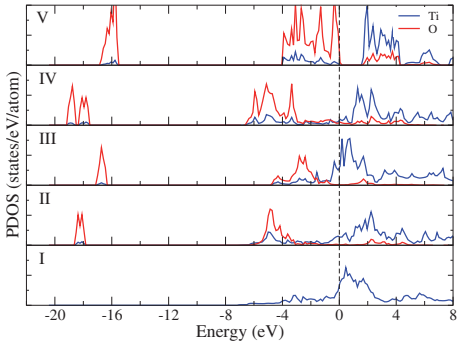

FIG. 4. (Color online) Partial density of states of Ti and O atoms: (I) clean Ti-terminated B2 NiTi(110) surface; (II) I+1 ML O adsorbed [Figs. 1(c) and 1(d)]; (III) one layer of TiO(110); (IV) I+1 ML O_2 adsorbed [Figs. 3(e) and 3(f)]; (V) one layer of TiO_2(001).

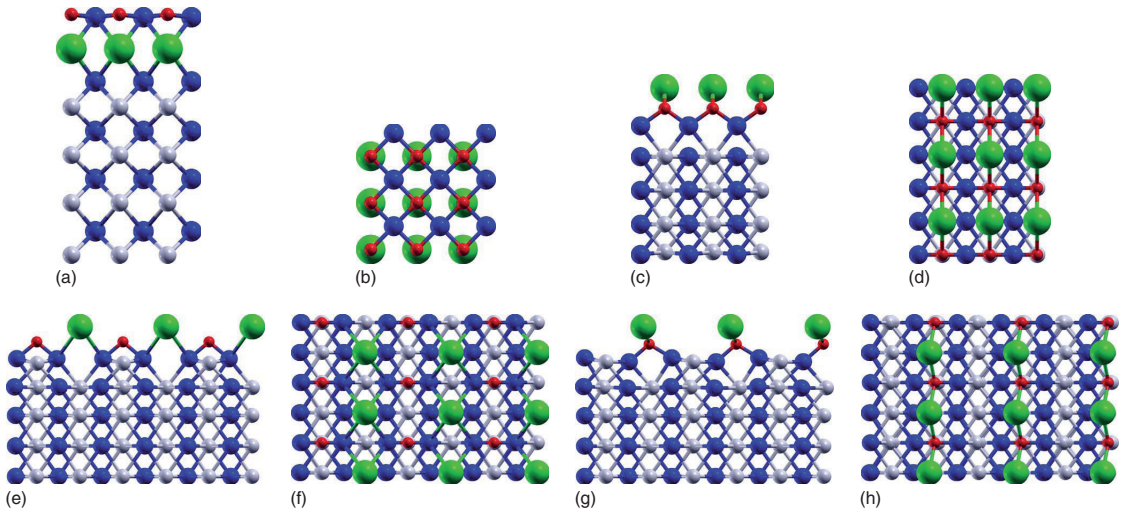

FIG. 5. (Color online) Adsorption on B2 NiTi with K doping; (a) and (b) side and top view, 1 ML O, fourfold hollow site on the (001) surface; (c) and (d) side and top view, 1 ML O , twofold bridge site on the (110) surface; (e) and (f) side and top view, 0.5 ML O, twofold bridge site on the (110) surface (2×1 supercell with only half of Ni in top layer substituted by K; K-O distance is 5.02 Å); (g) and (h) side and top view, 0.5 ML O, twofold bridge site on the (110) surface, (2×1 supercell with only half of Ni in top layer substituted by K; K-O distance is 2.57 Å). Colors (size, grayscale): K-green (huge, light gray), Ti-blue (large, gray), O-red (small, gray), Ni-white (large, white).

are also bonded to Ni (1.88 Å). As shown by Perron *et al.*,[44] the presence of Ti(4) is a signature of $TiO_2(001)$, which leads us to categorize the grown structure as $TiO_2(001)/NiTi(110)$. The calculated oxygen charges are almost identical in the geometry in Figs. 3(e) and 3(f) (0.68*e* and 0.73*e*) and in the single (as cleaved) layer of $TiO_2(001)$ (0.67*e*). In Fig. 4, (IV) and (V), the PDOS of Ti and O are plotted for $TiO_2(001)/NiTi(110)$ [Figs. 3(e) and 3(f)] and a single layer of $TiO_2(001)$, respectively. The oxygen bands below the Fermi level are shifted to lower energies in $TiO_2(001)/NiTi(110)$ compared to the single layer of $TiO_2(001)$. However, both in Fig. 4, (IV) and (V), there are overlapping oxygen bands, both at the lowest energies shown, and for energies a few electron volts below the Fermi level.

Also in this case, the surface Ti PDOS at the Fermi level diminishes upon oxidation, as expected, see Fig. 4, (I), (II), and (IV). However, the effect is less pronounced than for oxidation of the B2 (001) surface (Fig. 2). This is an indication that the coverage of 1 ML O_2 on B2 (001) yields an oxide layer which is more "bulklike" than on the B2 (110) surface. This observation is consistent with the difference in coordination of the Ti atoms in the two oxides grown: On B2 (001), the grown oxide can have either Ti(5) or Ti(6), but on B2 (110), the grown oxide has only Ti(4). The former is closer to the perfect and stoichiometric Ti(6) coordination of bulk TiO_2.

Adsorption of 1 ML O_2 on the Ti(110) surface is exothermic by only 2.60 eV. This is significantly less than for adsorption of 1 ML O, and consistent with the trend observed with the Ti(001) surface.

As expected, in most cases, the adsorption energy increases when the oxygen coverage is reduced to submonolayer values. This can be ascribed to a reduction in repulsive interactions between the adsorbed oxygen atoms. The changes in E_{ads} seem to correlate well with the "oxygen density" on the surface, which decreases in the order O_2 on B2 (001), O_2 on B2 (110), O on B2 (001), and O on B2 (110). The corresponding changes in E_{ads} are 2.59, 2.04, −0.39, and −0.66 eV (see Table I). Note that these numbers are based on a comparison of ADF/BAND adsorption energies for (1×1) supercells and DACAPO adsorption energies for (2×1) supercells. Test calculations with DACAPO on a few of the (1×1) supercells indicate that these adsorption energy changes are somewhat too low, by about 0.5 eV, but the observed trend should be reliable.[46]

3. Effect of potassium doping of B2 NiTi (001) and (110)

In the experiments reported by Tollefsen *et al.*,[8] nitinol samples with submonolayer (about 0.3 ML) coverage of K were studied. Our goal here is to address the influence of the presence of K atoms on the oxidation of NiTi surfaces. To enable valid comparisons with the results obtained for oxidation of undoped NiTi, we have chosen to model the K doping by replacing near surface Ni atoms with K atoms in the five layer slab structures discussed in the previous section. In the typical case, the (1×1) slab supercell is retained by replacing one of the five Ni atoms by K. This corresponds to a coverage of 1 ML K. However, we have also modeled 0.5 ML coverage of K by using a (2×1) slab supercell and replacing only one of the two near surface Ni atoms by K. For simplicity, we will refer to the replacement of Ni atoms by K as "K doping" and the corresponding slab structures as "K-doped" surfaces. This terminology is also used in the relevant literature.[8]

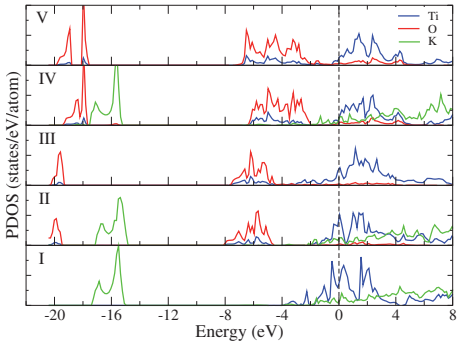

FIG. 6. (Color online) Partial density of states (B2 (001)) of Ti, O, and K atoms: (I) clean K-doped NiTi(001); (II) I+1.0 ML O adsorbed [Figs. 5(a) and 5(b)]; (III) 1.0 ML O adsorbed on NiTi(001) [Figs. 1(a) and 1(b)]; (IV) I+1 ML O_2 adsorbed [Figs. 7(a) and 7(b)]; V) 1 ML O_2 adsorbed on NiTi(001) [Figs. 3(c) and 3(d)].

The Ti-terminated K-doped (001) surface of B2 NiTi is structurally similar to the undoped surface, and as expected, the favored site for adsorption of atomic oxygen is the fourfold hollow site, as found with the undoped surface. The resulting geometry, with a coverage of 1 ML O, is shown in Figs. 5(a) and 5(b), and should be compared with the corresponding undoped structure in Figs. 1(a) and 1(b). The effects of K doping are a reduction in the Ti-O bond from 2.09 Å to 2.06 Å, and an increase in the oxygen charge from 0.88e to 0.98e. The adsorption energy increases, from 8.87 eV to 9.67 eV, indicating that the presence of K facilitates the growth of an oxide layer on the substrate surface. With reference to the discussion of the undoped case above, the structure in Figs. 5(a) and 5(b) is categorized as TiO(001)/KNiTi(001).

Increasing the adsorbate coverage to 1 ML O_2 results in low energy K-doped structures similar to the undoped versions of Figs. 3(a)–3(d). The geometry analogous to Figs. 3(c) and 3(d) is shown in Figs. 7(a) and 7(b), where one O is located in the fourfold hollow site and the other in a bridging position between two Ti atoms [cf. Figs. 3(c) and 3(d)]. The Ti-O bonds are 2.14 and 1.59 Å, and the oxygen charges are 0.87e and 0.60e for the O atom in the fourfold hollow site and in the bridging position, respectively. These values are almost the same as without K doping [Figs. 3(c) and 3(d)]. However, the adsorption energy of 9.68 eV is about 1.5 eV larger than without K doping. As found for adsorption of 1 ML O, it is evident that the presence of K, also with 1 ML O_2, has a positive effect on the formation of the oxide layer. The similarity between Figs. Figs. 7(a) and 7(b) and 3(c) and 3(d) suggests a categorization of the former as TiO_2(110)/KNiTi(001). The K-doped analogy of the structure in Figs. 3(a) and 3(b) has Ti-O bond lengths and oxygen charges very similar to the undoped structure. The adsorption energy is 9.47 eV, which is about 1.5 eV more than without K doping. This structure (not shown here) is categorized as TiO_2(100)/KNiTi(001), in analogy with the structure in Figs. 3(a) and 3(b).

The similarities between the undoped and K-doped structures discussed above are reflected also in the Ti and O PDOS curves, as shown in Fig. 6, (II)–(V). There are only minor changes in the band widths and positions as a result of the K doping, both with a coverage of 1 ML O [Fig. 6, (II) vs Fig. 6, (III)] and with a coverage of 1 ML O_2 [Fig. 6, (IV) vs Fig. 6, (V)]. As expected, the surface Ti PDOS at the Fermi level is reduced upon oxidation, also for the K-doped (001) surface [see Fig. 6, (I), (II), and (IV)] but to a lesser extent than for the undoped B2 (001) surface.

Replacement of the near surface Ni atom by K in the (110) surface of B2 NiTi results, upon geometry relaxation, in a structure which is markedly different from the undoped (110) surface. In the undoped case, the Ti atoms move out and the Ni atoms move in, when compared with the as cleaved (bulklike) (110) NiTi layers. With Ni replaced by K, the K atoms move out and the Ti atoms move in. This is essentially caused by the K atoms having a much larger radius than Ni.

With such a K-terminated (110) surface as the "reactant," oxygen atoms can be adsorbed in a variety of sites, both above and below the K atoms. The lowest energy configurations have oxygen below the surface layer of K atoms, enabling the formation of a TiO or TiO_2 layer, depending on the oxygen coverage.

At a coverage of 1 ML O, the favored adsorption site on KNiTi(110) is in the bridging site between two Ti atoms, see Figs. 5(c) and 5(d). This geometry is similar to the corresponding undoped structure shown in Figs. 1(c) and 1(d), and therefore categorized as TiO(110)/KNiTi(110). However, each O atom is now also bonded to two K atoms, resulting in a longer Ti-O bond length, 1.91 vs 1.84 Å, and a higher oxygen charge, 0.91e vs 0.70e, when we compare with the undoped case, Figs. 1(c) and 1(d). The adsorption energy for the structure in Figs. 5(c) and 5(d) is 9.23 eV, which is almost 1 eV higher than the undoped version in Figs. 1(c) and 1(d). Again, the presence of potassium has a stabilizing effect on the grown oxide layer.

At a coverage of 1 ML O_2 on KNiTi(110), the energetically most favored structure has a TiO_2(001)-like oxide layer below the surface layer of K atoms. This geometry is essentially obtained from the one discussed above, Figs. 5(c) and 5(d), by adding an oxygen atom to a "vacant site" in the uppermost Ti layer, on top of Ti in the layer below. The resulting structure is shown in Figs. 7(c) and 7(d). The Ti-O bonds are 2.13 Å (in plane) and 1.90 Å (vertically) for the threefold coordinated oxygen atom added to the vacant site. For the O atom in the bridging site between two Ti atoms, and also with bonds to two K atoms, the Ti-O bond length is 1.91 Å, i.e., the same as for the corresponding O atom in Figs. 5(c) and 5(d). The total charge on the two O atoms is 1.75e, which is partly donated by Ti atoms in the upper two layers, and partly by the K atoms on the surface. The adsorption energy for the structure in Figs. 7(c) and 7(d) is 10.94 eV, which is 3.4 eV higher than for the structure in Figs. 3(e) and 3(f), which represents the undoped version of 1 ML O_2 on B2 NiTi(110). Clearly, the K doping has made possible a particularly stable layer of TiO_2.

In Fig. 8, the electronic structures of K-doped and undoped versions of oxidized B2 NiTi(110) are compared in terms of PDOS curves for Ti, O, and K. The similarities between TiO(110)/KNiTi(110), Figs. 5(c) and 5(d), and

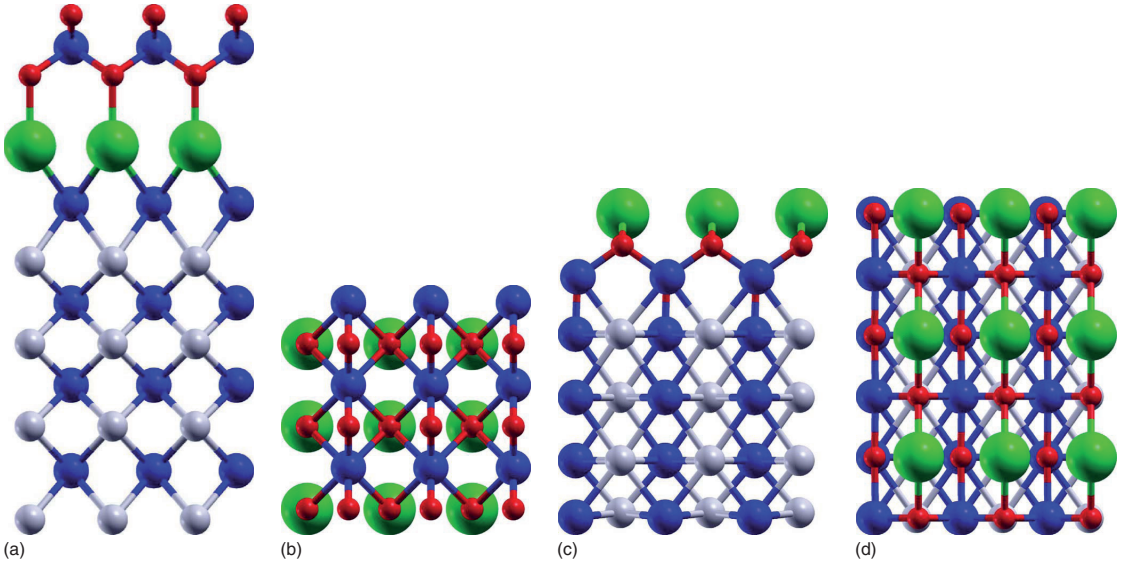

FIG. 7. (Color online) Adsorption of 1 ML O_2 on B2 NiTi with K doping; (a) and (b) side and top view, hollow and bridge sites on the (001) surface; (c) and (d) side and top view, bridge and in-plane sites on the (110) surface. Colors (size, grayscale): K-green (huge, light gray), Ti-blue (large, gray), O-red (small, gray), Ni-white (large, white).

TiO(110)/NiTi(110), Figs. 1(c) and 1(d), are reflected in Ti and O PDOS curves in Fig. 8, (II) and (III) sharing several common features. Further, based on the discussion above, the K-doped structure with 1 ML O_2 adsorbed, Figs. 7(c) and 7(d), can be related both to the K-doped structure with 1 ML O adsorbed, Figs. 5(c) and 5(d), and to the undoped structure with 1 ML O_2 adsorbed, Figs. 3(e) and 3(f). This is reflected in the PDOS curves of Fig. 8, (IV) having common features with the corresponding curves in *both* Fig. 8, (II) and (V). A comparison of Fig. 8, (I), (II), and (IV) shows a reduced value of the surface Ti PDOS at the Fermi level upon oxidation of the surface. However, the Ti PDOS reduction is more pronounced for the undoped surface.

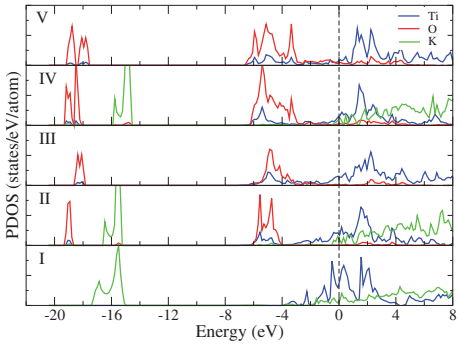

FIG. 8. (Color online) Partial density of states (B2 (110)) of Ti, O, and K atoms; (I) clean K-doped NiTi(110); (II) I+1 ML O adsorbed [Figs. 5(c) and 5(d)]; (III) 1 ML O adsorbed on NiTi(110) [Figs. 1(c) and 1(d)]; (IV) I+1 ML O_2 adsorbed [Figs. 7(c) and 7(d)]; (V) 1 ML O_2 adsorbed on NiTi(110) [Figs. 3(e) and 3(f)].

For the K-doped B2 NiTi(110) surface, we find interesting differences in the adsorption energy at submonolayer oxygen coverage, depending on the relative positions of the oxygen and potassium atoms. For the geometry shown in Figs. 5(e) and 5(f), the adsorption energy is 7.35 eV. Here, the distance between K and O atoms is large, and the stabilizing effect of K on the grown oxide layer is absent. However, as is evident from the top view in Fig. 5(f), the O atom could alternatively be located in a Ti-O-Ti bridging position between two K atoms. In this alternative geometry, see Figs. 5(g) and 5(h), the positive influence of the K atoms is reflected in a much higher adsorption energy of 8.99 eV.

B. Adsorption of oxygen on the *B19′* phase of NiTi

1. Bulk B19′ *NiTi and its low index surfaces*

For the monoclinic B19′ phase of NiTi, we have used experimentally determined values for the lattice parameters, a=2.89 Å, b=4.62 Å, c=4.12 Å, and γ=96.8°.[47] There has been a lack of consensus in the literature on the position of atoms in the unit cell,[48,49] although the lattice parameters are all in good agreement. This inconsistency has been noted over the last few decades.[47] In this study, we have chosen the atomic positions described by Kulkova *et al.*[48] and consider oxygen adsorption on the (010) surface, which is found to have a lower energy than the (001) and (100) surfaces.[11]

The as cleaved (010) surface consists of equal amounts of Ni and Ti atoms, and upon relaxation of the geometry, the Ti atoms move out and the Ni atoms move in, creating an essentially Ti-terminated surface. As such, the (010) surface of B19′ is similar to the (110) surface of the B2 phase.

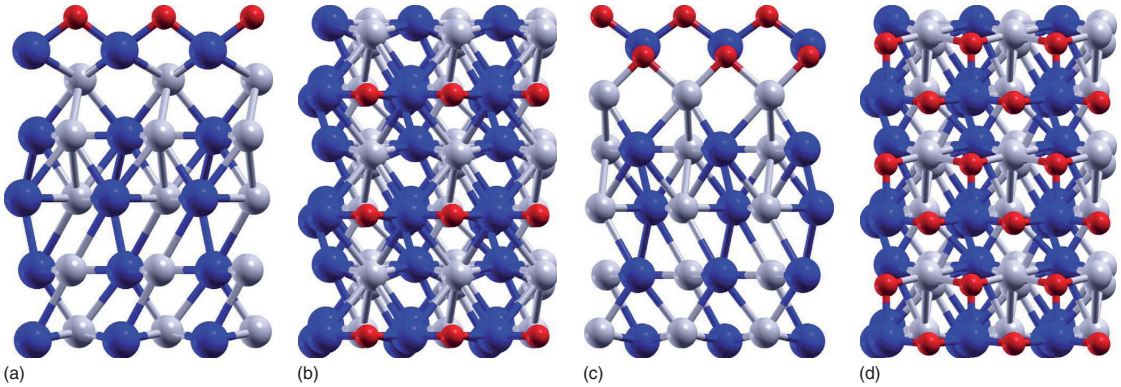

FIG. 9. (Color online) Adsorption of oxygen on B19′ NiTi(010); (a) and (b) side and top view, 1 ML O, twofold bridge site; (c) and (d) side and top view, 1 ML O_2, bridge and in-plane sites. Colors (size, grayscale): Ti-blue (large, gray), O-red (small, gray), Ni-white (large, white).

2. Oxygen adsorption on undoped B19′ NiTi (010)

Oxygen adsorbs at a bridge site between two Ti atoms, corresponding to 1 ML O coverage, as shown in Figs. 9(a) and 9(b). One layer of TiO(110) is formed on the substrate surface, similar to the growth on the NiTi(110) surface in the B2 phase. The Ti-O bond length of 1.83 Å is almost the same as the value of 1.84 Å for TiO(110)/NiTi(110), Figs. 1(c) and 1(d). The adsorbed oxygen atom has gained a charge of 0.65*e*, which is similar to adsorption of 1 ML O on the B2 (110) surface. However, there appears to be a larger contribution of charge transfered from the Ni atoms to O in TiO(110)/NiTi(010) than in TiO(110)/NiTi(110). Based on the Ti and O PDOS curves in Fig. 4, (II) and Fig. 10, (II), we conclude that these two geometries have a similar electronic structure at the surface. Also, the adsorption energy of 8.01 eV for TiO(110)/NiTi(010) is similar to 8.30 eV found for TiO(110)/NiTi(110).

Increasing the oxygen coverage to 1 ML O_2 results in the growth of a TiO_2(001)-like oxide layer, shown in Figs. 9(c) and 9(d). All Ti atoms in the grown oxide are fourfold coordinated, with bonds to two bridging surface O atoms (1.79 Å) and two in-plane O atoms (2.05 Å). The total charge gained by the two oxygen atoms is 1.42*e*, and the adsorption energy is 7.49 eV, to be compared with 1.41*e* and 7.52 eV found for adsorption of 1 ML O_2 on the B2 (110) surface [Table I and Figs. 3(e) and 3(f)]. We also note that a reduction to submonolayer oxygen coverage (0.5 ML O) on the B19′ (010) surface results in an increased adsorption energy (see Table III), similar to the behavior of the B2 (110) surface (see Table I).

The electronic structure of undoped B19′ (010), with and without oxygen adsorbed, is visualized in terms of Ti and O PDOS curves in Fig. 10, (I)–(III). Comparison should be made with the corresponding PDOS curves for the B2 (110) surface, Fig. 4, (I), (II), and (IV). Note, again, that the surface Ti PDOS at the Fermi level is reduced upon oxygen adsorption, in particular at high oxygen coverage (i.e., 1 ML O_2).

3. Effect of potassium doping of B19′ NiTi (010)

Replacement of the near surface Ni atom by K in the (010) surface of B19′ NiTi results in K moving out of and Ti moving into the surface, similar to what was found with the B2 (110) surface. The energetically favored geometries upon adsorption of 1 ML O and 1 ML O_2 have their natural B2 (110) counterparts. This is apparent if one compares the structure in Figs. 11(a) and 11(b), B19′ KNiTi(010)+O, with the one in Figs. 5(c) and 5(d), B2 KNiTi(110)+O, and the structure in Figs. 11(c) and 11(d), B19′ KNiTi(010)+O_2, with the one in Figs. 7(c) and 7(d), B2 KNiTi(110)+O_2. Values for adsorption energies and oxygen charges are comparable, see Tables IV and II. Also for the B19′ (010) surface, the K doping results in significantly higher adsorption energies than for the undoped NiTi surface. At a coverage of 1 ML O, E_{ads} increases from 8.01 eV (undoped) to 9.00 eV (K-doped), and at a coverage of 1 ML O_2, E_{ads} increases

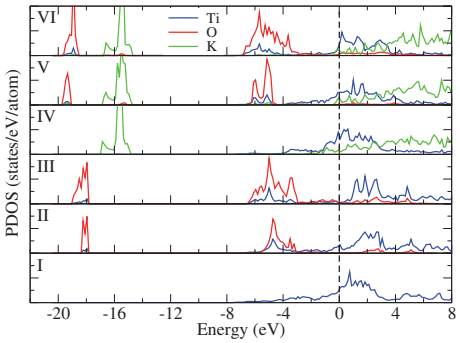

FIG. 10. (Color online) Partial density of states (B19′ phase) of Ti, O, and K atoms; (I) clean NiTi(010); (II) I+1 ML O adsorbed [Figs. 9(a) and 9(b)]; (III) I+1 ML O_2 adsorbed [Figs. 9(c) and 9(d)]; (IV) clean K-doped NiTi(010); (V) IV+1 ML O adsorbed [Figs. 11(a) and 11(b)]; (VI) IV+1 ML O_2 adsorbed [Figs. 11(c) and 11(d)].

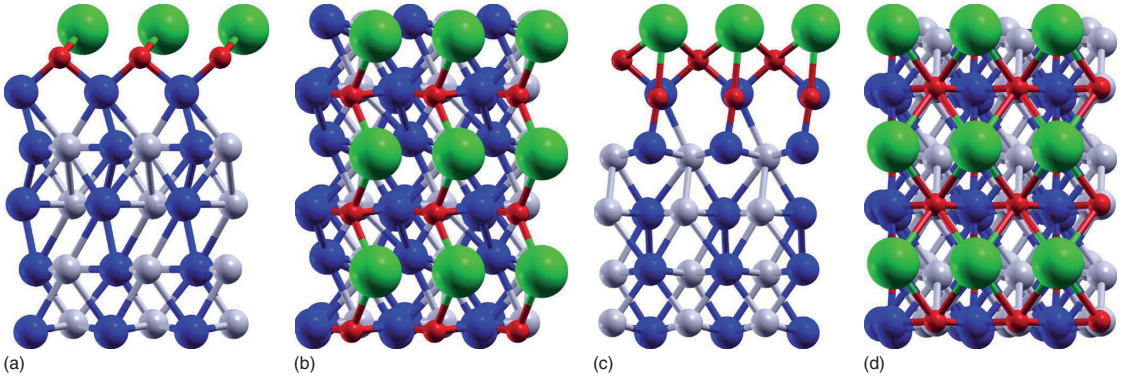

FIG. 11. (Color online) Adsorption of oxygen on K-doped B19′ NiTi(010); (a) and (b) side and top view, 1 ML O, twofold bridge site; (c) and (d) side and top view, 1 ML O_2, bridge and in-plane sites. Colors (size, grayscale): K-green (huge, light gray), Ti-blue (large, gray), O-red (small, gray), Ni-white (large, white).

from 7.49 eV (undoped) to 12.63 eV (K-doped).

The electronic structure of K-doped B19′ (010), with and without oxygen adsorbed, is visualized in terms of Ti, O, and K PDOS curves in Fig. 10, (IV)–(VI). Comparison should be made with the corresponding PDOS curves for the K-doped B2 (110) surface, Fig. 8, (I), (II), and (IV). The surface Ti PDOS at the Fermi level is somewhat reduced upon oxygen adsorption but to a much lesser extent than for the undoped B19′ (010) surface.

IV. DISCUSSION

As pointed out in the previous section, the PDOS calculations, as presented in Figs. 2, 4, 6, 8, and 10, show that the formation of TiO and TiO_2 results in a lower Ti PDOS at the Fermi level compared to the clean surface, with the Ti PDOS corresponding to TiO_2 formation being the lowest. In general, a low density of states at the Fermi level is related to high stability.[49,50] The Ti PDOS at the Fermi level is less reduced for the K-doped surfaces than for the undoped surfaces, in particular for B2 (110) and B19′ (010). This indicates that the K-doped surfaces are more reactive toward additional oxygen and have the best potential for growing thicker oxide layers.

Upon oxidation of the NiTi surfaces, the vertical separation between the outermost Ti layer and the Ni layer below increases in most cases. This is a sign of depletion of Ni atoms from the surface region, consistent with a previous study.[51] In Fig. 12, we have plotted the change in this vertical Ti-Ni separation upon oxide formation. The depletion of Ni from the surface is most pronounced upon the formation of TiO_2, corresponding to two O atoms pr surface Ti atom. From Fig. 12, the effect appears to be larger for the undoped surfaces (solid lines) than for the K-doped surfaces (dashed lines). However, one should keep in mind that the Ti-Ni separation prior to oxidation is significantly larger for the K-doped than for the undoped surfaces. This is mainly because replacement of near surface Ni atoms with K trivially removes Ni atoms from the surface region. In any case, it is fair to say that K doping and oxide formation both contribute to the depletion of Ni atoms from the surface.

Even with undoped NiTi surfaces, our calculations suggest that O_2 dissociates with practically no energy barrier. Upon K doping, the adsorption energies increase (Table II vs Table I, Table IV vs Table III), and the Ti-O bond distances are closer to the values in bulk TiO_2. Thus, the catalytic role played by the K atoms, for the enhancement of the stability of the grown oxide layer, appears to be via electron donation to the oxygen atoms, and not by a reduction in the energy barrier of dissociation.

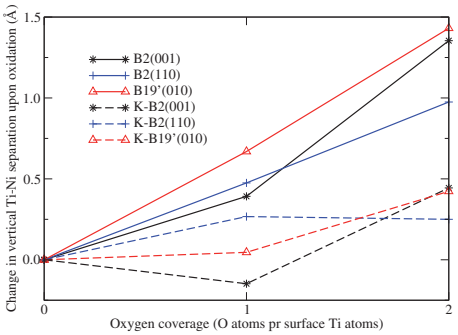

FIG. 12. (Color online) Oxygen coverage dependence of the relaxation of surface atoms for undoped (solid lines) and K-doped (dashed lines) surfaces of B2 (001) (black), B2 (110) (blue), and B19′ (010) (red), i.e., change in vertical Ti-Ni separation upon oxidation. At 1 ML O coverage (one O pr surface Ti), the data points correspond to the geometries of Figs. 1(a) and 1(b) (black star, solid), 1(c) and 1(d) (blue plus, solid), 9(a) and 9(b) (red triangle, solid), 5(a) and 5(b) (black star, dashed), 5(c) and 5(d) (blue plus, dashed), 11(a) and 11(b) (red triangle, dashed). At 1 ML O_2 coverage (two O pr surface Ti), the data points correspond to the geometries of Figs. 3(c) and 3(d) (black star, solid), 3(e) and 3(f) (blue plus, solid), 9(c) and 9(d) (red triangle, solid), 7(a) and 7(b) (black star, dashed), 7(c) and 7(d) (blue plus, dashed), 11(c) and 11(d) (red triangle, dashed).

The present study is limited to the growth of a single layer of TiO_2. As shown in Fig. 12, the geometric relaxation effects increase with increasing oxygen coverage. Presumably, two to three oxide layers could grow, but additional growth is not expected to make a big difference, since it has been found that O_2 physisorbs on $TiO_2(110)$ once it has fully resumed its passivating role.[52] The surface treatment by K doping represents a real possibility to obtain more than a single layer of Ti atoms at the surface, thereby enabling the formation of, say, two to three layers of TiO_2 outside the outermost Ni atoms. Clearly, this would require the adsorption of at least 2–3 ML of O_2. Our ambition here has not been to establish a mechanism for how Ni atoms near the surface are replaced by K atoms but rather to identify the resulting geometries, assuming the replacement has taken place.

The XPS experiments reported by Tollefsen *et al.*[8] show that K doping enhances the formation of TiO_2 at the expense of lower oxides, e.g., TiO. Our results are in agreement with this observation, since the adsorption energies E_{ads} increase significantly more upon K doping for the formation of TiO_2 than for the formation of TiO. The effect is more pronounced for the B19′ (010) surface (0.99 eV vs 5.14 eV) and the B2 (110) surface (0.93 eV vs 3.42 eV) than for the B2 (001) surface (0.80 eV vs 1.51 eV). Here, the numbers in parenthesis represent the increase in E_{ads} upon K doping for TiO and TiO_2 formation, respectively (see Tables I–IV).

TiO_2 is experimentally known to exhibit stable surface indexes including rutile $TiO_2(110)$, rutile $TiO_2(101)$, and anatase $TiO_2(101)$.[13,53] The former is the most stable. NiTi(001) and NiTi(110) of the B2 phase, and NiTi(010) of the B19′ phase are the most investigated NiTi surfaces in previous studies[11,18] because of their high stability, which is also found in the present study. We have considered these three surfaces of NiTi since it is important to identify which titanium oxide that will grow on which substrate surface. Indeed, our investigation shows that the TiO_2 growth on the B2 NiTi(001) surface is best categorized as rutile $TiO_2(110)$ [Figs. 3(c) and 3(d)] or $TiO_2(100)$ [Figs. 3(a) and 3(b)]. As shown by Perron *et al.*[44] these two surfaces of rutile are structurally rather similar. On the other hand, the oxide growth on NiTi(110) in the B2 phase and NiTi(010) in the B19′ phase is better categorized as rutile $TiO_2(001)$. It has been shown[44] that rutile $TiO_2(001)$ is of lower stability than $TiO_2(101)$, which in turn is less stable than $TiO_2(100)$. Doping of the NiTi alloy with K atoms does not change this growth pattern for the different surfaces. As discussed already, $TiO_2(001)$ is characterized by fourfold coordinated Ti atoms, whereas $TiO_2(110)$ and $TiO_2(100)$ have sixfold- and fivefold-coordinated Ti atoms. Since bulk rutile has sixfold-coordinated Ti atoms, we expect a fully passivating oxide to be obtained with about two layers of TiO_2 on B2 NiTi(001), and with slightly more, about three layers of TiO_2, on B2 NiTi(110) and B19′ NiTi(010).

V. CONCLUSION

The main results and implications of the present study can be summarized as follows: (1) NiTi surface alloys react with oxygen and form stable titanium oxides, with adsorption energies in the range 7–11 eV pr adsorbed atom or molecule, as predicted by DFT calculations. (2) Based on their geometric and electronic structures, the grown TiO and TiO_2 surface layers are conveniently categorized in terms of specific low-index surfaces of these oxides. (3) Both TiO and TiO_2 promote the biofunctionality of NiTi surface alloys by depleting Ni atoms from the surface region. (4) By the growth of TiO_2, increased stability of the oxide and biofunctionality of the NiTi surface is obtained. (5) Doping of the NiTi alloy, i.e., replacement of near surface Ni with K atoms, improves the strength of the grown oxides, enhances the formation of TiO_2 at the expense of TiO, and represents a surface treatment mechanism that enables two or more successive layers of Ti atoms at the surface, and thereby the possibility of growing thicker passivating layers of TiO_2.

ACKNOWLEDGMENTS

We thank S. Raaen and H. Tollefsen for fruitful discussions. NOTUR is acknowledged for providing computer time.

*Corresponding author; jon.stovneng@ntnu.no

[1] D. Brunette, P. Tengvall, M. Textor, and P. Thomsen, *Titanium in Medicine* (Springer-Verlag, Berlin, 2001).
[2] K. Otsuka and C. Wayman, *Shape Memory Materials* (Cambridge University Press, UK, 2002).
[3] C. Leyens and M. Peters, *Titanium and Titanium Alloys, Fundamentals and Applications* (Wiley-VCH, Weinheim, 2003).
[4] G. Andreasen, Am. J. Orthod. **78**, 528 (1980).
[5] M. Simon, C. Athanasoulis, D. Kim, F. L. Steinberg, D. H. Porter, B. H. Byse, S. Kleshinski, S. Geller, D. E. Orron, and A. C. Waltman, Radiology **172**, 99 (1989).
[6] H. Gerber and S. Perren, in *Evaluation of Biomaterials*, edited by G. D. Winter, J. L. Leray, and K. de Groot (Wiley, New York, 1980).
[7] L. Peltonen, Contact Dermatitis **5**, 27 (1979).
[8] H. Tollefsen and S. Raaen, J. Appl. Phys. **105**, 123501 (2009).
[9] C. Chu, S. Wu, and Y. Yen, Mater. Sci. Eng., A **216**, 193 (1996).
[10] L. Zhang, C. Xie, and J. Wu, Mater. Charact. **58**, 471 (2007).
[11] S. Kulkova, V. Egorushkin, S. Eremeev, and S. Kulkov, Mater. Sci. Eng., A **438-440**, 476 (2006).
[12] A. Michiardi, C. Aparicio, J. Planell, and F. Gil, Surf. Coat. Technol. **201**, 6484 (2007).
[13] C. Chu, T. Hu, S. Wu, Y. Dong, L. Yin, Y. Pu, P. Lin, C. Chung, K. Yeung, and P. Chu, Acta Biomater. **3**, 795 (2007).
[14] J. Ryhänen, M. Kallioinen, J. Tuukkanen, P. Lehenkari, J. Junila, E. Niemela, P. Sandvik, and W. Serlo, Biomaterials **20**, 1309 (1999).
[15] Y. Fu, W. Huang, H. Du, X. Huang, J. Tan, and X. Gao, Surf. Coat. Technol. **145**, 107 (2001).
[16] F. Wang, W. Buehler, and S. Pickart, J. Appl. Phys. **36**, 3232

(1965).
[17] A. Kellou, Z. Nabi, A. Tadjer, N. Amrane, N. Fenineche, and H. Aourag, Phys. Status Solidi B **239**, 389 (2003).
[18] S. Kulkov, S. Eremeev, and S. Kulkova, Phys. Solid State **51**, 1281 (2009).
[19] W. Cai, C. Tan, T. Shen, and X. Tian, J. Alloys Compd. **438**, 30 (2007).
[20] E. Goo and R. Sinclair, Acta Metall. **33**, 1717 (1985).
[21] M. Punkkinen, K. Kokko, and I. Vayrynen, Solid State Commun. **108**, 567 (1998).
[22] Y. Teng, S. Zhu, F. Wang, and W. Wu, Physica B **393**, 18 (2007).
[23] C. Tan, W. Cai, and J. Zhu, Phys. Status Solidi B **243**, R69 (2006).
[24] P. Soukiassian, T. Gentle, M. Bakshi, and Z. Hurych, J. Appl. Phys. **60**, 4339 (1986).
[25] M. Nolan and S. Tofail, Biomaterials **31**, 3439 (2010).
[26] M. Nolan and S. Tofail, Phys. Chem. Chem. Phys. **12**, 9742 (2010).
[27] S. Vosko, L. Wilk, and M. Nusair, Can. J. Phys. **58**, 1200 (1980).
[28] J. P. Perdew, J. A. Chevary, S. H. Vosko, K. A. Jackson, M. R. Pederson, D. J. Singh, and C. Fiolhais, Phys. Rev. B **46**, 6671 (1992).
[29] http://www.scm.com
[30] G. te Velde and E. J. Baerends, Phys. Rev. B **44**, 7888 (1991).
[31] P. H. T. Philipsen, E. van Lenthe, J. G. Snijders, and E. J. Baerends, Phys. Rev. B **56**, 13556 (1997).
[32] G. Wiesenekker and E. J. Baerends, J. Phys.: Condens. Matter **3**, 6721 (1991).
[33] The KSPACE parameter denotes the number of sample points from the Γ point to a vertex of the Brillouin zone, including the two end points. For a square Brillouin zone, then, one has at the outset a 9×9 regular square lattice of k points, out of which only the symmetry unique points are selected.
[34] K. Yamaguchi, F. Jensen, A. Dorigo, and K. Houk, Chem. Phys. Lett. **149**, 537 (1988).
[35] C. Schweitzer and R. Schmidt, Chem. Rev. **103**, 1685 (2003).
[36] http://dcwww.fysik.dtu.dk/campos/Dacapo
[37] D. Vanderbilt, Phys. Rev. B **41**, 7892 (1990).
[38] Note that the slab-to-slab interaction is not an issue in the ADF/BAND program, where the slab is a truly 2D system which is not repeated in the third dimension.
[39] H. J. Monkhorst and J. D. Pack, Phys. Rev. B **13**, 5188 (1976).
[40] F. Birch, J. Geophys. Res. **83**, 1257 (1978).
[41] O. Mercier, K. Melton, G. Gremaud, and J. Hägl, J. Appl. Phys. **51**, 1833 (1980).
[42] G. Bihlmayer, R. Eibler, and A. Neckel, Phys. Rev. B **50**, 13113 (1994).
[43] R. Weast and M. Astle, *CRC Handbook of Chemistry and Physics* (CRC Press, Boca Raton, Florida, 1982).
[44] H. Perron, C. Domain, J. Roques, R. Drot, E. Simoni, and H. Catalette, Theor. Chem. Acc. **117**, 565 (2007).
[45] At lower oxygen coverage, a structure with the O atom in a bridge between Ti and Ni is also possible, as shown by Nolan *et al.* (Ref. 25). At a coverage of 1 ML O, this is not an energy minimum. However, a structure with the Ti-O-Ti bridge and an O-Ni bond in addition is possible, also at a coverage of 1 ML O. The energy of this structure is very close to the one discussed here [Figs. 1(c) and 1(d)].
[46] For adsorption of 1 ML O and 1 ML O_2 on B2 NiTi(001), DACAPO gives E_{ads}=8.06 eV and 7.92 eV, which is, respectively, 0.81 eV and 0.25 eV less than obtained with the ADF/BAND program.
[47] G. Michal and R. Sinclair, Acta Crystallogr., Sect. B: Struct. Crystallogr. Cryst. Chem. **37**, 1803 (1981).
[48] S. Kulkova, V. Egorushkin, S. Eremeev, J. Kim, G. Lee, and Y. Koo, Physica B **349**, 342 (2004).
[49] G. Bihlmayer, R. Eibler, and A. Neckel, J. Phys.: Condens. Matter **5**, 5083 (1993).
[50] Y. Y. Ye, C. T. Chan, and K. M. Ho, Phys. Rev. B **56**, 3678 (1997).
[51] P. Filip, J. Lausmaa, J. Musialek, and K. Mazanec, Biomaterials **22**, 2131 (2001).
[52] Z. Dohnálek, J. Kim, O. Bondarchuk, J. M. White, and B. D. Kay, J. Phys. Chem. B **110**, 6229 (2006).
[53] C. Chu, C. Chung, and P. Chu, Mater. Sci. Eng., A **417**, 104 (2006).

PAPER V

Theoretical investigation of the interaction of oxygen with pure and K-doped NiTi shape memory surface alloys

Computer Physics Communications (2010), doi:10.1016/j.cpc.2010.12.027

Is not included due to copyright

PAPER VI

Alloy structure of rare earth Ce with Pt base metal, and the adsorption of CO

Preprint

Is not included due to copyright